Winter 1999

Ocean Surface Maps From Blending Disparate Data Through Normal Mode Analysis

William John Schulz Jr.
Old Dominion University

OCEAN SURFACE MAPS FROM BLENDING DISPARATE DATA THROUGH NORMAL MODE ANALYSIS

by

William John Schulz, Jr.
B.S. May 1985, United States Naval Academy
M.S. March 1992, United States Naval Postgraduate School

A Dissertation Submitted to the Faculty of
Old Dominion University in Partial Fulfillment of the
Requirement for the Degree of

DOCTOR OF PHILOSOPHY

OCEANOGRAPHY

OLD DOMINION UNIVERSITY
December 1999

Approved by:

A. D. Kirwan, Jr. (Co-Director of Committee)

C. E. Grosch (Co-Director of Committee)

J. A. Adam (Member)

J. M. Harding (Member)

B. L. Lipphardt, Jr. (Member)

ABSTRACT

OCEAN SURFACE MAPS FROM BLENDING DISPARATE DATA THROUGH NORMAL MODE ANALYSIS

William John Schulz, Jr.
Old Dominion University, 1999

Co-Directors of Advisory Committee: Dr. A. D. Kirwan, Jr.
Dr. C. E. Grosch

Rapid environmental assessment is conducted using disparate data sources in the northwestern Gulf of Mexico. An overview of significant physical features in the Gulf highlights the complexities of the large and meso-scale circulations. Spectral analysis of high resolution current meter and drifter data reveals the significant forcing features detectable by readily available observing techniques. These observations are combined with boundary data extracted from the U.S. Navy's Modular Ocean Data Assimilation System (MODAS) through Normal Mode Analysis (NMA). The NMA blending process is described, and surface maps of velocity and convergence are produced. Using statistical and qualitative techniques, the NMA generated "nowcasts" are analyzed to determine the significant modes applicable to varying oceanographic situations. Fundamental guidance for choosing the number and type of modes in an REA scenario are noted. The NMA method proves to be a useful tool in constructing analytic surface maps when the component modes are wisely chosen.

ACKNOWLEDGMENTS

This project contains the contributions of my family, academic associates, research partners, and Navy shipmates.

First, I am most thankful for the support, understanding and encouragement of my wife Jenny. Along with her, the inspiration from Amanda, Emily, Bob and Kathleen truly sustained this project.

I sincerely thank Drs. Denny Kirwan, Chet Grosch and Bruce Lipphardt for their guidance, patience and flexibility. Their efforts went above and beyond in working around my military commitments and getting me back into the academic arena after a prolonged absence. I am also thankful to the members of the faculty and staff who had an interest in my education at the Center for Coastal Physical Oceanography. Among the staff in the Department of Ocean, Earth and Atmospheric Sciences, Dana Oblak stands out for assistance rendered to Denny and me concerning off-schedule course construction and timely reminders when important deadlines approached. I am especially thankful to the members of my dissertation committee from outside the department, Dr. John Adam from Math and Dr. John Harding from Naval Research Laboratory, Stennis Space Center, Mississippi.

Great appreciation goes to my far-flung data providers:

- Dr. Walter Johnson at MMS for the drifting buoy (SCULP) data.
- Dr. Pearn Niiler at Scripps Institute of Oceanography for the drifting buoy (SCULP) data.
- Dr. Matt Howard and Dr. Norm Guanasso at Texas A & M University for LATEX current meter data.
- Dr. Charlie Barron, Naval Research Laboratory, Stennis Space Center, for providing, explaining, and for patiently re-explaining upon my numerous requests,

the MODAS model and data.

My friends and co-workers in the Navy, through scheduling adjustments and just plain encouragement, were most helpful. I thank the METOC detailer, CDR Paul Stewart, for his understanding and diligence in providing me the time to complete this work. I appreciate the indulgences of the Optimum Track Ship Routing Division at NAVLANTMETOCCEN for the time I've been able to dedicate at school. The Chief of Naval Education and Training's Tuition Assistance Program funded my studies.

Finally, I wish to thank my three officemates at Fleet Training Center with whom I worked for the first two and a half years of this project. Their dedication and professionalism allowed me to be a part time student. Thanks to Keith Atkinson, LCDR Marshall Wilson (who also provided my first UNIX lessons and continues to provide graphics assistance), and especially AGCS (retired) William Stamper. Bill frequently carried more than his share of the load, even while working on his own degree, and I am deeply grateful.

Contents

List of Tables

List of Figures

1 Introduction

The objective of this study is to demonstrate the utility of disparate data and normal mode analysis in the rapid construction of improved resolution ocean surface maps in a near shore region. Motivated by military and commercial needs for rapid analysis of the environment, opportune data not traditionally included in synoptic model initialization can be blended with larger scale model data to provide a detailed description of ocean currents in shallow water.

In this study, the region of interest is the northwestern Gulf of Mexico including the Louisiana-Texas (LATEX) Shelf northward from 25°N and westward from 90°W. Moored current meters and drifting buoys comprise the disparate data set, and normal mode analysis (NMA) is the blending tool.

1.1 The Emerging Need for Rapid Environmental Assessment

Modern civil and military requirements create a demand for rapid, detailed assessments of the near-shore ocean surface. Naval tactical meteorology and oceanography (METOC) increasingly turns toward rapid environmental assessment (REA) to support both planners and the individuals operating in the water [*Whitman*, 1997]. Safe, precise completion of hazardous missions such as special swimmer operations or mine clearance often requires detailed analysis (or "nowcasts") supplied on short notice. Civil operations such as quick and accurate placement of spill containment apparatus also require rapid, detailed surface analysis. This requirement may be filled by innovative data processing techniques developed by the REA com-

The *Journal of Geophysical Research* was used as the journal model.

munity [*Harding et al.*, 1996]. Additionally, REA techniques supplement sparse or non-existent data bases [*Sellschopp and Robinson*, 1997]. Regional REA models thus present advantages over the present operational, synoptic METOC models. Traditionally run every 6, 12 or 24 hours, under stringent data cut-off time requirements, many of these large scale models have a limited ability to ingest data from numerous sources. Thus, a significant piece of data may be overlooked or delayed, reducing the accuracy of the final forecast.

Small scale models also have their handicaps. Determining the boundary conditions for a selected region in rapid fashion can be a limiting factor in most regional models. Remote sensing techniques provide data which can be processed quickly into a prediction model, easing the boundary condition problem. Inclusion of satellite data provides a greater number of observations with quality comparable to moored current meters [*Stammer*, 1997]. The U.S. Navy's Modular Ocean Data Assimilation System (MODAS) allows such ingestion and analysis [*Durham and Boatman*, 1997].

Numerical data ingestion techniques such as empirical orthogonal functions (EOF) have been successfully employed in the decomposition of observed scalar data, such as sea surface temperature, into components which then reveal sub-seasonal time scale influences [*Everson et al.*, 1997]. Complex EOFs have been used to analyze velocity fields [*Kundu and Allan*, 1976; *Legler*, 1983]. In three dimensions, EOF methods also facilitate analysis of potential vorticity advection and water mass movement [*Gavart and Demay*, 1997].

Perhaps more difficult is the assimilation of vector data. The utility of Lagrangian observations in charting mesoscale phenomena is well documented. Float trajectories in the Gulf Stream successfully mapped mixing events associated with eddy formation [*Lozier et al.*, 1997]. Drifters have also been used to provide the first observations of seasonally reversing gyres in the Gulf of California [*Lavin et*

al., 1997]. *Valle-Levinson and Luiza* [1997] proved the utility of such data in an REA scenario by producing a decomposition of forcing components (wind, tidal, or coastal) in the Chesapeake Bay within 30 hours of their first observation.

Normal mode analysis (NMA) represents a relatively new mathematical tool for blending Lagrangian and Eulerian observations into operational models. With sufficient, well-placed observations the method allows the resolution of significant, small scale oceanographic features. The northwest Gulf of Mexico presents a challenging test case. Although data rich, accurate automated analysis of the large shallow area over the shelf is elusive, leading to poor forecasts by most large scale operational models.

1.2 Circulation Features of the Northwestern Gulf of Mexico Including the Louisiana-Texas Shelf

The Louisiana-Texas shelf consists of the shallow (200 m depth or less) region from the Rio Grande to the Mississippi Delta. The bathymetric contours in Figure 1 show that while very narrow near the Mississippi Delta, the shelf widens to approximately 200 km off Sabine Pass, then tapers to about 85 km near Brownsville [*Cochrane and Kelly*, 1986]. The general surface circulation pattern consists of an elongated cyclone covering the shelf, except in July when an anti-cyclone centered south of the Texas-Louisiana border dominates the area. For most of the year, this maintains a generally coastward flow in the east, an offshore flow in the west, and a nearshore flow directed to the southwest. Significant seasonal variations occur, notably the gradual movement of the cyclone from west to east during the winter and spring, and the appearance of a secondary cyclone near the Texas-Mexico border in February. *Cochrane and Kelly* [1986] and *Cho et al.* [1998] provide monthly maps documenting these synoptic scale circulation features. *Oey* [1995] constructed similar maps numerically using the *Oey and Chen* [1992] adaptation of the *Blumberg and*

Mellor [1983] three-dimensional primitive equation regional ocean model. Smaller scale features including the wind-driven along shore current, the Loop Current and Loop Current Eddies, the shelf break counter current, river outflow, and convergence regions support the large scale features [*Oey*, 1995] and affect the safety and efficiency of littoral operations. In preparation for evaluating the NMA technique's ability to accurately reproduce these features, a brief description of each follows.

1.2.1 Along shore current

A significant (monthly mean speeds up to 25 cm-s^{-1}) along shore current runs predominately south and west over the LATEX shelf. This current represents the northern limb of the dominant cyclonic gyre, and exists due to wind forcing and river outflow. *Cochrane and Kelly* [1986] demonstrate that the along shore current correlates most strongly with the along shore component of wind stress, especially west of 92.5°W. (East of this line, the correlation is much weaker.) Wind stress, a function of air density, frictional drag, and wind velocity expressed as $\vec{\tau} = \rho_a C_D \vec{U}|\vec{U}|$, also produces a cross-shelf Ekman transport, which contributes to the frequent formation of areas of convergence and divergence. Due to the limited depth of the water on the inner shelf, the along shore current in this region varies from geostrophy as a balance between the wind stress forcing and bottom stress, according to:

$$\vec{\tau} = \rho r \vec{u} \tag{1}$$

where r represents bottom resistance, ρ is the water density and u is the mean velocity [*Cochrane and Kelly*, 1986]. The effects of bottom stress are reduced, and the surface current enhanced, during high river outflow periods as stratification effectively reduces the friction felt at the surface [*Oey*, 1995].

Cochrane and Kelly [1986] also quantified the correlation of the along shore component of the wind stress with the components of the bottom current. Spectral

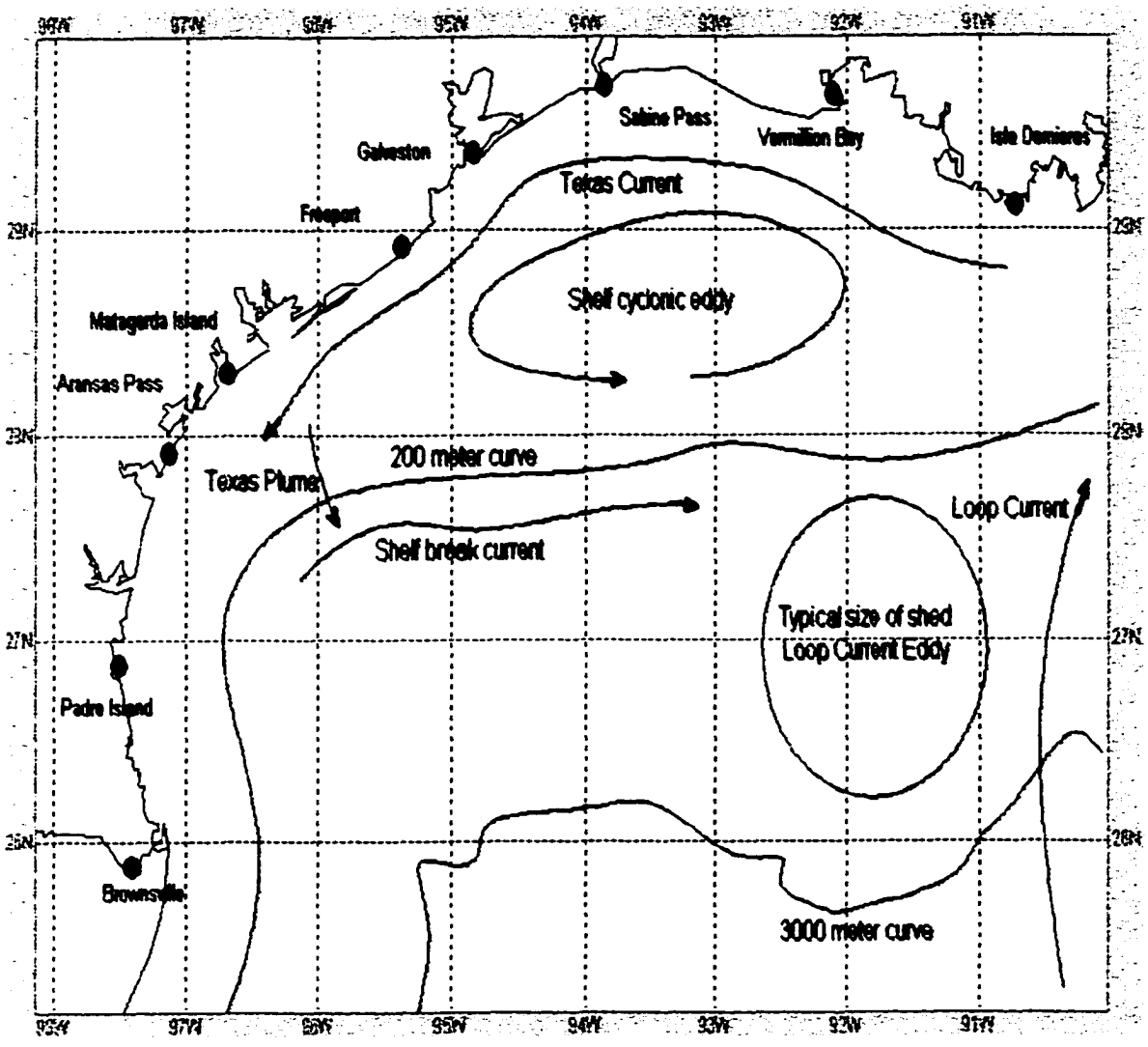

Figure 1: Major circulation features of the northwestern Gulf of Mexico. The Texas Current, Shelf Break current and Texas Plume are in their nominal March positions. The Loop Current is depicted as in a far western-reaching intrusion.

analysis showed significant coherence throughout the 0.02 to 0.8 cycles per day (cpd) band for alongshore currents and from 0.04 to 0.7 cpd for cross-shelf currents. Attempts to correlate wind stress with surface current measurements revealed too much noise in the data set, which was attributed to "baroclinic motions" in the vicinity of a salinity front. *Oey* [1995] later attributed these baroclinic motions to the Mississippi River plume's interaction with the more saline Gulf water.

Average along shore current speeds measured over six years (1978 – 1984) near Freeport, Texas ranged between 25 cm-s^{-1} toward the southwest and 7 cm-s^{-1} toward the northeast. At Freeport, which is nearly in the center of the bounding coastline, the mean current is directed southwest almost ten months of the year, with an easterly component seen only during July and August. Farther eastward along the coast east of Sabine currents range from west 15 cm-s^{-1} to east (July only) near 1 cm-s^{-1} [*Cochrane and Kelly*, 1986].

1.2.2 Loop Current and Loop Current Eddies

The Loop Current, a continuation of the Caribbean Current through the Gulf of Mexico, periodically influences the surface circulation along the LATEX shelf break. The current itself often penetrates the Gulf as far as 29°N and 89°W, while shedding eddies that translate even further westward [*Vukovich and Crissman*, 1986; *Oey*, 1995]. Eddy separation events occur every six to seventeen months. These Loop Current Eddies are persistent, energetic mesoscale features in the northwestern Gulf.

After separation, the eddies drift west to west-southwest at oscillating rates of speed. *Vukovich and Crissman* [1986] determined a bimodal distribution for eddy translation speeds, with 4 km per day the primary mode and 1 km per day the secondary. However, the common range of speeds varied from 1 to 8 km per day, with oscillation periods ranging between 40 to 100 days (0.01 – 0.025 cpd). The highest translation speed noted was 14 km per day. Typical diameters are 300 to

400 km at birth, decreasing to an average of 185 km by the time they reach the western Gulf [*Vukovich and Crissman,* 1986]. Rotational surface current speeds reach between 100 and 200 cm-s^{-1} while the eddy remains in deep water. Most importantly to this coastal analysis, these eddies induce shelf break currents up to 70 cm-s^{-1} [*Tomczak and Godfrey,* 1994].

The area encompassed by this study includes the dissipation area for most Loop Current Eddies. Bounded by 25°N, 28°N, 93°W and 96°W, this northwestern corner of the Gulf is the common end area for the three persistent Loop Current Eddy paths described by *Vukovich and Crissman* [1986]. *Hamilton et al.* [1999] noted that as the eddies translate toward this area, both the eddy path and the individual eddy parameters, including rotational velocity and period, exhibit oscillations with 20 to 30 day cycles. *Hamilton* [1990], using moored arrays, detected peaks in the deep current spectra with similar 20 to 30 day cycles. He attributed these signals to topographic Rossby waves. Further, *Hamilton et al.* [1999] measured the time scale of eddy translation velocity transition events in the northwestern Gulf of Mexico as near 5 days in deep water and 13 days along the slope.

1.2.3 Shelf break counter current

A counter current to the along shore flow runs eastward along the shelf break, forming the southern limb of the dominant gyre. This counter current has been mapped by bathythermograph sections which revealed a dome of cold water pushed up from the bottom circulation over the continental slope [*Cochrane and Kelly,* 1986]. The thermosteric anomalies [*Pond and Pickard,* 1983] shown by these traces dynamically support an eastward current. Over a seven year study, this current averaged 10 cm-s^{-1} eastward [*Oey,* 1995].

Oey [1995] describes two methods of shelfbreak current generation by the Loop Current and its eddies. Occasionally, the Loop Current will expand to the north and

west far enough to "feel" the shelf break just southeast of the Mississippi mouth. During these events, the eastward flow of the Loop Current enhances the easterly current at the extreme eastern portion of the shelf break. The second mechanism involves the shed eddy as it moves westward. These eddies eventually impact the shelf, enhancing the shelf break current in the western Gulf through both momentum transfer and increases in the thermal gradient as they bring a core of warm water near the shelf. These events are marked by the advection of the higher salinity water northward over the western shelf, and a peak in vorticity along the shelf, which shows strongest coherence with eddy passage at frequencies of .01 to .02 cycles per day. [*Oey*, 1995].

1.2.4 River outflow

Examining the surface salinity over the LATEX shelf highlights the importance of wind-directed river outflow as a significant forcing mechanism in the circulatory pattern. While evaporation over the shelf exceeds precipitation (138 cm^3-yr^{-1} vs. 95 cm^3-yr^{-1}), both are overshadowed by the freshwater influx from over a dozen rivers supplying 1070 cm^3-yr^{-1} to the inner one-third of the shelf [*Dinnel and Wiseman*, 1986]. The great majority of this influx flows from the Mississippi-Atchafalaya system. Roughly half of that system's discharge flows onto the LATEX shelf, with the remainder flowing directly to deeper water. That portion is 15 times greater than all other regional outflows combined [*Cochrane and Kelly*, 1986]. Numerical simulations indicate that Coriolis alone is insufficient to direct this flow onto the shelf. Given the significant eastward currents at the shelf break, the plume would head south and then east in the absence of the predominately easterly winds [*Oey*, 1995].

The overflow of brackish water supports a geostrophic balance over much of the middle shelf. At middle-shelf stations between Sabine and the Atchafalaya outflow,

the sea surface slopes upwards toward shore due to the salinity gradient. This slope is balanced geostrophically with a westward current. Seaward of these stations (over the shelf break and into deeper water), the sea surface slope and the current direction reverses, due largely to the warm water advected by Loop Current Eddies and a reduction of the sea surface salinity gradient. Closer to the Mississippi River Delta, the strong freshwater outflow maintains the sea surface slope upwards toward the shore, even out over water up to 500 m deep maintaining westward currents [*Oey*, 1995].

Tracing changes in the surface salinity confirms the alongshore flow pattern inferred from wind stress, and highlights a secondary feature in the southwest portion of the domain. Around April, when the Mississippi-Atchafalaya outflow peaks, salinities on the inner shelf range from 20 PSU near Cameron, gradually increasing to 27.5 PSU near the Texas-Mexico border. During the October minimal outflow period, the same stations average salinities of 31 and 35 PSU, respectively [*Cochrane and Kelly*, 1986]. A particularly interesting feature noted by *Cochrane and Kelly* [1986] is an outflow of brackish water extending eastward from southern Texas. Although no current meters marked this area, such a freshwater intrusion is consistent with the convergence pattern inferred from the wind stress field.

1.2.5 Convergence regions

While the prevailing winds nearly always have an easterly component, greater variance in the north-south component allows for a moving convergence point over the shelf. In the fall, prevailing winds are from the east-southeast, with the core aimed roughly at Brownsville, Texas (the southern end of the Texas coast.) As water is directed shoreward, the transport bifurcates at the coast. The northern leg of this split flow encounters the southwesterly flow following the remainder of the LATEX coast, and a convergence region appears. The seasonal wind changes move the

wind clockwise around the Gulf, and with these changes the point of convergence migrates up the coast reaching the Louisiana border in July. In the fall, winds rapidly back counterclockwise, returning the convergence point to Brownsville by September [*Cochrane and Kelly*, 1986].

A second convergence site occurs due to bathymetry. Along the Louisiana coast from 91.1°W to 92.5°W, depths are less than 20 m, which increases the bottom resistance (r in (1)). To maintain wind-bottom stress balance, the flow speed decreases over this area. Once the flow moves west of 92.5°W, the bottom slopes away and r decreases, leading to an increased flow. This bathymetric influence causes a divergence area near western Louisiana [*Cochrane and Kelly*, 1986]. The establishment of this divergent area in the west and a convergent area in the east supports the predominant cyclonic gyre.

East of this area, the western currents formed in response to the Mississippi River plume meet the eastward shelf break current due to the rapid narrowing of the shelf along 90°W. Hence, another regular surface convergence feature forms [*Oey*, 1995]. Finally, *Hamilton et al.* [1999] note that the Loop Current Eddies themselves tend to be traveling areas of convergence.

1.3 Overview of Research and Assumptions

From the discussion of the physical features, it is clear that a viable analysis of the surface shelf circulation must consider wind, river inflow, bottom topography, and fluctuations in the Loop Current. These factors are considered directly or indirectly by various components of the NMA technique.

The NMA nowcast technique follows the method of *Eremeev et al.* [1992]. The velocity field is considered as a spectral expansion of velocity basis functions. These basis functions, based on the domain geometry and grid resolution, are computed numerically at the start of the analysis. Projections of disparate data (which include

effects of wind and river inflow) onto these basis functions should produce a reliable depiction of the entire region's motion. The observed data is used to constrain the time-dependent amplitudes. NMA has been successfully employed with varying data sources. *Lipphardt et al.* [1997], for example, described the use of high-frequency radar measurements of surface velocity in Monterey Bay to produce surface velocity nowcasts.

The NMA nowcast also requires information about the flow at the domain's open boundaries. Here, open boundary flow is estimated from a regional model run at the Naval Research Laboratory based on MODAS data. MODAS uses optimal interpolation to combine weighted bathythermograph observations, remotely sensed sea surface height and sea surface temperature data with a climatological first guess field [*Harding et al.*, 1996]. (These inputs allow computation of operationally useful depictions of the surface motion in deep water where geostrophy dominates. However, they are not as accurate in shallow water, especially where low-salinity outflow-driven motions dominate.) Using the MODAS data only for open-ocean boundary conditions, disparate surface velocity observations from drifting buoys and moored current meter arrays are assimilated yielding small scale surface current "nowcasts" for the northwestern Gulf of Mexico. (The buoys were deployed along the Louisiana-Texas Shelf as part of the SCULP project in 1993 and 1994. The current meter array data is from the Texas A and M University LATEX Shelf study during the same time.) Employing MODAS incorporates the effects of Loop Current eddies at the boundaries of the domain.

The MODAS surface velocity analyses for the entire region are used in this study as a comparative source. Seaward of the shelf break, MODAS' depiction of the Loop Current and detached eddies is assumed accurate enough to serve as a benchmark when evaluating NMA's depiction of similar features. Other assumptions are the boundary flow values supplied by MODAS are accurate, and the observation data

contains some 'noise' but are still the most reliable sources available.

Section 2 lists the questions addressed in these experiments. Section 3 describes the mathematical fundamentals of NMA and introduces the boundary specifications particular to the northwest Gulf of Mexico. The remaining sections describe the specific application of NMA to the northwest Gulf of Mexico. Products of this study will include assessment of the utility of dynamic observation inclusion via NMA, and increased understanding of the dynamics of the northwestern Gulf of Mexico surface circulation. The seasonal variability of the region, a combined result of wind shifts, topography, and Loop Current rings, complicates surface current analysis with many modern diagnostic tools [*Cho et al.*, 1998; *Johnson et al.*, 1992; *O'Reilly and Guza*, 1998] . It is theorized that eddys such as Loop Current rings conduct significant energy transfer in semi-enclosed seas like the Gulf of Mexico as they interact with bathymetric features [*Rachev and Stanev*, 1997]. Through NMA, energetic modes are identified which may clarify the mechanism of energy tranfer.

2 Research Questions

This study addresses the following questions:

- Does the NMA method effectively consider forcing features unaccounted for by the large scale model, e.g. surface wind speed and river outflow?
- To what extent is oceanographic knowledge of an area required for successful implementation of NMA?
- How sensitive is the NMA method to variability in the open boundary forcing?
- How sensitive is the NMA method to the density of observations in the domain?
- Can optimal mode numbers and types be determined for inclusion in NMA based on the specific oceanographic situation?
- Does assimilation of dynamic observations enable the rapid construction of convergence fields?
- Does the convergence pattern provide substantive information on the flow in the northwestern Gulf?
- Does seasonal change affect the entering assumptions in NMA?
- Is NMA computationally cheap enough with sufficient portability to provide real-time nowcasts?

3 Normal Mode Analysis Technique

The irregular coastline, significant bathymetric features, and frequent sampling make the northwest Gulf of Mexico an attractive area for application of normal mode analysis. The coastline presents a challenging numerical modeling problem. Circulation on the LATEX shelf, as with most shallow water areas, is poorly modeled by operational open-ocean models. Yet, numerous government and commercial activities have conducted studies in the region, providing an abundance of observational data. Complementing this data are MODAS analyses from the Naval Research Laboratory, appropriate as a boundary data source and as a comparative model.

3.1 Components

Operational employment of normal mode analysis requires four *a priori* decisions or data sources:

- Identification of a REA target area.
- Determination of the necessary spatial resolution. From these first two items, calculate the basis eigenfunctions.
- Choosing a source of open boundary flow data.
- Observations to determine time dependent basis function amplitudes.

The first two components can be obtained or constructed well ahead of the desired nowcast time. From these, eigenfunctions are generated as solutions to two homogeneous Helmholtz eigenvalue problems solved on the irregularly shaped domain. Next, the flow across the open boundaries must be established. Numerically

generated horizontal velocity components from an operational, larger scale model provide the boundary forcing once per day in this study. In other operational scenarios, this could be supplied with greater frequency by other numerical models, observations or, in some cases, ignored. These values are then used to obtain the inhomogeneous portions of the solution.

The latter two components are more time-critical. Satisfying the final requirement often confounds the typical forecast process, especially when working in a denied area or with inefficiently placed sensors. The utility of the NMA method is best illustrated when the observation set has the irregular temporal and spatial structure typical of operational situations, as with the drifting buoys and moored current meters. Finally, the observed data are projected onto the basis functions to generate the spectral amplitudes. These spectral amplitudes allow extraction of coherent velocity (or other variable of interest) fields. Figure 2 depicts the sequence of events in a generic normal mode analysis. The four critical components listed above are printed in italics within heavy-framed boxes. The following sections describe the process in greater detail.

3.2 Eigenfunctions and the Homogeneous Solution

This study concentrates on surface current velocity as the variable of interest over an 81 by 51 numerical grid covering the Gulf of Mexico north of 25° and west of 90°W. Grid spacing is 0.1 degrees in both latitude and longitude. Velocity observations at each grid point are decomposed into component forms, which will constrain the problem in both amplitude and direction. Most conveniently for this method, velocity may be expressed as a function of two scalar potentials:

$$\vec{u} = \nabla \times \left[\hat{k}(-\Psi) + \nabla \times (\hat{k}\Phi)\right]. \qquad (2)$$

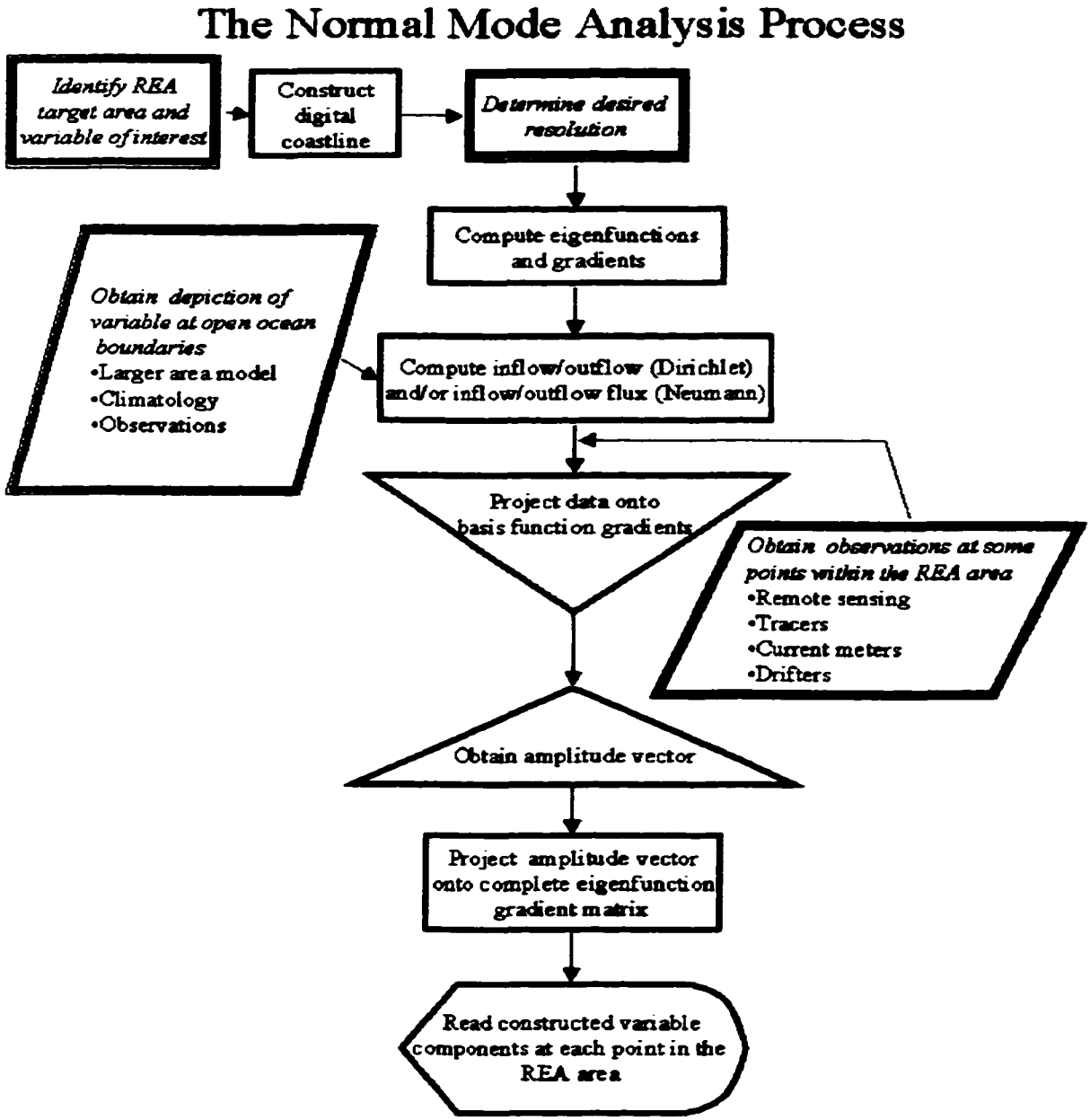

Figure 2: Normal Mode Analysis procedural flow chart.

In this representation from *Eremeev et al.* [1992], Ψ acts as the stream function and Φ as a velocity potential. Finally, $\widehat{k}$ is the vertical unit normal

The surface velocity field is constructed from two constituents, a homogeneous solution and an inhomogeneous solution, as is standard for boundary value problems. The homogeneous solution allows no flow through the boundaries, while the inhomogeneous solution admits flow forcing from the southern and eastern boundaries of the domain; i.e. the open boundaries. From (2), Ψ and Φ are expanded as in *Lipphardt et al.* [1997]. To construct the homogeneous solution Ψ is expanded using eigenfunctions termed *Dirichlet* modes (ψ_n). These eigenfunctions are solutions to:

$$\nabla^2\psi_n + \lambda_n\psi_n = 0, \quad \psi_n|_{boundary} = 0. \tag{3}$$

The ψ_n may be thought of as vorticity modes, with zero horizontal divergence. From (3), the gradients of ψ_n are expressed as in *Lipphardt et al.* [1999] , hereafter referred to as *L99*:

$$\left(u_n^D, v_n^D\right) = \left(\frac{-\partial\psi_n}{\partial y}, \frac{\partial\psi_n}{\partial x}\right). \tag{4}$$

Continuing as in *Eremeev et al.* [1992], Φ is expanded using eigenfunctions called *Neumann* modes (ϕ_m). They are solutions to:

$$\nabla^2\phi_m + \mu_m\phi_m = 0, \quad (\widehat{n}\cdot\nabla\phi_m)\,|_{boundary} = 0, \tag{5}$$

where $\widehat{n}$ is the unit outward normal of the boundary. The ϕ_m may be thought of as divergence modes, with zero relative vorticity. From (2), the gradients of ϕ_m are expressed as:

$$\left(u_n^N, v_n^N\right) = \left(\frac{\partial\phi_m}{\partial x}, \frac{\partial\phi_m}{\partial y}\right). \tag{6}$$

A FORTRAN implementation of the Arnoldi method for determining eigenvalues of large, sparse matrix systems provides the solutions to (3) and (5). The residuals for these calculations were $O(10^{-11})$, which although three orders of magnitude greater than those occuring in an NMA study on a smaller, higher resolution grid [*Lipphardt et al.*,1999] are still small enough to allow a reasonable nowcast.

3.3 Calculating the Inhomogeneous (Boundary) Solution

The homogeneous solutions to (3) and (5) satisfy zero normal flow at all boundaries. This is appropriate for impermeable boundaries like the coastline on the north and west sides of the domain, but is not appropriate for the seaward east and south boundaries where there is both normal and tangential flow.

To account for the normal component of the flow at the domain's open boundaries, a boundary velocity potential solution Θ is calculated numerically at each nowcast time as the solution to:

$$\nabla^2\Theta\,(x,y,0,t) = S_\Theta(t), \quad (\hat{n}\cdot\nabla\Theta)|_{boundary} = (\hat{n}\cdot\vec{u}_{model})|_{boundary} \tag{7}$$

where $\vec{u}_{model}$ is surface velocity provided by the MODAS model and S_Θ is a source term that accounts for the net flow into the domain through its open boundaries [*L99*]. The source term varies due to tidal fluctuations, wind events, and the proximity of Loop Current Eddies. S_Θ is defined as in *L99*:

$$S_\Theta(t) = \frac{\oint \hat{k}\cdot\vec{u}_{model}\,dl}{\iint dx\,dy}. \tag{8}$$

Typical values of $S_\Theta(t)$ are $O(10^7)\mathrm{s}^{-1}$. The sign of $S_\Theta(t)$ changes at eight to ten day intervals in the early winter, then at longer (near 90 day) intervals for the remainder of the period.

Figure 3 shows the behavior of the source term through both experiment periods. Positive values indicate a net inflow. In Winter, the net flow reverses four times; three weeks of net inflow in December, a week of outflow, nearly two months of inflow from mid-January through mid March, and a final nine day period of inflow. The prolonged period of outflow implies significant subsurface replenishment and large surface divergence. In Summer, a two-month period of inflow, with daily averages nearly three times the summer outflow, dominates. This suggests large surface convergence values with compensating subsurface evacuation mechanisms.

Numerical solutions for Θ were generated by a double precision version of the generalized minimum residual method for sparse matrices included in the SPARSKIT FORTRAN library. Maximum residuals were 1.0×10^{-6}. From Θ, inhomogeneous solution velocities are calculated using finite differences as:

$$\left(u^i, v^i\right) = \nabla\Theta\left(x, y, 0, t\right). \tag{9}$$

The Θ and velocity fields are constrained only by the velocities generated from the model along open boundaries, and by the requirement for no normal flow along the coastline. The Θ field represents the portion of the nowcast velocity field due to flow into and out of the domain.

3.4 Generating Spectral Amplitudes and Assembling the NMA Nowcast

The exact solution of a velocity component at any point in the domain comes from superposing an appropriate number of Dirichlet and Neumann modes. Combined with contributions from the boundary conditions these are described in *L99* as:

$$u\left(x, y, 0, t\right) = \sum_{n=1}^{N} \frac{A_n\left(0, t\right)}{\gamma_n^D} u_n^D\left(x, y\right) + \sum_{m=1}^{M} \frac{B_m\left(0, t\right)}{\gamma_m^N} u_m^N\left(x, y\right) + u^i\left(x, y, 0, t\right) \tag{10a}$$

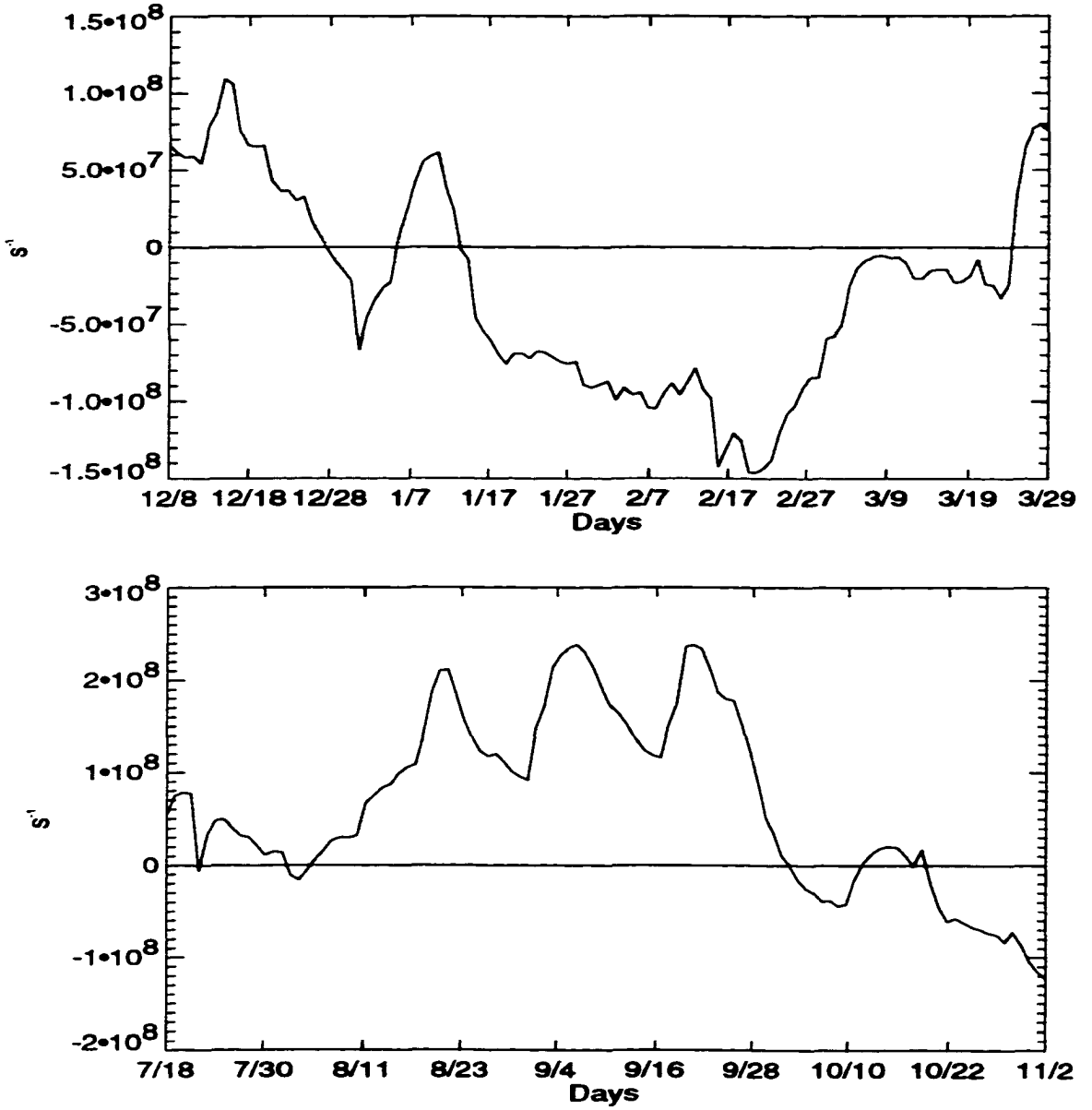

Figure 3: Time series of boundary source term.

$$v(x,y,0,t) = \sum_{n=1}^{N} \frac{A_n(0,t)}{\gamma_n^D} v_n^D(x,y) + \sum_{m=1}^{M} \frac{B_m(0,t)}{\gamma_m^N} v_m^N(x,y) + v^i(x,y,0,t) \quad (10b)$$

where (u^i, v^i) are the inhomogeneous velocity components shown in (9), $\left(u_n^D, v_n^D\right)$ are the Dirichlet mode velocities shown in (4), and $\left(u_m^N, v_m^N\right)$ are the Neumann mode velocities shown in (6). In (10), each of the mode velocity fields has been normalized by

$$\gamma_{n,m}^{D,N} = \frac{\iint \left[\left(u_{n,m}^{D,N}\right)^2 + \left(v_{n,m}^{D,N}\right)^2\right] dxdy}{\iint dxdy} \quad (11)$$

so that $\left(A_n/\gamma_n^D\right)^2$ and $\left(B_m/\gamma_m^N\right)^2$ are proportional to kinetic energy.

A_n and B_m are the time varying spectral amplitudes for the Dirichlet and Neumann modes at each point on the grid. These coefficients are determined from the linear system:

$$\begin{bmatrix} u_1(x_1,y_1) \\ \vdots \\ u_k(x_k,y_k) \\ v_1(x_2,y_2) \\ \vdots \\ v_l(x_l,y_l) \end{bmatrix} = [M] \begin{bmatrix} A_1 \\ \vdots \\ A_n \\ B_1 \\ \vdots \\ B_m \end{bmatrix}. \quad (12)$$

The left hand column contains observed component velocity measurements, taken from the current meters and drifting buoys at specific locations at a given instant. The extreme right-hand column contains the "time varying amplitudes", consisting of "Dirichlet mode 1 coefficient", "Dirichlet mode 2 coefficient", "Neumann mode 1

coefficient", etc., and:

$$[M] = \begin{bmatrix} u_1(x_1,y_1)^D & \dots u_n(x_1,y_1)^D & u_1(x_1,y_1)^N & \dots & u_m(x_1,y_1)^N \\ \vdots & & & & \\ u_1(x_k,y_k)^D & \dots u_n(x_k,y_k)^D & u_1(x_k,y_k)^N & \dots & u_m(x_k,y_k)^N \\ v_1(x_1,y_1)^D & \dots v_n(x_1,y_1)^D & v_1(x_1,y_1)^N & \dots & v_m(x_1,y_1)^N \\ \vdots & & & & \\ v_1(x_l,y_l)^D & \dots v_n(x_l,y_l)^D & v_1(x_l,y_l)^N & \dots & v_m(x_l,y_l)^N \end{bmatrix}. \quad (13)$$

The first row of matrix M, the "basis function matrix", is interpreted as "Dirichlet-mode number 1 u component at point (x_1, y_1)", "Dirichlet mode number 2 u component at point (x_1, y_1)", etc.

The NMA method consists of two operations on this linear system. In the first operation, the time varying amplitude vector is the unknown. A solution for this vector is obtained following the numerical least-squares techniques in *L99*, where the amplitudes are determined by minimizing the following error measure:

$$\sigma^2 = \frac{1}{K}\sum_{k=1}^{K}\left(\tilde{u}_k - u_k^h\right)^2 + \frac{1}{L}\sum_{l=1}^{L}\left(\tilde{v}_l - v_l^h\right)^2 \quad (14)$$

where

$$(\tilde{u}, \tilde{v}) = \left(u^{obs}, v^{obs}\right) - \left(u^i, v^i\right) \quad (15)$$

$$\left(u^h, v^h\right) = (u, v) - \left(u^i, v^i\right). \quad (16)$$

Here $\left(u^{obs}, v^{obs}\right)$ are measured velocities, either from drifter and current meter observations or model data sampled from the interior. K and L are the total number of u^{obs} and v^{obs}, respectively.

Typically, 60–120 measured velocities (120–240 velocity component equations) were used to determine up to 50 A_n and 50 B_m amplitudes, so that the linear system was always overdetermined. The linear least–squares minimization problem was solved numerically using a FORTRAN implementation of the QR factorization technique provided in the LAPACK library.

The second operation treats the component velocity vector (the left-hand side of (12)) as the unknown, combining the spectral amplitude vector and the basis function matrix to obtain velocity components at each grid point in the domain. Limited only by computational power, an infinite number of modes could be used. However, practical limitations to be discussed later restrict this study to an upper limit of 29 Dirichlet and 29 Neumann modes. Future operational users of this method may be limited by hardware and time to fewer modes. (Note that eigenfunctions could be computed for anticipated interest areas, then provided to operational users on CD-ROMs. This removes most of the computational burden from the user.) A reduction in the number of modes employed is actually one form of spatial filtering. This method is well suited for operating on a reduced number of wisely chosen modes.

From (9), other variables of interest may be computed to the same order of accuracy as u and v. Streamfunction (Ψ), velocity potential (Φ), relative vorticity (ξ) and horizontal divergence ($\nabla_H \cdot \vec{u}$) are expressed as:

$$\Psi(x,y,0,t) = \sum_{n=1}^{N} A_n(0,t)\,\psi_n(x,y) \tag{17}$$

$$\Phi(x,y,0,t) = \sum_{m=1}^{M} B_m(0,t)\,\phi_m(x,y) + \Theta(x,y,0,t) \tag{18}$$

$$\xi = \hat{k} \cdot \nabla \times \vec{u}(x,y,0,t) = -\sum_{n=1}^{N} A_n(0,t)\,\lambda_n \psi_n(x,y) \tag{19}$$

$$\nabla_H \cdot \vec{u}(x,y,0,t) = -\sum_{m=1}^{M} B_m(0,t)\,\mu_m \phi_m(x,y) \tag{20}$$

where $\nabla_H = \left(\frac{\partial}{\partial x}, \frac{\partial}{\partial y}\right)$. Note that the above expressions for ξ and horizontal divergence do not require differentiation of the ψ_n or ϕ_m fields, allowing simple construction of the convergence/divergence and vorticity maps.

4 Observational Data

This study employs two sets of observational data; drifting buoys and moored current meters. In addition to constraining the amplitudes, the data serves two purposes:

- Through spectral analysis, the data reveals some of the forcing constituents acting in the Gulf of Mexico.
- The observations provide a benchmark for evaluating the performance of the NMA nowcast.

Identification of the forcing mechanisms, specifically the frequencies of significant signals, are used to select the individual NMA modes used in some reduced-mode experiments. This section provides descriptions of the observational hardware, placement, and significant frequencies found. These frequencies are compared to known forcing signals over the Louisiana-Texas shelf.

4.1 Drifting Buoys

The drifting buoy data set consists of surface drifter trajectories collected during the Minerals Management Service's Surface CUrrent Lagrangian Program (SCULP), provided by P.P. Niiler at the Scripps Institution of Oceanography. This program launched a total of 374 drifters from offshore oil platforms and aircraft between June 1993 and October 1994. Figure 4 shows the uneven temporal distribution of buoy deployments. These buoys follow the upper meter of water, with positions recorded every three hours. Since these data comprised the bulk of the observations used

here, two study periods (18 December 1993 to 30 March 1994, and 18 July 1994 to 2 November 1994) were chosen to correspond with peaks in available buoys. *Lipphardt and Kirwan* [1996] show that while the vast majority of these drifters moved west from their launch basket along the Louisiana coast, many followed secondary paths into the southern portions of the study area, fortunately providing at least sporadic constraints for the NMA amplitudes.

Within the December to March (hereafter 'Winter') period, between 50 and 120 buoys were in the water at any time, some reported for only a few days, others for several months. The three-hourly recording schedule makes the data appropriate for the analysis of low frequency signals. For frequency analysis in Winter, a data set of 111 buoys was selected following two criteria: the buoy record must be at least 30 days in length, and the reporting period must start no earlier than 30 days prior to the start of the Winter period and end no later than 30 days after the end of the Winter period. From this set, time series of the observed u and v component velocities were compiled, and the quadratic trends were removed numerically. An example of observed data for one buoy is provided in Figure 5. The upper panel reveals the oscillations of the east-west velocity along the drifter's trajectory, suggesting interaction with one or more forcing phenomena. In this panel the dot-dashed curve represents the raw u-component data, the dotted curve the quadratic trend, and the solid curve the data after removing the quadratic trend. The dashed horizontal line is the mean of the data after quadratic trend removal, with solid horizontal lines above and below delineating two standard deviations (2σ). With few exceptions, the data remains within the 2σ envelope. Such constraint is typical of the buoy and current meter records studied and suggests well behaved data with some 'noise'. This supports the basic premise of accurate observational data, and allows later evaluation of NMA success based on analysis of variance.

A spectral analysis of the drifter velocities shown in the middle and lower panels

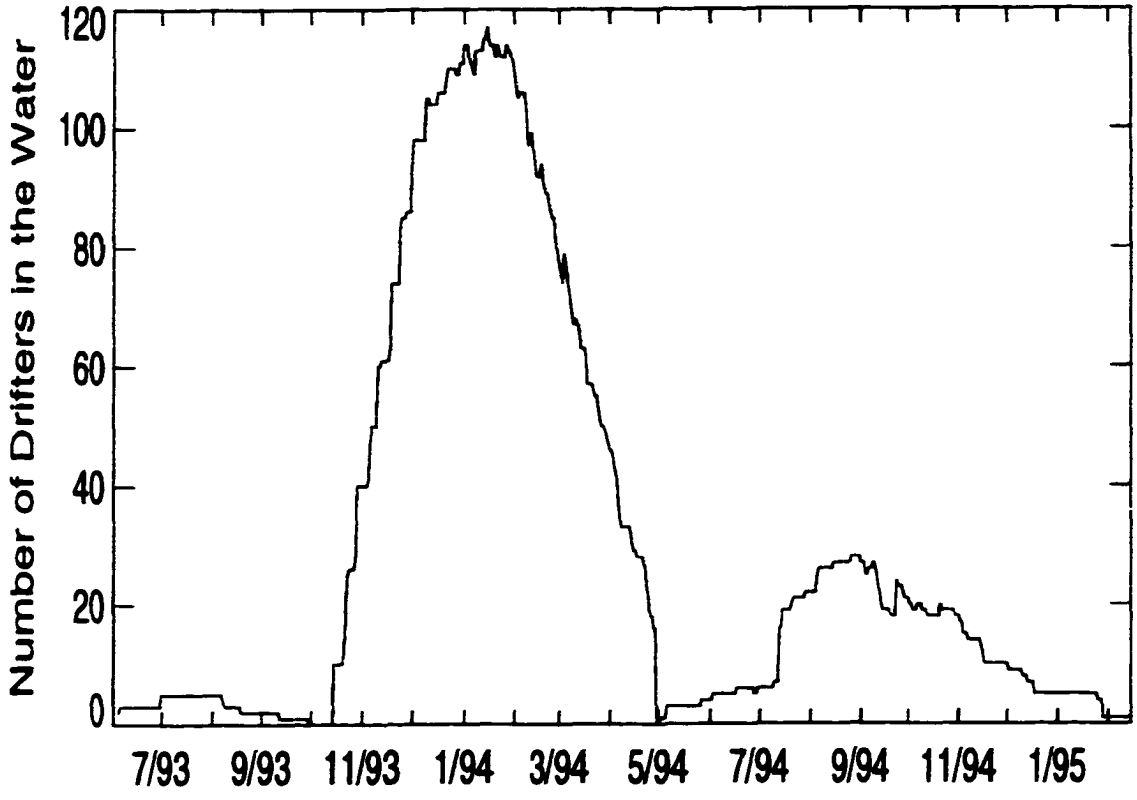

Figure 4: Buoy deployments over the LATEX shelf (from *Lipphardt and Kirwan*, [1996]).

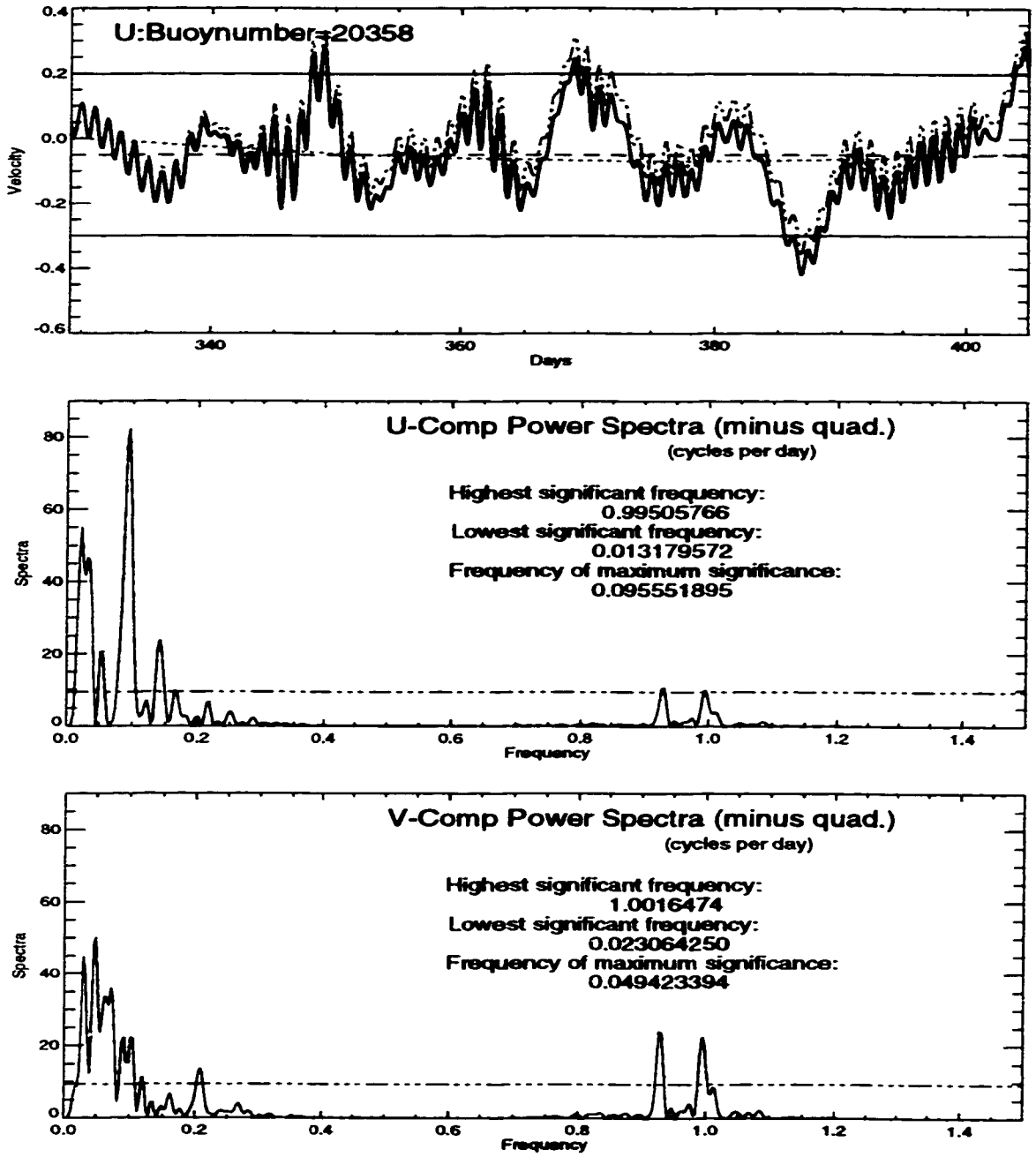

Figure 5: Example of a drifting buoy velocity record. The top panel contains a time series of u component observations. V component observations (not shown) were similarly analyzed. The power spectra of the u observations (center panel) and the power spectra of the corresponding v observations (lower panel) are shown.

of Figure 5 reveals predominant frequencies from 0.01 cycles per day (cpd) (100 days, nearly the length of the 113 day record of the Winter period) to 1.0 cpd. The power spectra are calculated by Lomb's method, which calculates the spectrum for unevenly sampled data by weighting the data on a per point basis as opposed to a time interval basis [*Press et al.*, 1992]. This method is ideally suited for data not equally spaced in time. (As a consistency check, power spectra calculations made using the maximum entropy method [*Press et al.*, 1992] provided similar results.) The dot-dash horizontal line in the two panels marks the 95% significance level. Some buoys displayed over 60 significant frequencies, some as few as 10. Figure 6 shows histograms of the frequencies collected from these analyses for the Winter period. Significant frequencies cluster around 0.1 cpd, spreading up to 0.2 cpd. These low frequency signals indicate various dynamic forcing mechanisms listed later in this section. A secondary grouping between 0.9 and 1.1 cpd marks inertial and tidal signals.

Despite a smaller number of observations, results are similar for the July to November (hereafter 'Summer') period. During this period, 18 to 30 buoys were in the water. Using the same criteria as for the Winter set, 34 buoys were selected. The spectral analysis again returned a bimodal distribution, with a group of frequencies below 0.2 cpd and a second group near the inertial frequency. Figure 7 illustrates the distribution of the summer frequencies.

4.2 Current Meters

Current meters deployed for the Louisiana-Texas Shelf Circulation and Transport Processes Study (LATEX-A) provided an Eulerian input for the normal mode analysis. The current meters operated periodically from April 1992 to April 1995. Five types of current meters were used in that study (Endeco 174 SSM and DMT, Aanderaa RCM 4/5 and 7/8, and InterOcean S4) with the top sensor at a nominal depth

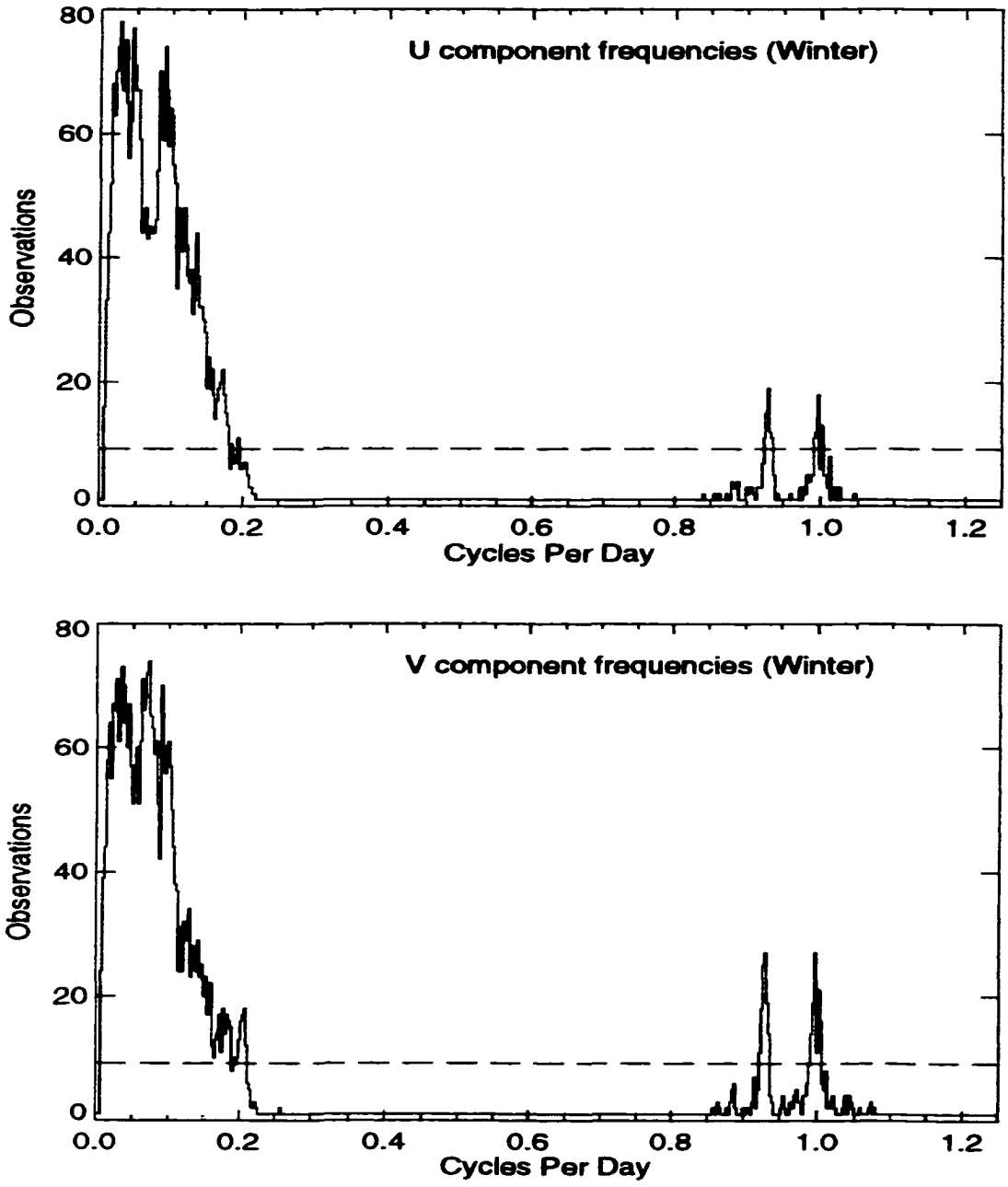

Figure 6: Histogram of frequencies present in the Winter buoy records.

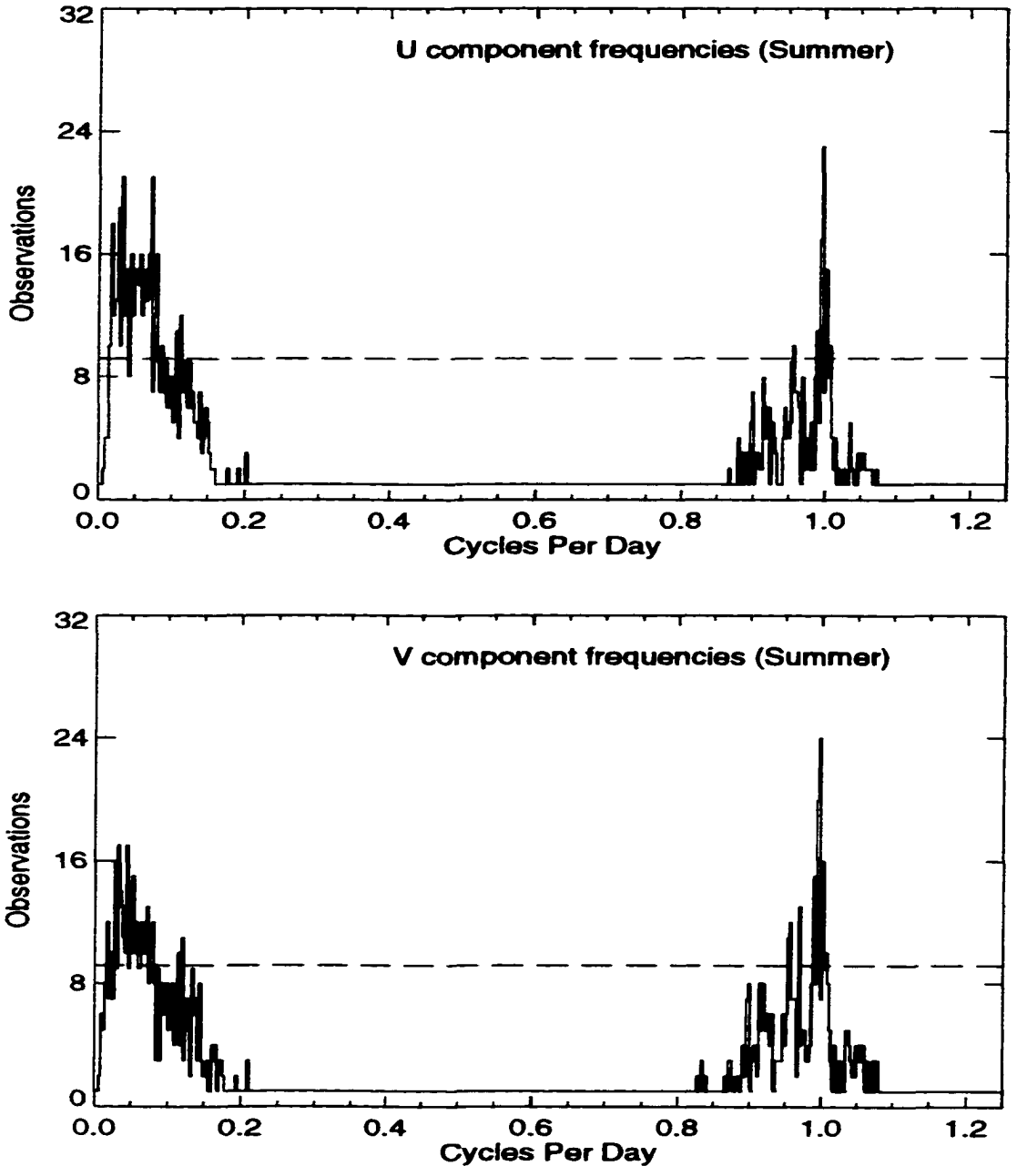

Figure 7: Histogram of frequencies present in the Summer buoy records.

of 10 – 12 meters [*Chen et al.*, 1996] measuring horizontal current components every 30 minutes (six times the frequency of the buoy observations). Of the 39 meters deployed, 19 provided near-surface (10m) velocity component readings within the study area during the Winter and Summer observation periods.

The 19 current meters used for this study provided 10 to 30 percent of the observations for each nowcast. Component time series were also compiled for these Eulerian sensors, with the same spectral analysis techniques applied. Although comprising a distinct minority of the observation data, the position of the meters on the shelf and near the shelf break make them critical sensors in areas where bathymetry affects current motions. Therefore, the current meters were weighted equally with drifter velocities in mode selection for the reduced mode experiments.

Figure 8 and Figure 9 show the frequencies evident in the current meter records for the Winter and Summer periods. Most notable in these plots is the extensive number of signals detected in the 0.2 to 0.8 cpd range, the band virtually ignored by the buoys. Since many buoys passed near the current meter moorings, spatial differences are discounted as a possible explanation for the disparity in spectral coverage. The higher sampling rate of the meters also fails to explain the gap, since even the 3-hourly rate of the buoys should have been sufficient to capture signals near 0.5 cpd. Somehow the Lagrangian nature of the buoys masks the 0.2 to 0.8 cpd band. Additionally, the current meters also retain the peaks near 0.1 and 1.0 cpd present in the buoy analysis.

4.3 Forcing Signals

Section 1.2 described the physical features dominating the area. Each of these mechanisms generate spectral signals detectable by time series analysis. The amplitudes of these signals fall in the range of surface velocities common to the Gulf of Mexico, typically less than 10 cm-s^{-1}. However, *Chen et al.* [1996] note amplitudes near the

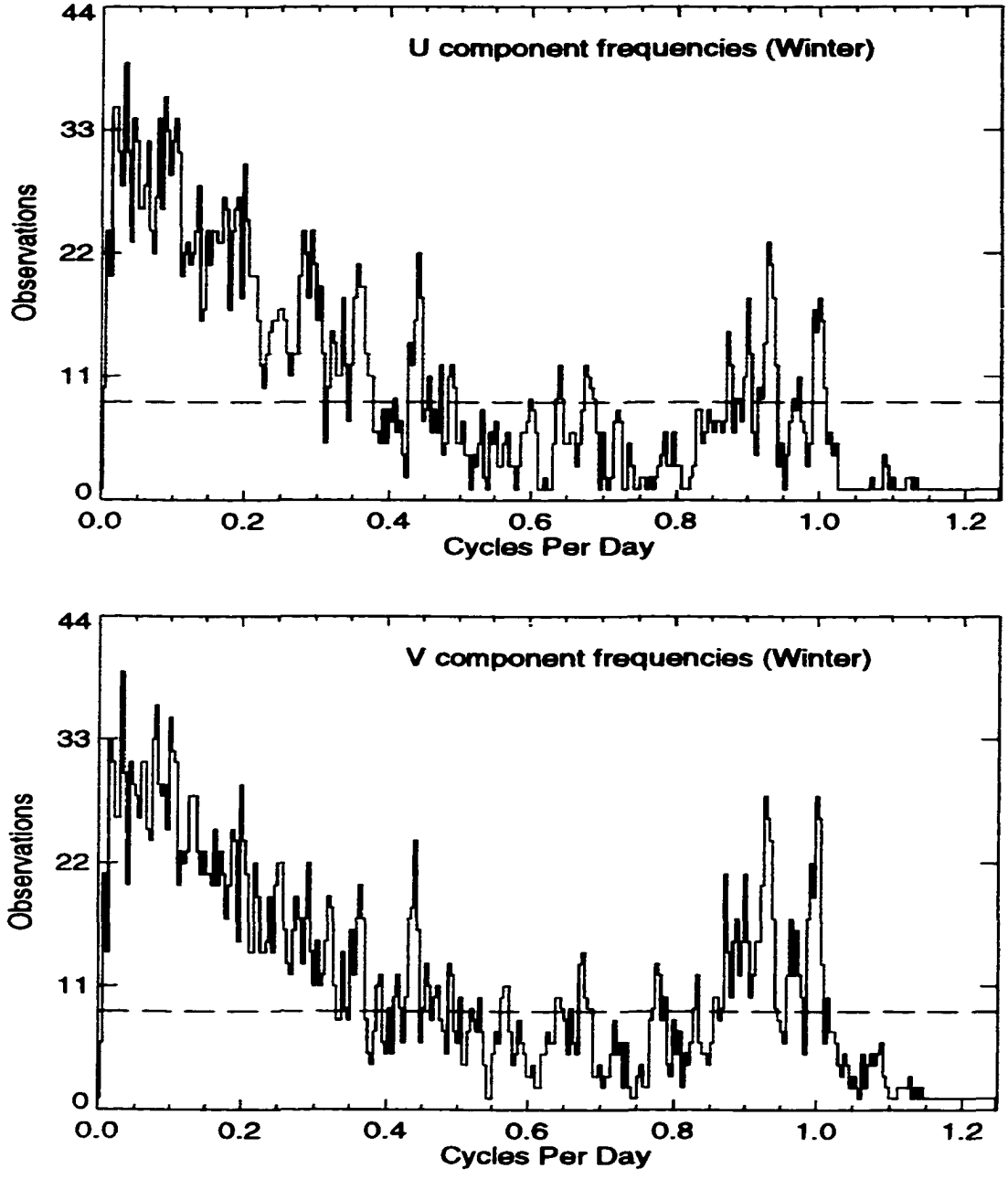

Figure 8: Histogram of frequencies detected in the Winter current meter records.

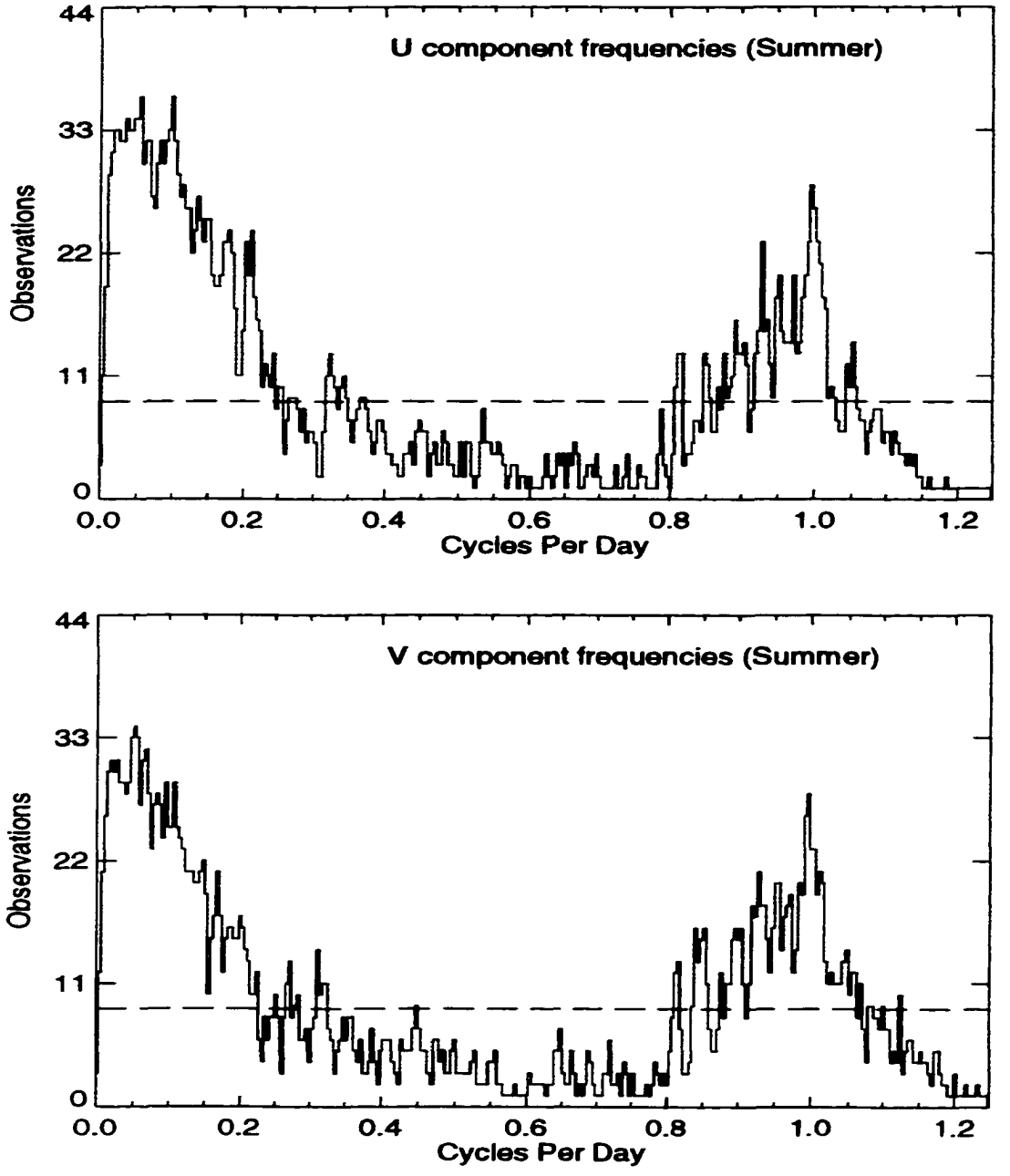

Figure 9: Histogram of frequencies detected in the Summer current meter records.

shelf break at 21 and 54 cm-s^{-1}. The latter amplitude nearly matches amplitudes on the shelf associated with hurricane passage. As previously noted, *Tomczak and Godfrey* [1994] described even higher shelf break currents, up to 70 cm-s^{-1}. Thus any NMA generated velocities over the LATEX shelf above 70 cm-s^{-1} will be suspect. By noting the frequency of signals natural to the REA target area, modes matching those frequencies can be included in a NMA nowcast. Ideally, a reduced number of such well chosen modes will produce surface maps with statistics comparable to maps derived from larger numbers of modes.

In the shallow water on the shelf, wind forcing drives many of the mechanisms described in section 1.2. Changes in the wind stress vector drive the along shore current, determine convergence region locations, and generate near-inertial oscillatory signals [*Kundu and Thompson*, 1985]. Tidal forcing contributes as well, transferring energy into near-inertial motions during interaction with topographic features [*Hendershott*, 1973] . A summary list of the amplitudes and frequencies associated with the predominant influences over the shelf follows. See *Chen et al.* [1996], *Hamilton et al.* [1999], *Kirwan et al.* [1984] and Section 1 for further details.

- O_1 tidal period of 1.08 cpd.
- Inertial periods of .91 to .99 cpd.
- K_1 tidal period of .996 cpd.
- Basin tidal resonance of .86 cpd.
- Acceleration changes due to shingles (small eddies near fronts) generate oscillations near .48 cpd.
- Eddy rotational periods of .07 to .16 cpd.
- Atmospheric frontal passage commonly at .11 cpd.

- Oscillations in eddy translational speed from .01 to .025 cpd.
- Oscillations in eddy rotational period, and swirl speed from .03 to .04 cpd.
- Wind fluctuations from .0667 to 0.2 cpd.

Higher frequency signals noted in the literature include harmonics of the inertial and tidal periods, plus diurnal signals associated with land-sea breeze phenomena near the coast. These higher signals cannot be reliably resolved with these data.

Figure 10 compares the signals detected in the buoy and current meter data with the expected signals discussed above. Several noteworthy disparities illustrate the subtlety of features of the Gulf of Mexico circulation and the value of a combined Eulerian/Lagrangian sensing strategy.

First, both buoy data sets capture the 0.01 to 0.2 cpd band, which contains fluctuations in eddy translation speed, eddy swirl velocity, eddy rotational periods, and the more common oscillations in surface wind speed. The winter current meters detect these signals yet extend this band out intermittently to 0.8 cpd. The 0.2 to 0.8 cpd portion of the band corresponds to events occurring every 1.5 to 5 days, suggesting wind related events such as winter weather front passages. The current meters, sitting farther offshore than most of the buoys (which at this time of year typically move coastally southwest), likely feel the impact of these events more than the drifters. *Hamilton* [1990] offers a more oceanographic explanation for the buoy's inability to detect higher frequency signals on the shelf. Buoys which become involved in a vigorous eddy tend to follow the 20° C isotherm, which places the buoy near mid-radius of the eddy. Only when the eddy rotation begins to slow does the buoy move to the outer areas of the eddy. Thus, drifters bias to seaward the occurrence of higher frequency (greater than 0.2 cpd) eddy rotation events when they are detected at all. Detection of 0.2 to 0.8 cpd ('weather and large eddy band') events by buoys is rare since eddies are strongest in the southeast portion of the area,

generally decaying as they transit northwest. Still, *Kirwan et al.* [1984] detected oscillations of .48 cpd and higher in a study of three drifters entrained in northwest Gulf of Mexico eddies. Their study also noted buoy interaction with shingles (eddies less than 10 km diameter) as a source of oscillations centered near .48 cpd. The SCULP drifters rarely reached the southeastern portions. However, such an intially vigorous eddy may extend to the shelf break, and as *Oey* [1995] indicates, influence transport on the shelf. The current meters on the shelf would detect such events.

The Winter current meter data provided insight into shelf circulation by capturing a unique portion of the spectrum. The Summer current meters are revealing by their omissions. During Summer the meters fail to detect the wind fluctuation band, the eddy rotation period band, and the weather and large eddy band. Light winds along the Gulf coast in summer provide too faint a signal for the subsurface current meters. The buoys however, cover a greater area and are in more direct contact with the atmospheric forcing. During Summer, the lack of eddy and Loop Current intrusions make the light winds a dominant signal that must be included in an NMA trial.

Finally, notice in Figure 10 the coverage surrounding inertial and tidal frequencies. The buoys restrict the significant portion of the spectra to 0.95 to 1.0 cpd, while the meters expanded the significant near-inertial spectrum to as low as .85 cpd. The Winter meter records in figure 8 also indicate significant frequencies above inertial, near 1.05 cpd. Both cover the expected K_1 tidal signal, but only the meters come close to matching the O_1 tide. Recall that boundary forcing is provided once per day in this study, which fails to account for tidal motions. Thus, the current meters are the most complete source for assimilating a tidal signal into the NMA process.

Clearly a combination of Lagrangian and Eulerian sensors provides the best opportunity for detecting all significant physical forcing mechanisms. The drifting

buoys, while providing extended areal coverage, report wind influences and map complete eddy and current paths. The current meters, somewhat insulated from wind due to depth, mark tidal signals and large, shelf-affecting eddy movements. To determine the importance of this information in conducting NMA, nowcasts will be created using 1) a large number of modes for a "best case" scenario, 2) a reduced number of modes, with mode selection based on amplitude size, and 3) a reduced number of modes, selected by matching the significant frequencies shown by time series of the mode amplitudes to frequencies found in the data or noted in the literature describing the region.

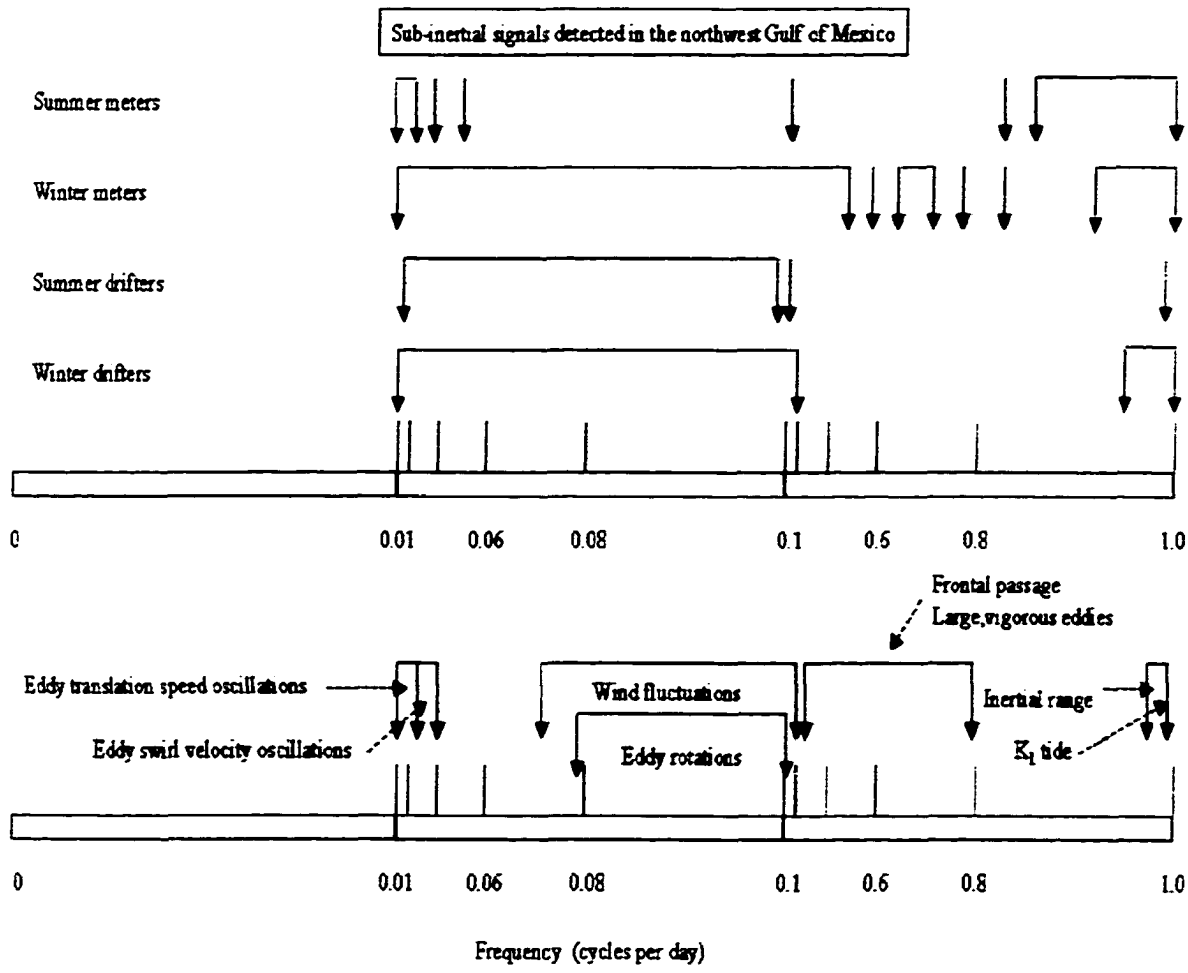

Figure 10: Summary of detected signals and their probable sources.

5 Nowcasts

In this section, parameters for a baseline normal mode analysis are determined. After noting the baseline NMA's performance in comparison to MODAS and raw data, NMA is conducted using reduced numbers of modes chosen through varying selection processes. These trials reveal the sensitivities to mode type and the amount of *a priori* environmental knowledge required for generating usable nowcasts. Reliability thus established, NMA generated surface convergence maps are presented.

5.1 Determining the Number of Usable Modes

Two concerns govern the selection of a baseline scenario. First, the number of available observations imposes an upper computational limit on the number of usable modes. Second, difficulties in reliably resolving spatial scales further restricts the number of modes due to inefficiencies in sensor placement and the expected size of pertinent physical features.

Equation (12) implies the limiting influence of observations. For a uniquely determined or overdetermined system, the maximum possible number of amplitudes generated in that matrix equation equals the number of velocity observations. The observations are the "independent" factor in the initial computation of the amplitude vector. When these amplitudes are then projected onto the eigenfunction gradient derived velocities, they may be regarded as "degrees of freedom." In theory, over 240 modes could be generated based on the peak available data during the Winter period. However, early trials computing only 100 modes (50 Dirichlet and 50 Neumann) produced large, unrealistic amplitudes with corresponding velocities several orders

of magnitude too large, similar to the early trials described in *L99*. In a REA situation, or if the method is applied to the analysis of a denied-entry area, the number of available observations will be much less than in a controlled research project such as SCULP or LATEX-A.

Employing the maximum theoretical number of modes fails because of sub-optimal sensor spacing. Physically, the numerical machinery in Section 3 projects observations onto the eigenfunction gradients generated from equations (3) and (5). Problems arise when the projected data are two widely spaced on the eigenfunction gradients, allowing calculations between the data points to proceed unconstrained. As the mode number increases, the smallest spatial scale resolved by that mode decreases. From equation (10), one may be tempted to incorporate as many modes as possible, reasoning that the more components included in the Fourier-like sum, the more accurate the final computed velocity component. But, similar to "noodling", which occurs when higher and higher order polynomials are used to approximate a function's behavior between two data points, the high mode number eigenfunctions eventually begin to infer unrealistic motion from the data. Further, if the data do not resolve the scales of the higher eigen modes, the energy in these scales (distributed through the amplitude vector in (12)) is aliased back into scales that are resolved.

Energy from higher modes can be redistributed and can corrupt the lower modes. The unrealistic velocities produced by the 100 mode trials usually occurred in areas lacking observations. Despite a great number of sensors, many buoys converged along the few predominant paths described in *Lipphardt and Kirwan* [1995] or reported while very close to current meters. (Recall that from the buoy launch point along the southern Louisiana coast, the predominant buoy drift pattern was westward along the shelf. Only a few buoys, probably through anomalous wind conditions or interaction with eddies, drifted into the central and eastern areas.) Thus,

large data-free areas exist, allowing small features to go unresolved.

As long as the spatial scale of a dynamic feature is small enough to fit within a data-free region, spurious velocities can result. Examining plots of the eigenfunctions reveals when such a situation will likely occur. In Figure 11 the Dirichlet and Neumann eigenfunctions for mode 2 and mode 29 are displayed for comparison. The Dirichlet mode 2 can be expected to resolve large circular features such as the shelf eddy, but is a poor representation of overall northwestern Gulf circulation. The Neumann mode 2, however, maps out a flow along the western coast similar to the expected path of the Texas Current. Both depictions show only large features, requiring only a widely spaced observation population for detection and modeling. Raising the mode number to 29, in the lower two panels of the figure, results in multiple, smaller circular features in the Dirichlet modes. The size of these rings matches the smaller circulation features discussed in Section 1. While even smaller micro-scale circulations may exist over the LATEX shelf, their presence is not well documented in the the literature and apparently not resolved by the LATEX observations. For the area and periods under study, the maximum mode Dirichlet or Neumann employed is 29.

5.2 Baseline Scenario

An optimum situation in NMA consists of a large number of observations, spread well throughout the domain. Roughly one month into the Winter trial, 22 January 1994 is the closest to optimum scenario in the data set, and therefore a good candidate for a baseline scenario. On this day, the observation field consisted of 119 drifters and 19 current meters, dispersed as shown in Figure 12. While spatial data coverage is good along the shelf, only a few buoys reached the south central and south eastern portions of the domain. In the large gaps left here, unrealistic amplitudes develop unless modeled (or other source) observations are sampled as additional data.

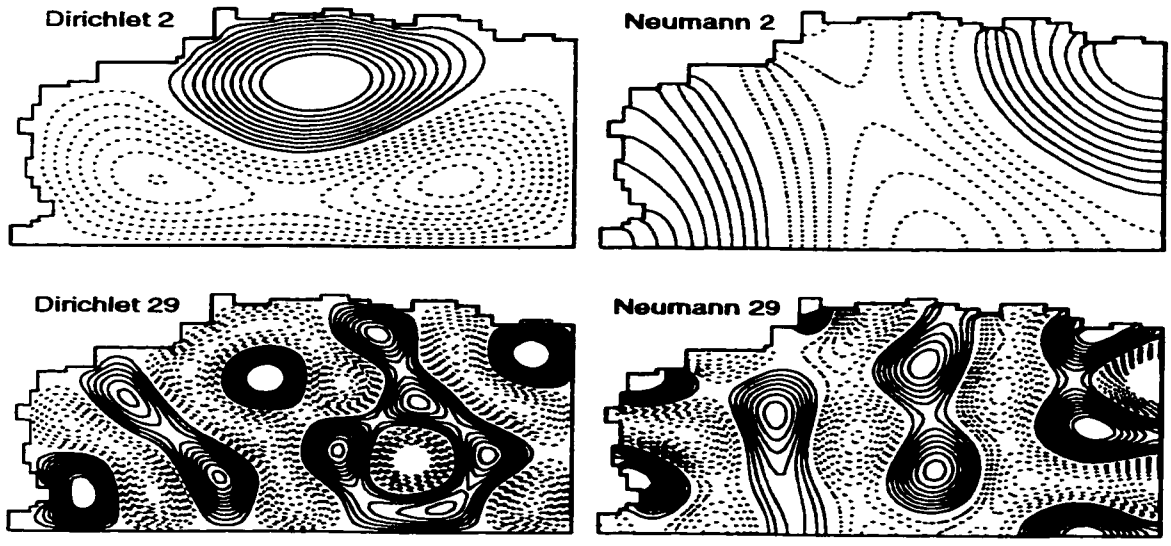

Figure 11: Sample eigenfunctions. Modes 2 and 29 for both the Dirichlet and Neumann are displayed.

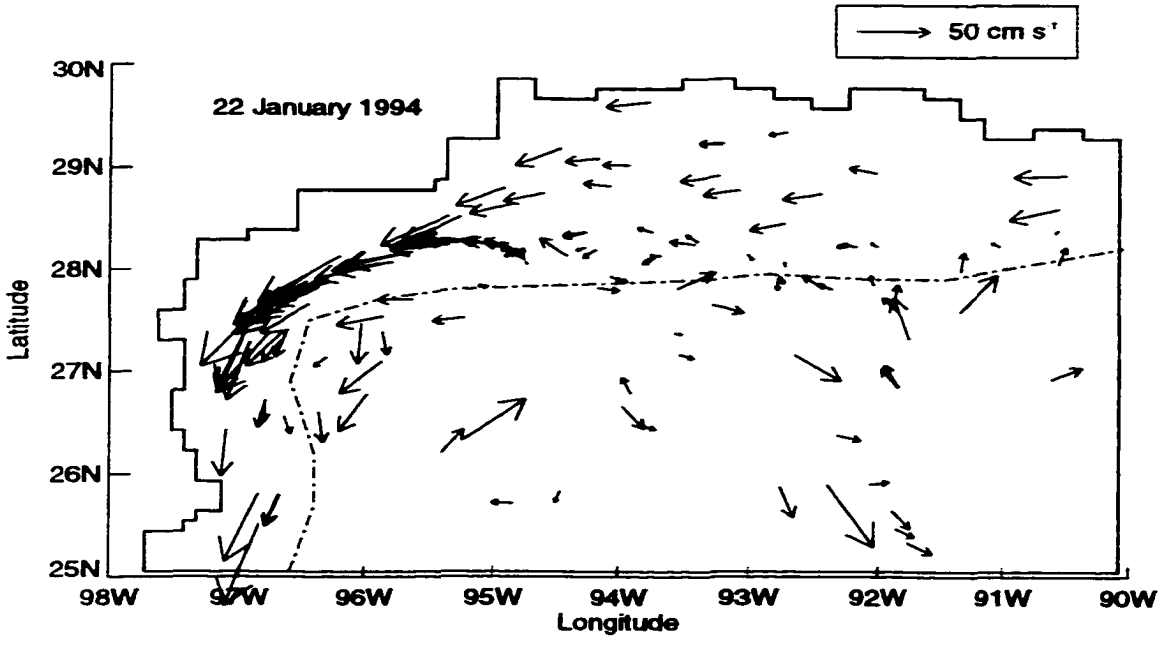

Figure 12: Observations available for the baseline trial of 22 January 1994. Data set consists of 19 current meters and 119 drifting buoys. The dotted line approximates the 200 meter depth contour.

When such gaps occur in this study, modeled velocity components are inserted. *L99* addresses this situation by sampling model surface velocities from 20% of the points in data-free regions. In this study, certain areas are consistently data poor, so fixed sampling sites can be determined and checked for each nowcast. Figure 13 shows the potential sites for inserting simulated observations. Due to the along shore flow to the west, and the overall tendencies of Loop Current Eddies to drift northwest, the north and west sections of the domain are routinely well covered by actual data sources, so no sampling sites are active there. In trials with sampling included, the area around each designated sampling site is examined. If a real observation is located within a given radius (typically about 3 grid spacings or 30 km), then no model data is substituted at that site. If the radial search indicates the sampling site is in a data sparse area, the u and v components from the MODAS analysis at that point are inserted.

Computational problems develop along irregularly shaped segments of the numerically constructed coastline. In the interior, centered finite differencing methods compute the required eigenfunction gradients. The coastline, however, necessitates the use of single-sided techniques while balancing against an imposed "no flow-through" condition. Occasionally this generates very high current velocities at the coastal boundary points, especially at areas where a small coastal outcropping or inlet is modeled with less than three grid points per side. A coastal filter masks this problem by re-setting to zero any computed velocity exceeding 10 cm-s^{-1} on a coastal boundary point. No observations so close to shore were included in the data set.

Having determined the appropriate number of modes, the correct degree of simulated observation sampling must be fixed. A NMA nowcast with no sampling on 22 Jan 94 is compared to the MODAS run for the same day in Figure 14. The troubling feature of the nowcast is the large velocity region appearing in the southeast

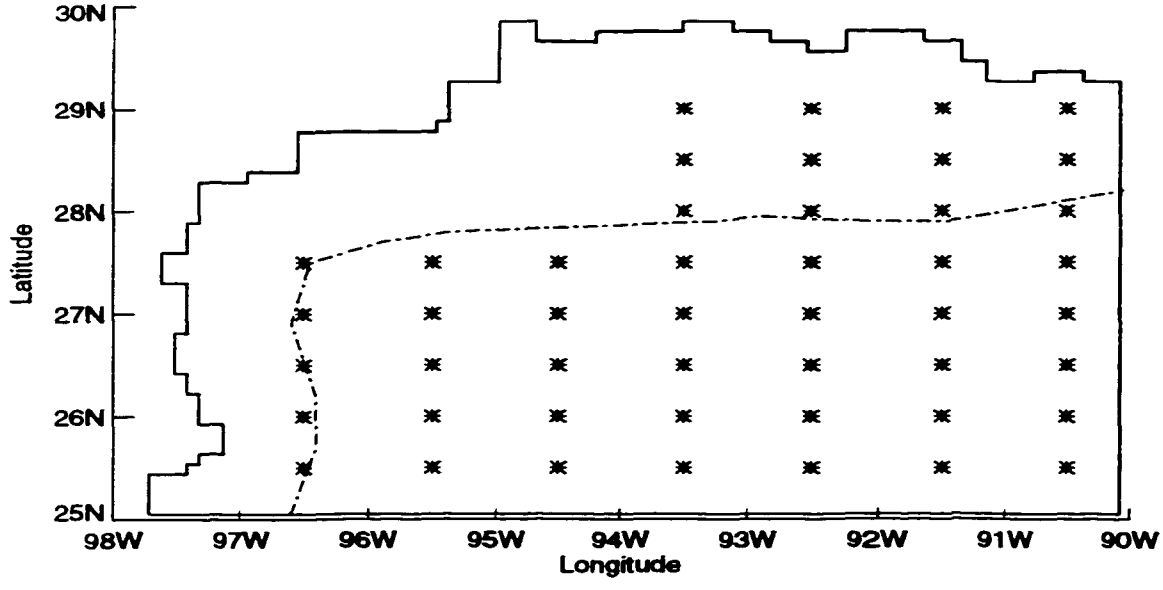

Figure 13: Potential sampling sites. Positions marked by asterisks are the sampling points on the NMA grid. The dotted curve approximates the 200 meter contour.

corner. Along the eastern edge of the domain, this unrealistic flow actually reverses the weak boundary flow provided by MODAS. In other areas, the NMA depiction seems reasonable. The northern along shore current is well modeled by NMA, but practically ignored by MODAS. A loop current eddy is well defined in the central southern region by NMA. MODAS' depiction suggests the feature may still be a meander for the Loop Current and not yet a separate feature, which would be an unusual situation so far westward.

The overly strong anticyclonic eddy in the east has few observations nearby to constrain its behavior or verify its existence. The other features, however are consistent with available observations. Figure 15 shows the differences between observations and NMA analyses (top panel) and MODAS analyses (bottom panel). The NMA nowcast shows better magnitude agreement, with differences averaging 5.89 cm-s^{-1} (u) and 6.06 cm-s^{-1} (v) compared to MODAS' 18.36 cm-s^{-1} and 13.86 cm-s^{-1}. A degree of quality on directional modeling may be inferred from a correlation scatter plot of the observations, shown in Figure 16. At observation locations, NMA shows much higher correlations than MODAS, suggesting good matching in both magnitude and direction.

Although the trial worked well in the shallow water areas which are handled poorly by MODAS, and near dynamic deep water features when provided with observations, the large vectors in the southeast makes the resulting overall surface current depiction unacceptable. By invoking the sampling procedure, the velocity excesses are eliminated. The NMA nowcast in Figure 17 uses a sampling factor of 6 (inserts a modeled observation at the designated point if there are no observations within 60 km). The excessive velocities in the southeast are diminished, but still strong enough to reverse the flow imparted at the eastern boundary. The along shore current and Loop Current Eddy in the southwest are still well modeled. The average differences (6.20 cm-s^{-1} u and 6.40 cm-s^{-1} v) are comparable to the no-sampling

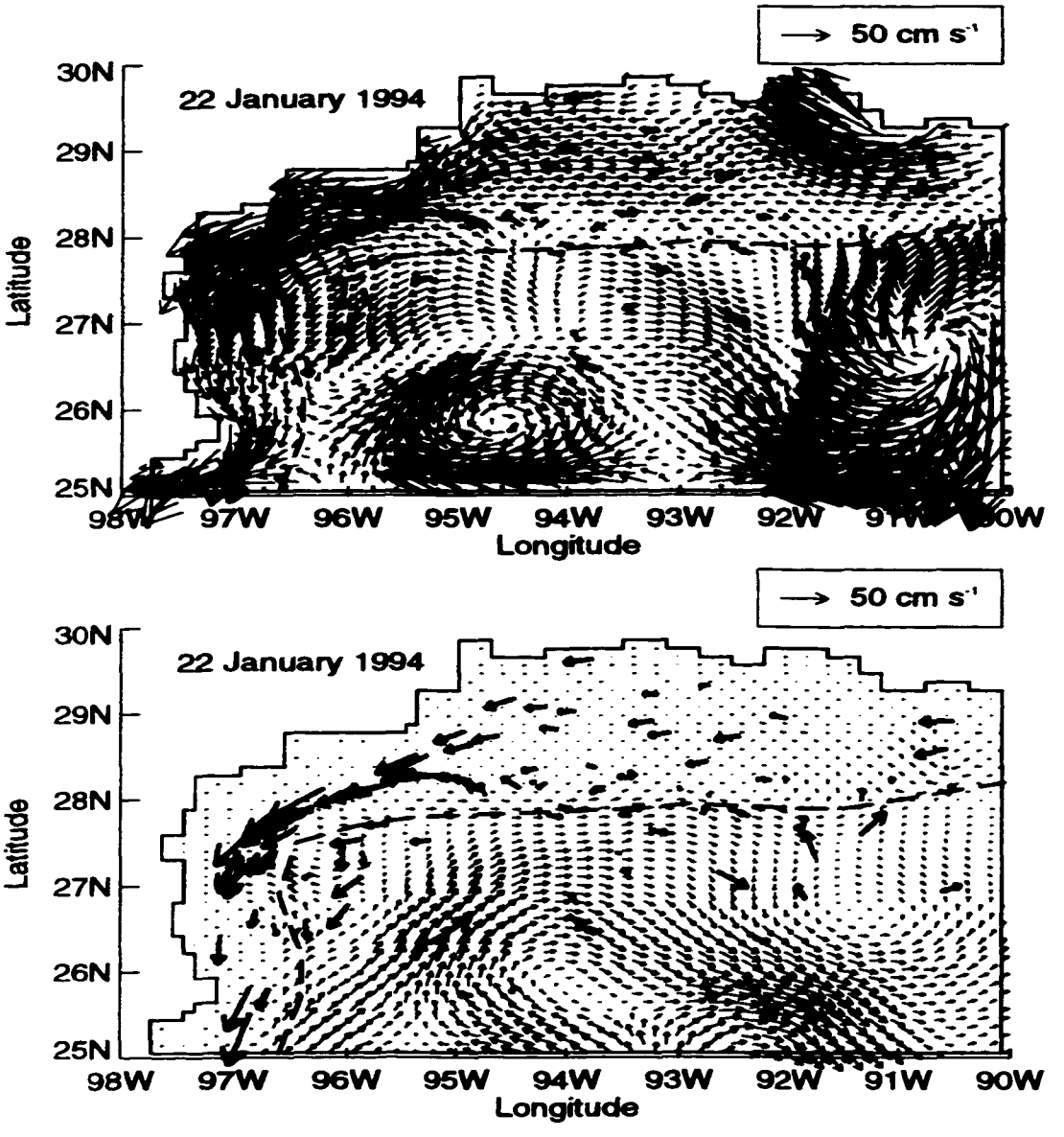

Figure 14: NMA nowcast without sampling (top) and MODAS analysis (bottom) for 22 January 1994. Observations are overlaid as thick red arrows.

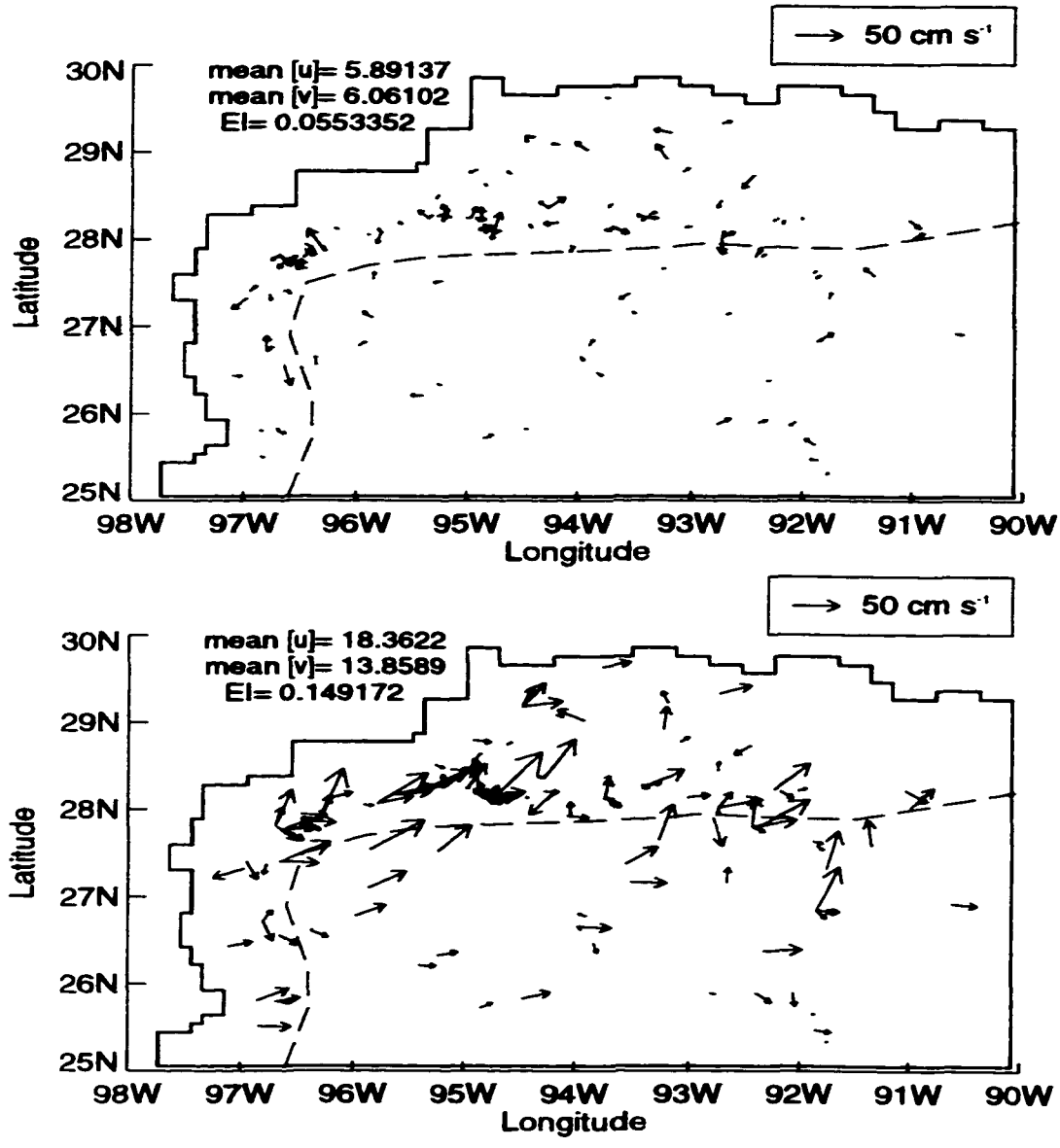

Figure 15: Difference plots for 22 January 1994 with no sampling. NMA minus Observations (top) and MODAS minus Observations (bottom), with mean differences in cm-s^{-1}.

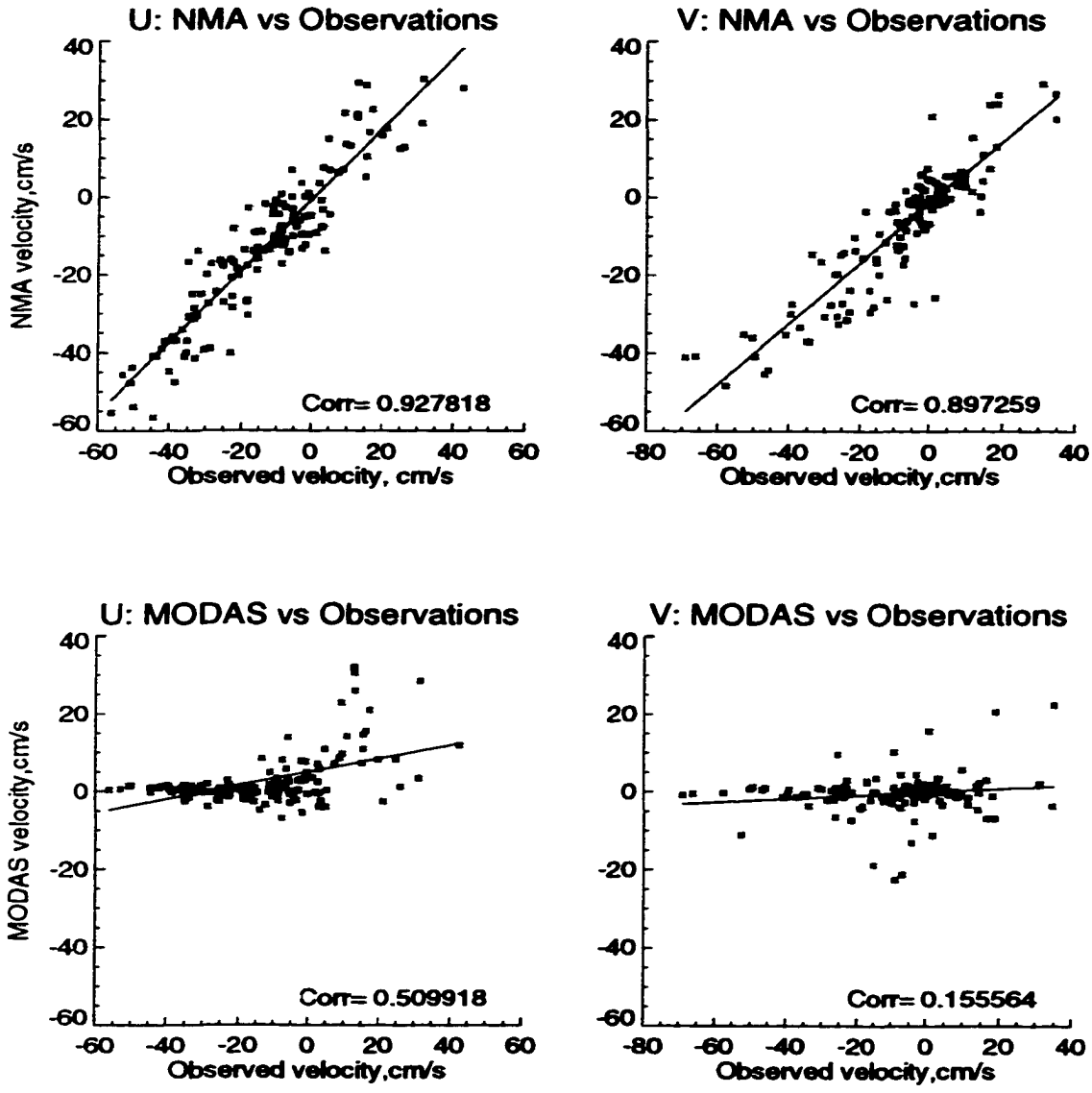

Figure 16: Correlation between computed and observed velocities for 22 January 1994 without sampling.

case. The correlations are also comparable, but slightly reduced (0.91 u and 0.88 v) due to the ingestion of presumably lower quality simulated observations.

The reversal of boundary flow in the east contradicts one of the entering assumptions in NMA; the provided boundary data is generally correct. Further adjustment to the nowcast leads to a trial with a higher degree of sampling. In Figure 18, the NMA nowcast includes a sampling factor of 3 (the testing radius is cut in half). The along shore flow is still reasonably modeled, the Loop Current Eddy is not as strong but is still defined as a closed circulation, and the boundary flow in the east is in fair agreement with the entering data. The baseline scenario now consists of a 58 mode (29 Dirichlet and 29 Neumann modes) trial with a sampling factor of 3. For the Winter trials, mean NMA correlations were 0.7778 (u) and 0.73401 (v), compared to mean MODAS correlations of 0.3278 (u) and 0.1218 (v). Mean Error Index values were 0.109 (MODAS) compared to 0.0608 (NMA).

Before conducting trials across the entire Winter period, a similar analysis of two more specific days verifies the "robustness" of the selected parameters. The days chosen have significant differences in computational considerations. On 8 December 93, the data quantity is moderate (98 drifters and 12 current meters), but MODAS suggests the presence of strong dynamic features. Conversely, on 19 March, there is nearly a minimum of both observational data (60 drifters, 17 meters) and dynamic forcing.

The 8 December MODAS depiction in Figure 19 (bottom) indicates a wide but not overly intense Loop Current Eddy just southwest of the region's center, as well as strong anti-cyclonic flow in the southeast. Again, as the overlaid observations indicate, the along shore flow is missed. The NMA depiction displays the eddy as a tighter closed off circulation covering a reduced area. NMA includes the effects of the two easterly observations in the southwest which counter MODAS' assertion on the size of the eddy circulation. Flow at the boundaries looks reasonable. The

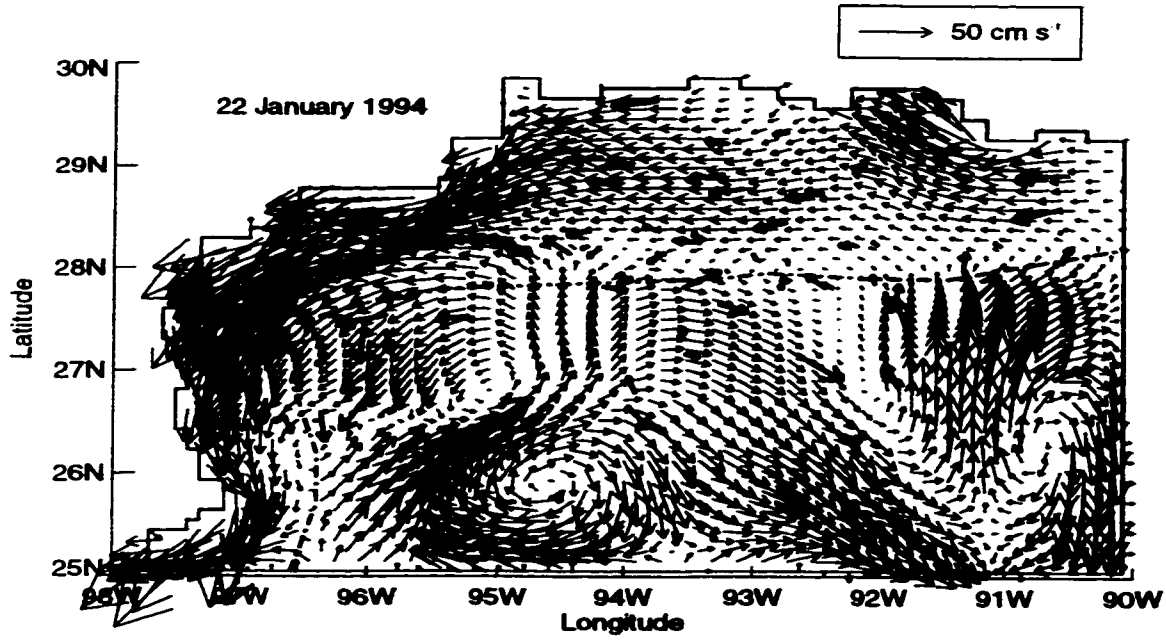

Figure 17: 22 Jan 94 NMA nowcast, 58 modes with sampling factor 6. Observations are overlaid as thick red arrows.

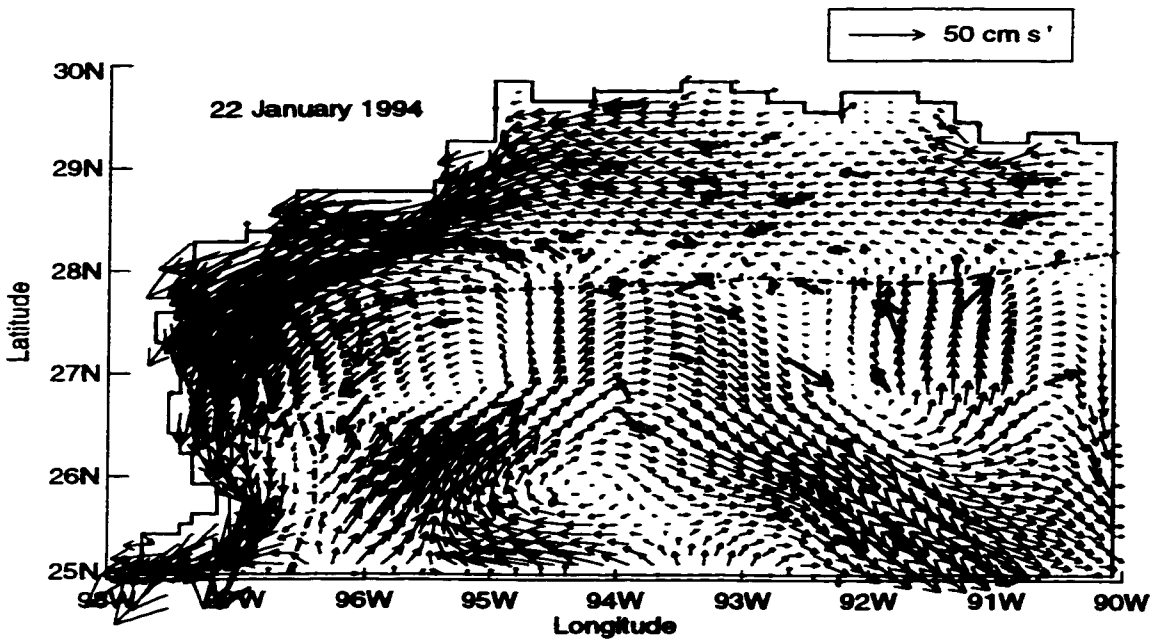

Figure 18: 22 Jan 94 NMA nowcast, 58 modes with sampling factor 3. Observations are overlaid as thick red arrows.

difference vectors have mean magnitudes of 5.23 cm-s^{-1} u and 3.81 cm-s^{-1} v for NMA compared to MODAS' 10.13 cm-s^{-1} u and 6.31 cm-s^{-1} v. Correlations for the NMA nowcast (.79 u and .74 v) are not as impressive as in the 22 January case, but still more than double the MODAS correlations. The suggested mode and sampling combination thus presents a usable depiction.

In Figure 20 (top), buoys on the shelf on 19 March 1994 support the NMA depiction of a distinct westward current. However, this forcing is much weaker than the previous cases examined, and again not modeled by MODAS (shown in the bottom panel). Offshore, weak intrusions of LCE's are detectable, but frequently the analyzed currents run counter to the overlaid observations. In such a weak forcing environment, there is less of a difference in the magnitude errors. NMA computes difference errors of 6.61 cm-s^{-1} u and 5.55 cm-s^{-1} v compared to MODAS' 9.83 cm-s^{-1} and 8.24 cm-s^{-1}, respectively. More revealing are the correlation plots shown in Figure 21, where the v components in MODAS are negatively correlated with the observations. Again, the conclusion stands that the 29 Dirichlet, 29 Neumann, sampling factor 3 (hereafter, "29D29N3") trial provides a suitable depiction.

Characteristics of the complete 29D29N3 run are displayed in Figure 22 through Figure 24. First, Figure 22 shows the error index for both analysis methods. The error index (EI) serves as a gross magnitude error check, and is defined as:

$$EI = \frac{1}{N}\sum\frac{1}{2}\left(\frac{|u_{comp} - u_{ob}|}{54} + \frac{|v_{comp} - v_{ob}|}{54}\right) \tag{21}$$

where u_{comp} and v_{comp} are the NMA or MODAS computed velocity components, N is the total number of observations, and 54 is chosen as the maximum expected surface velocity, 54 cm-s^{-1}, associated with hurricane passage as in Section 1. Thus, when the error index is zero, the computations agree precisely with the observations. An EI of unity indicates a difference equivalent to hurricane winds in the

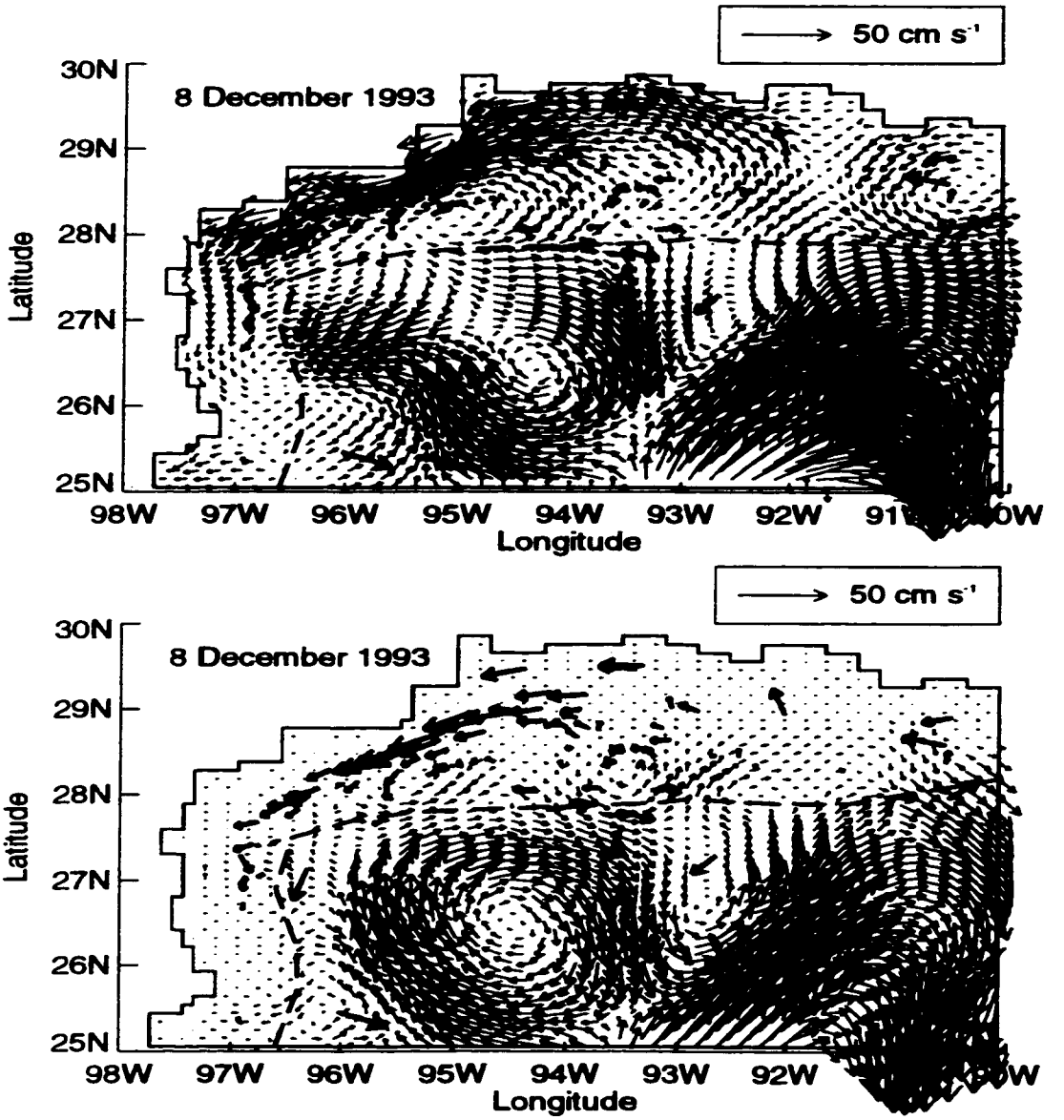

Figure 19: NMA nowcast with sampling factor 3 (top) and MODAS analysis (bottom) for 8 December 1993. Observations are overlaid as thick red arrows.

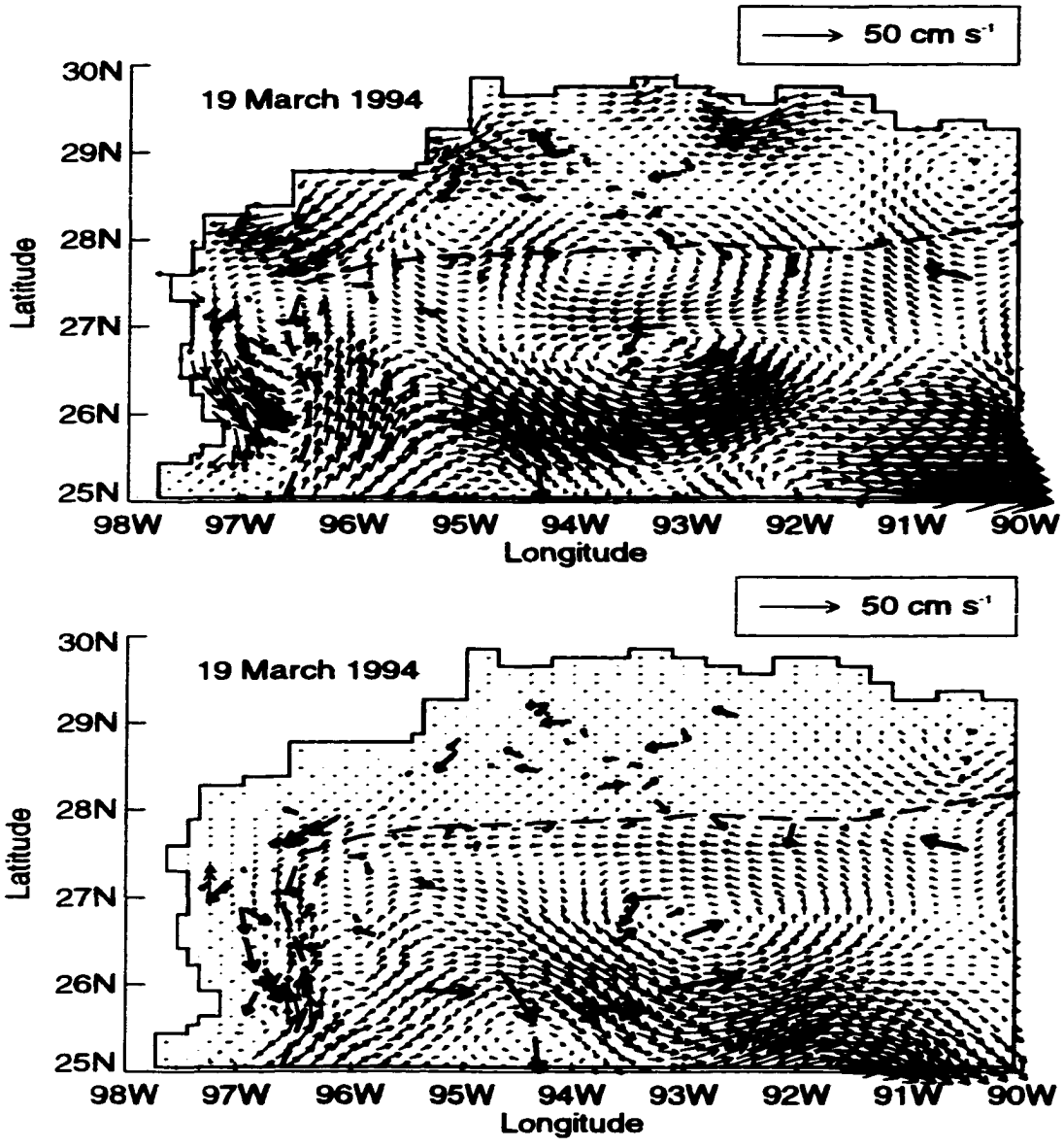

Figure 20: NMA nowcast with sampling factor 3 (top) and MODAS analysis (bottom) for 19 March 1994. Observations are overlaid as thick red arrows.

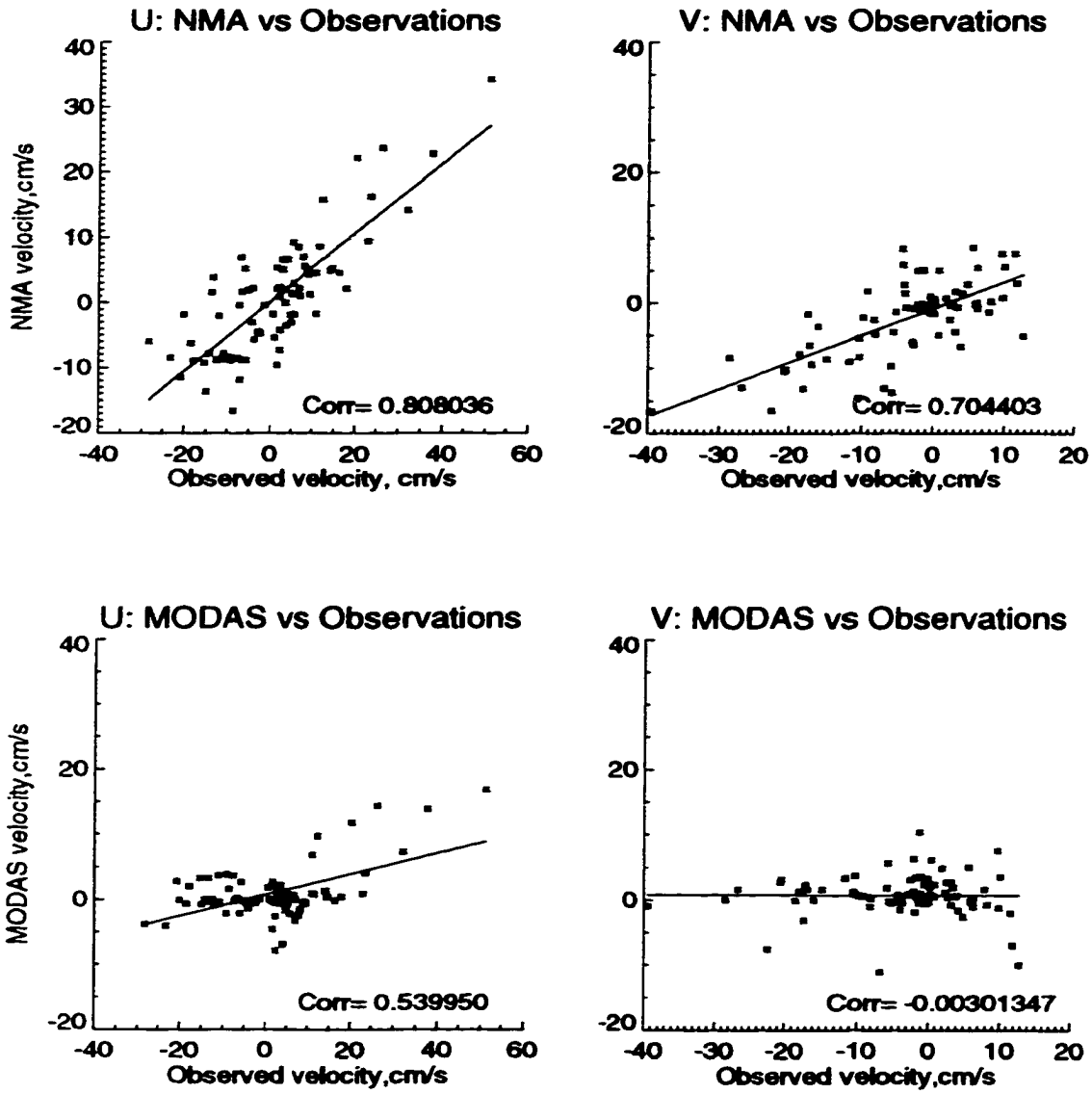

Figure 21: Correlation between computed and observed velocities for 19 March 1994 with sampling factor 3.

same direction, and an EI of two equates to a difference comparable to hurricane winds in the opposite direction. Large spikes in the EI plot serve as one indication that a buoy or current meter reported erroneously on a certain day. On such days, data may be considered "noisy", and the data-smoothing nature of a blending technique such as NMA is most advantageous. Large plateaus of high EI values indicate prolonged periods of large differences between the NMA or MODAS velocities and the observations. Assuming that the buoys and current meters generally report reliably, such plateaus indicate computational errors in NMA or analysis deficiencies in MODAS. Figure 22 shows the consistent superior magnitude analyzing performance of NMA. The progressively higher maxima may suggest a general increase in data noise through the trial, but likely stems from fewer observations available near the end of the period.

NMA correlation scores remain above the MODAS scores through the trial. Figure 23 displays the u (top) and v (bottom) correlation coefficients for each day in Winter. NMA is consistently above .5, and predominately above .7, where MODAS rarely exceeds .5 and occasionally returns negative correlations. As a final check on the numerical stability of each day in the trial, the maximum amplitudes of each day's Dirichlet and Neumann series are plotted in Figure 24. Any values exceeding 54 cm-s^{-1} would be highly suspect and likely result in a resonance somewhere in the domain, but for the 29D29N3 trial, all days indicate well behaved amplitudes between 2 and 14 cm-s^{-1}.

5.3 Reduced Mode Trials

Sensitivity of the NMA method is studied in trials involving fewer modes chosen by various selection procedures. In developing these procedures, emphasis shifted between accounting for the dominant energy modes and matching the mode resolution to the size of expected physical features. *L99* showed lower-numbered modes,

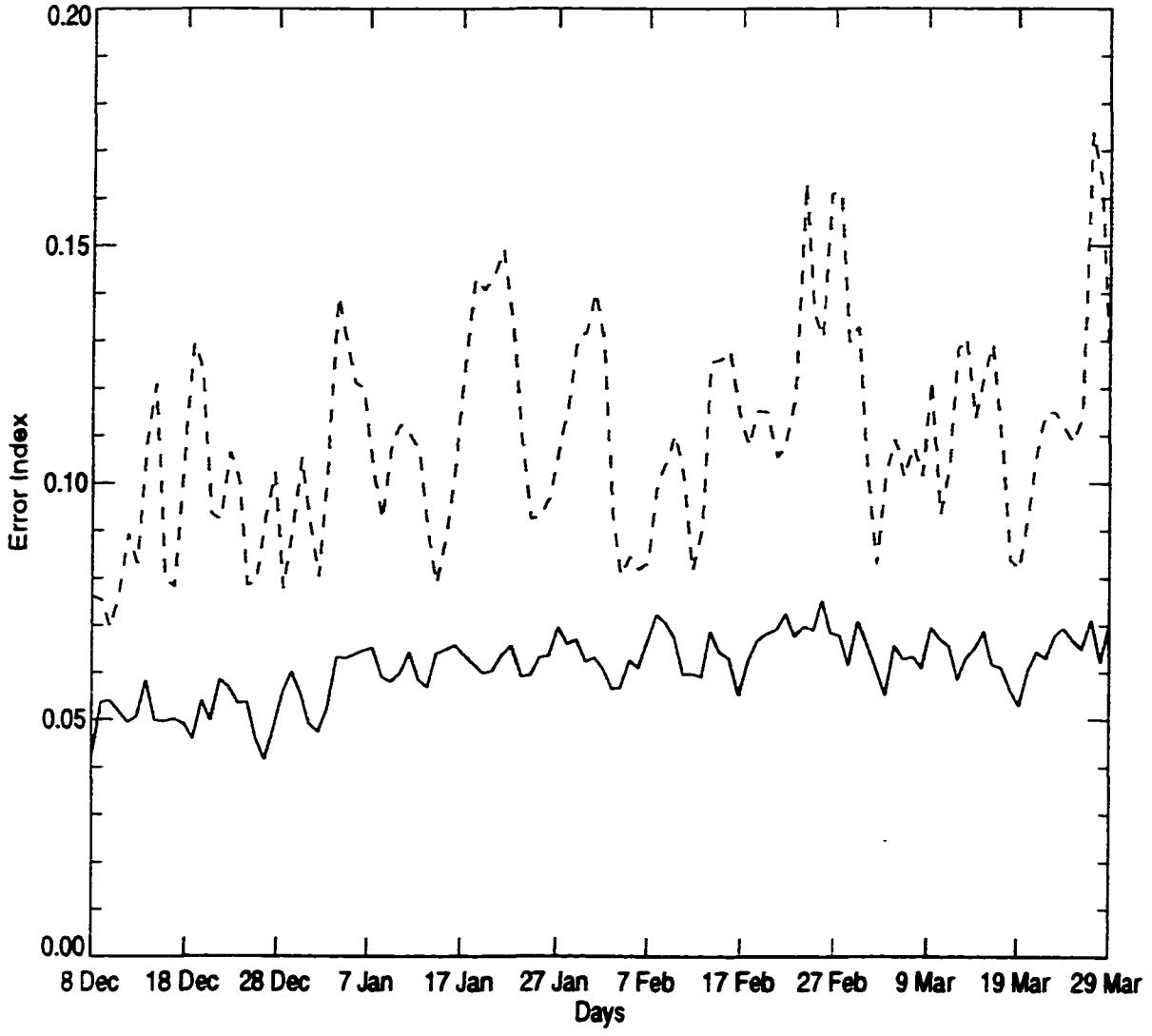

Figure 22: Error index for the 29D-29N-3 Winter trial. NMA (solid) and MODAS (dashed) displayed.

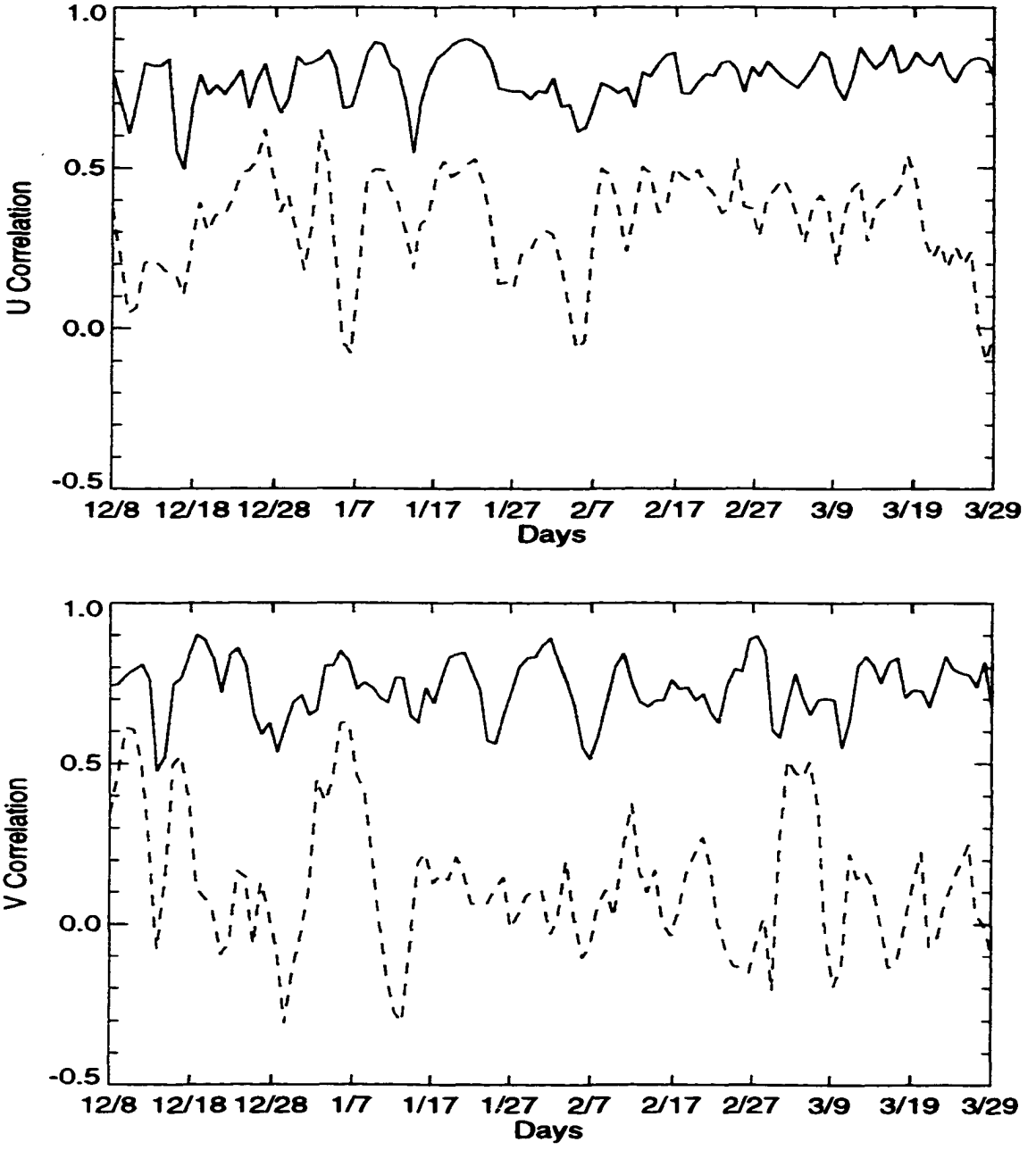

Figure 23: Daily correlation results for the Winter baseline trial. NMA correlation coefficients follow the solid line, MODAS coefficients follow the dashed line. The upper figure displays the U-component results; V-components in the lower panel.

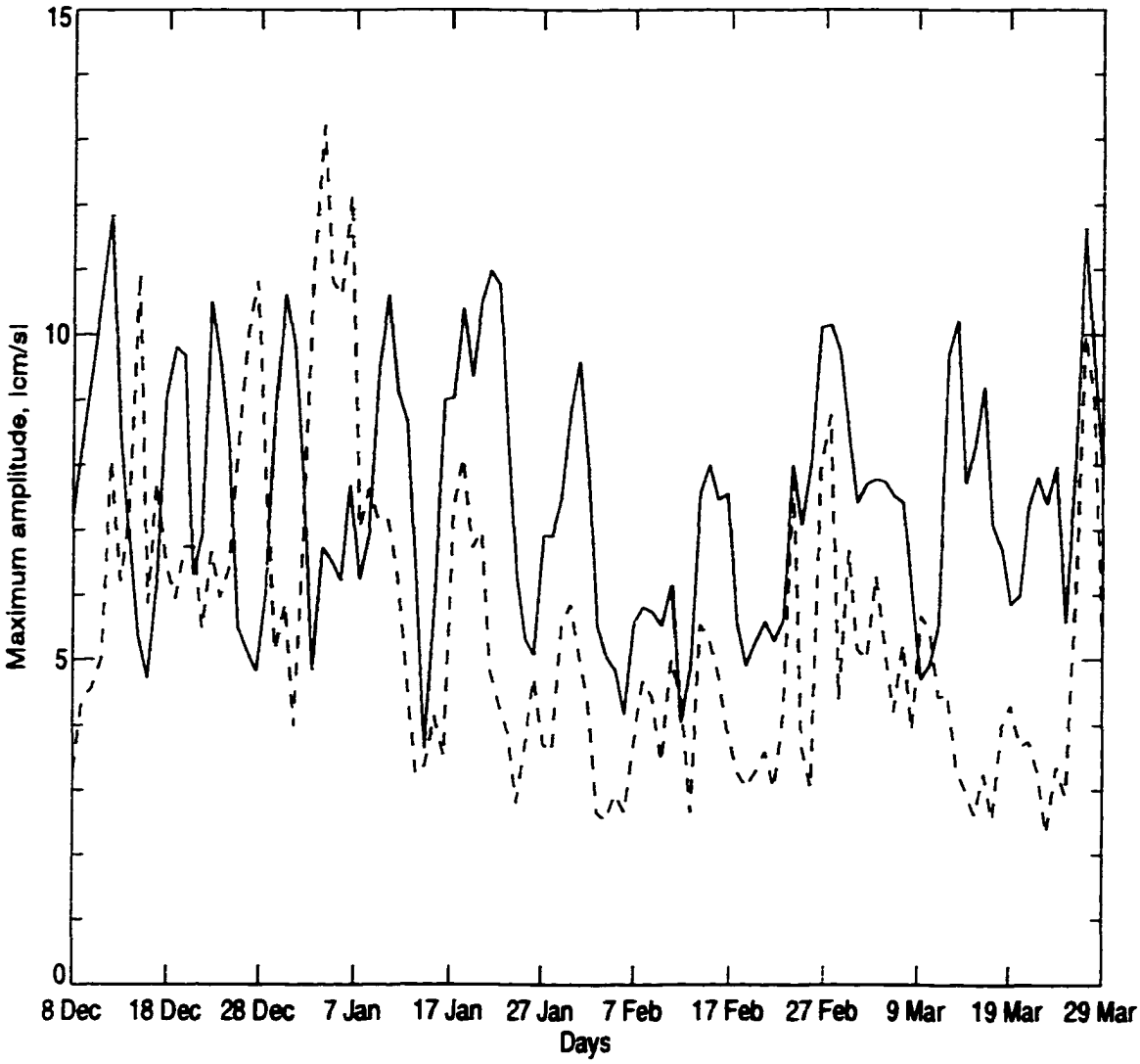

Figure 24: Maximum daily amplitudes for the Winter 29D-29N-3 trial. Dirichlet(solid)and Neumann(dashed) modes displayed.

analogous to longer, low frequency waves, are generally more energetic. In scenarios where large dynamic features dominate, trials relying primarily on larger modes should successfully represent these features. However, modeling quality may be diminished if small scale features are neglected. These features are often best re-created by the less energetic but structurally more complex higher modes. A balance is sought, as the NMA analyst must guard against inclusion of too many higher modes. These will introduce spurious circulation features into the surface map unless assimilation of sufficient observations constrains the calculation.

Evaluation of the trials conducted proceeds along two lines. First, the results are objectively examined by comparing the correlation coefficients and Error Index values. Second, surface maps from various trials are compared subjectively based on how the nowcast compares to the deep water structure depicted by MODAS, the climatologically expected features in the region, and the available observations. The three dates used in determining the sampling criteria are used here since they represent three different application scenarios for NMA. January 22 1994 has abundant observations and significant dynamic forcing features. December 8 1993 is relatively data-poor, but still subjected to significant forcing, and March 19 has neither large quantities of data nor strong dynamic features.

In January, expected features described by *Cochrane and Kelly* [1986] and shown in Figure 1 include a cyclone confined to the shelf centered south of Galveston, the Texas Current moving continuously from Sabine Pass to Aransas Pass and a distinct eastward shelf break current. For 22 January 1994, the MODAS analysis in the bottom panel of figure 14 indicates a large anticyclonic eddy centered near 26°N 94°W . The observations for that date document the presence of the Texas Current.

In addition to the MODAS and baseline (29D-29N-3) trials, these features were sought in nowcasts generated through ten different methods. Of these, seven methods (all conducted with sampling factor 3) yielded enlightening results:

- The *Random* trial involved 10 randomly selected Dirichlet and 10 randomly selected Neumann modes.
- The *Lower Neumann* trial consisted of Neumann modes 1 through 20 and Dirichlet modes 1 through 10.
- The *Lower Dirichlet* trial consisted of Dirichlet modes 1 through 20 and Neumann modes 1 through 10.
- A *High Amplitude* trial used the 10 Dirichlet and 10 Neumann modes displaying the largest magnitude amplitudes.
- The *Best Frequency* trial employed all modes which displayed frequencies indicated as significant in the current meter and buoy analyses, as well as frequencies expected from the dynamic features as described in Section 4. This involved 25 Dirichlet and 20 Neumann modes.
- The *Reduced Frequency* trial, involving the 15 lowest Dirichlet and 15 lowest Neumann modes from the Best Frequency experiment.
- The *Minimum Frequency* trial, involving the 10 lowest Dirichlet and 10 lowest Neumann modes from the Best Frequency experiment.

The remaining three methods based on the 10 lowest mode numbers, the 10 highest mode numbers, and sampling every third mode provided poor representations of the region. Results of these trials are not displayed or tabulated. The Best Frequency, Reduced Frequency and Minimum Frequency trials are considered frequency selection trials. The High Amplitude, Lower Neumann and Lower Dirichlet are amplitude selection trials. The objective results are listed in Table 1. Below the MODAS data, the experiments are listed in descending order of their objective depiction quality.

In selecting modes for the Best Frequency trial, times series of each mode's amplitude were spectrally analyzed, again by Lomb's method, and their most significant frequencies recorded. From Section 4, frequencies chosen to represent known physical processes are 0.15, 0.25, 0.43, 0.48, 0.53, 0.6, 0.67, 0.75, 0.86 and 0.95 cpd. Although the histograms in Figures 6 through 9 show numerous peaks above the significance line, some may be artifacts of Lomb's method. While that method is well suited for irregularly spaced data in a record, the analysis here involves multiple records of varying lengths, since some buoys drifted and reported for months while others latest only a few weeks. This must be considered before attempting to select significant peaks from the histograms. As an example, if the frequency of interest is near 0.2 cpd there are 18 cycles in a 90 day record. Assuming a conservative 5% variability, the range actually extends from 17.1 to 18.9 cycles in the record. This implies that detected frequencies from .19 to .21 cpd indicate the same forcing mechanism. The same variability assumed around a 0.8 cpd signal produces a window of 0.76 to 0.84. Thus, the cluster of spikes around the inertial period in the current meter histograms can only indicate actual frequencies to within roughly 0.02 to 0.05 cpd.

Modes displaying significant frequencies closest (i.e., within 0.02 cpd for frequencies below 0.5 cpd, and within 0.05 cpd for frequencies above 0.5 cpd) to the expected frequencies included Dirichlet modes 2 through 8, 10, 11, 13 through 16, and 18 through 29 plus Neumann modes 1,2,4 through 6, 8, 11, 13, 14, 16 through 19, and 22 through 28. Notably, none of the frequencies sought above 0.53 were captured, and only Neumann mode 19 matched the 0.35 to 0.48 cpd range. Yet, in this 45 mode trial, 20 of the components were from modes 14 or lower, while 25 came from mode number 15 or higher. This paradoxical relationship between low frequencies and higher mode numbers produced some of the most successful reduced-mode nowcasts.

Table 1: Objective analyses for 22 January 1994.

Trial	Total Modes	u-corr	v-corr	Error Index
Comparative sources				
29D-29N-3 baseline	58	.9011	.8449	.0635
MODAS		.5099	.1556	.1492
Experiments				
Best Frequency	45	.8855	.8200	.0679
High Amplitude	20	.8740	.8197	.0715
Lower Neumann	30	.8645	.8086	.0709
Reduced Frequency	30	.8643	.7869	.0725
Lower Dirichlet	30	.8518	.7781	.0748
Minimum Frequency	20	.8476	.7661	.0755
Random	20	.7578	.5684	.0975

The best subjective trials coincided with the top objective scores on this run. That the Best Frequency method performed well is not surprising, since that trial used the most modes and, by virtue of the frequency selection process, involved the most physically representative input. The second best method, however, used the lowest number of modes. The High Amplitude depiction shown in Figure 25, shows a shelf cyclone centered near 28°N 93°W while giving a fair representation of the Texas Current. The predominately low mode numbers used here also capture the Loop Current Eddy centered near 26°N and 94.2°W. Open ocean boundaries are consistent with the MODAS boundary flow. In less successful trials using a small number of modes, NMA generated unreasonably large values at the open ocean boundaries, sometimes even opposite in direction from the modeled inputs. Such large amplitudes signal an unreliable experiment, suggesting that severely over-determining the matrix problem described by (12) and (13), leads to an insufficient number of iterations of the error minimization process in (14). When the resulting large error is allowed, the boundary solution terms in (10) are overshadowed, which leads to the generation of erroneous values at the boundary points.

The misleading depiction of a cyclonic gyre centered near 27.2°N 95.5°W stands

out as the most significant detractor in this trial. From *Oey* [1995], detached LCE's rarely survive in such a vigorous symmetrical state so far west. Additionally, the NMA analysis greatly underestimates the southward flow of 20 to 25 cm-s^{-1} reported by two drifters near 27°N 96°W in Figure 25. The spacing between the southwesterly observations caught in the Texas Current at the narrowest portion of the shelf near Aransas Pass, and the northeasterly observations in the shelf break current allows the fitting of circular features resolved by Dirichlet modes 7 through 10. The trial fits a circular eddy in this space, highlighting surface NMA's inability to consider bathymetry. The 200 meter bathymetric contour runs through the center of this 'eddy', also an improbable occurrence according to *Oey* [1995].

Applying the same tests to the 8 December 1993 High Amplitude case, shown in Figure 26, allows a similar analysis. Expected December circulation features noted by *Cochrane and Kelly* [1986] include a zonally elongated cyclone on the Texas Shelf centered directly south of Galveston. The westward moving shoreward limb of this cyclone drives nearly to the coast, interrupting the Texas Current. Thus, one expects two branches of the along shore current, one heading west along the Louisiana coast and another heading south along the Texas shoreline. In deeper water, the shelf break current is well defined along the east-west oriented section of the 200 meter contour, unless temporarily disrupted by Loop Current Eddies. The MODAS analysis for early December indicated a large LCE centered near 25.56°N 95°W which did not begin to dissipate until mid-December. The LCE enhanced the shelf break current along the western half of the shelf break as expected. The shelf break current quickly diminishes east of the LCE as the southward circulation around the eastern limb established a divergent region along the break. The shelf break current strengthens east of 92°W, upon coinciding with a meander from the Loop Current.

The seven trials in Table 2 are listed in order of both objective and subjective

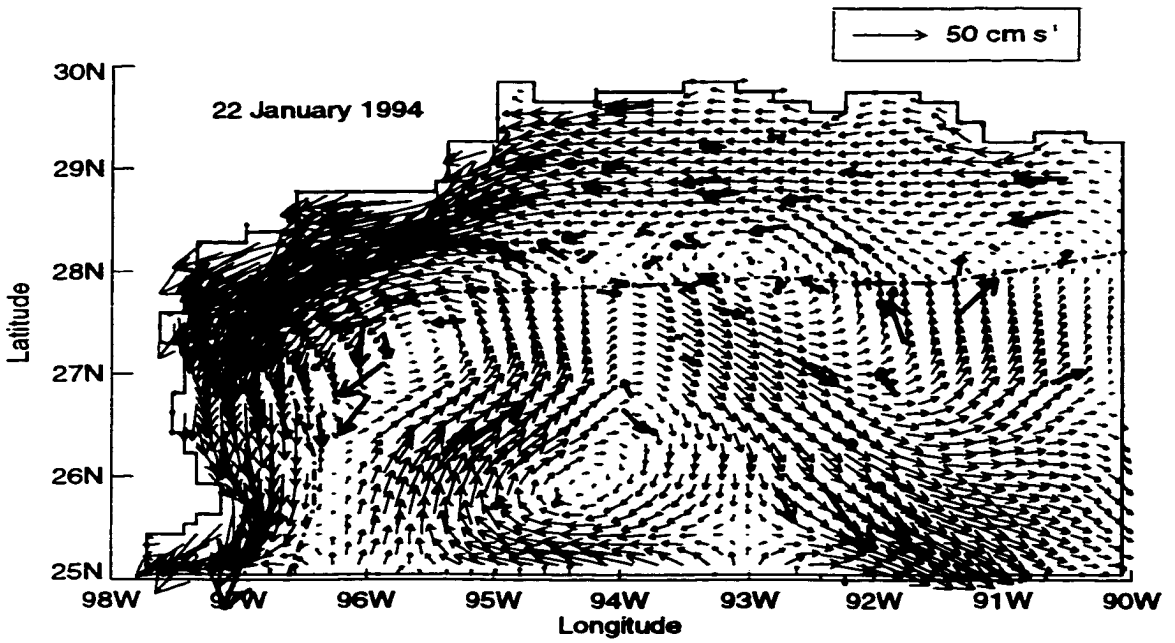

Figure 25: 22 Jan 94 NMA High Amplitude nowcast. Observations are overlaid as thick red arrows.

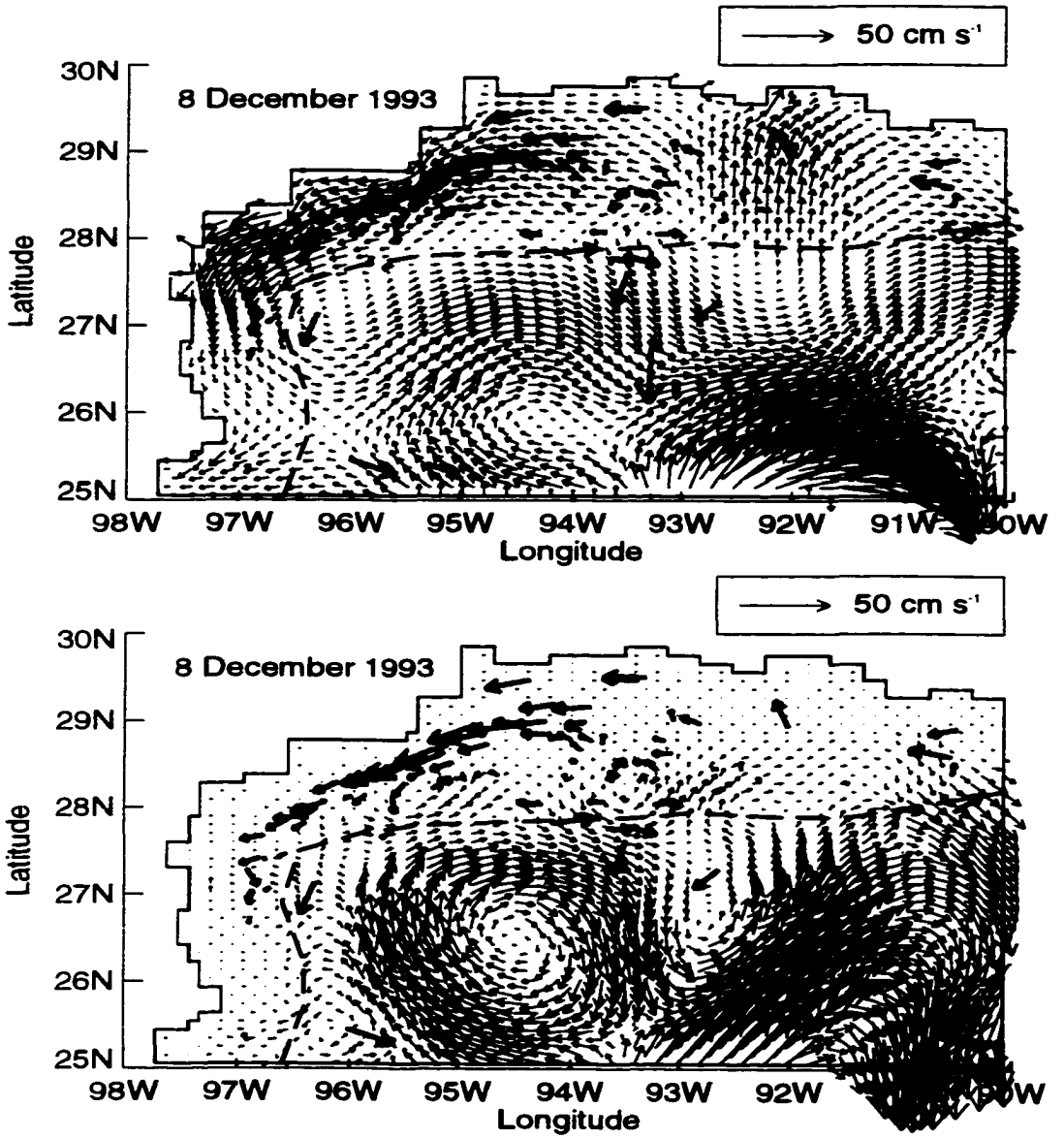

Figure 26: NMA High Amplitude nowcast with sampling factor 3 (top) and MODAS analysis (bottom) for 8 Dec 1993. Observations are overlaid as thick red arrows.

Table 2: Objective analyses for 8 December 1993.

Trial	Total Modes	u-corr	v-corr	Error Index
Comparitive sources				
29D-29N-3 baseline	58	.7871	.7430	.0419
MODAS		.3736	.3454	.0762
Experiments				
Best Frequency	45	.7642	.7263	.0454
Lower Dirichlet	30	.7311	.7077	.0451
Reduced Frequency	30	.7290	.6783	.0466
Lower Neumann	30	.7220	.6482	.4790
High Amplitude	20	.7053	.6471	.0504
Minimum Frequency	20	.6986	.6142	.0485
Random	20	.6754	.4469	.0538

quality. All non-random trials recorded u-velocity correlations between 69% and 76%. V-correlations covered a wider range (61% to 72%) and dropped off faster as the quality of the run decreased. Note the correlation statistics for the random trial drops to .4469 for v but only to .6754 for u. Since the preponderance of observations are in a strong u oriented flow over the shelf, better correlations in that component are not surprising. As in the January 22 trial, the Best Frequency method produced superior results. The cyclonic flow on the shelf appears as expected, centered south of Galveston, but stretched elliptically northeast to southwest. Observation density is highest along the northeast limb of this feature and indicates a strong southwest flow, which coincides with the westward intensified branch of the alongshore current. An intrusion in the southeast corner suggests a Loop Current meander or another eddy approaching from the south.

While both Tables 1 and 2 agree on the success of the Best Frequency trial, a noteworthy difference is the juxtaposition of the High Amplitude and Lower Dirichlet trials. In December, Lower Dirichlet selection ranks second, while this method ranked fifth in January. Recall from (3) and (4) that the Dirichlet modes solve the Helmholtz equation by expanding on the gradients of a stream function, resulting

in modes without divergence. Reliance on these vorticity modes, as in the Lower Dirichlet trial, supports the fitting of circular vortex features at the expense of more laminar features. On 8 December, MODAS and observations highlight several vorticity-driven features. In deep water, the mature LCE in the west and developing meander (or nascent LCE) in the southeast are prominent enough to depict without the benefit of nearby buoy observations. On the shelf, fortuitous drifter placement combined with weak but identifiable modeled flow reveals two small cyclonic vortices. By comparison, the January analysis shows a strong laminar flow over the shelf without hints of smaller rotational structures, plus an absence of closed eddies in deep water.

The High Amplitude trial attained better relative performance in January, placing second, than in December where it placed fifth. In an amplitude driven trial, the most energetic (typically lower-numbered) modes are captured. One expects the amplitude-selected trial to perform well when a large part of the energy in the region is confined to a small group of low-numbered modes. This constraint implies that the High Amplitude trial should work well when only large scale features dominate the region. If smaller features such as shelf cyclones or estuarine plumes are expected, mode selection via high amplitudes may produce poor results as the smaller structures are smoothed out. Since the December analysis shows several smaller scale features as described above, the High Amplitude selection method is not appropriate.

Among the trials using a combination of 20 modes, the order was consistently Higher Amplitudes, Minimum Frequencies and Random. Random's consistent last place finish suggests that the employing the other methods produces improved analyses. Weaknesses of the High Amplitude method have been noted. Inherent weaknesses of the frequency selection method include the observing system's inability to detect every significant frequency, and reliance on climatologically expected forc-

ing signals. The disparity in spectral coverage between drifters and current meters shown in Section 4 documents the increase in significant frequencies evident when using the fixed meters. However, these Eulerian sensors were only moored over the shelf. It is possible that fixed sensors in deeper water would detect additional significant signals and improve the frequency trials' depictions. Additionally, the list of frequencies culled from the literature may be far from comprehensive.

Finally, comparison of the trials for 19 March 1994 illustrates the impact of light forcing and low observation density. Although weak and ill defined, expected features noted by *Cochrane and Kelly* [1986], *Vastano et al.* [1995] and *Vastano and Barron* [1994] include a long, thin cyclone on the shelf centered south of Sabine, slightly weaker than in December but now supporting a continuous Texas Current. An estuarine plume extending southeast from Matagorda supplements transport across the shelf, merging with a well defined shelf break current. More subtle features evident in spring include a surface convergence region near Padre Island and a small, cyclonic feature on the shelf near Brownsville. The results for the day are compiled in Table 3.

By objective measure, the trials in descending order of performance are Best Frequency, Highest Amplitudes, Reduced Freqeuncy, Lower Dirichlet, Random and Lower Neumann. Unexpectedly, Random placed above a "skilled" mode selection forecast. When ranked subjectively, as they are in Table 3 the top performer becomes the 30 mode Reduced Frequency trial, another surprising result.

The Reduced Frequency trial, shown in Figure 27 compared to the MODAS depiction, generates a continuous Texas current, a reasonably defined shelf break current in the west, and convergent flow near Padre Island. Flow along the open boundaries remains consistent with the MODAS forcing. A weak cyclone exists on the shelf centered south of Vermillion Bay, consistent with expectations that the shelf cyclone is farther eastward at this time of year. The beginnings of the shelf

break current in the west are well placed, as is a small LCE which was also evident in the MODAS analysis near 26.5°N 92.5°W. Two physically inconsistent depictions degrade the quality of this nowcast. A large, symmetric eddy is centered over the shelf break south of Sabine Pass, and a smaller well-shaped ring is centered over the shelf break east of Padre Island. Topographic interactions normally prevent rings from remaining intact as they impact the shelf. Despite this inconsistency, the Reduced Frequency nowcast produces the best overall map. The Best Frequency nowcast did not capture a cyclone on the shelf. The shelf break current and deep water eddy depictions are adequate in the Best Frequency nowcast, but again a large eddy is centered on the 200 meter contour.

At the bottom of Table 3, the poor performance of the Minimum Frequency trial stands out. In a situation with small scale features like the Padre Island convergence and the Matagorda Plume, trials without higher mode numbers generate expectedly poor nowcasts. The low observation density here amplifies the problem of employing only lower numbered modes. That deficiency combines with the low modes used in the Minimum Frequency trial to heavily bias the resultant nowcast towards a map filled by large scale, low amplitude features. The occasional higher modes included in the Random trial slightly compensate for this deficiency.

From the three sampled dates examined, frequency selection modes appear to work well. In all three situations (strong dynamics and numerous observations, strong dynamics and few observations, weak dynamics and few observations), frequency methods were the single best or one of the top two performers. In weakly dynamic scenarios, frequency methods can impose spurious circulation structures if too many modes are included. Amplitude methods are most useful in well-sampled situations, more so if an assumption can be made about the rotational character of the circulation expected over a given period. The assumption that nowcasts generated by more modes will outperform those generated by fewer modes fails, shown by

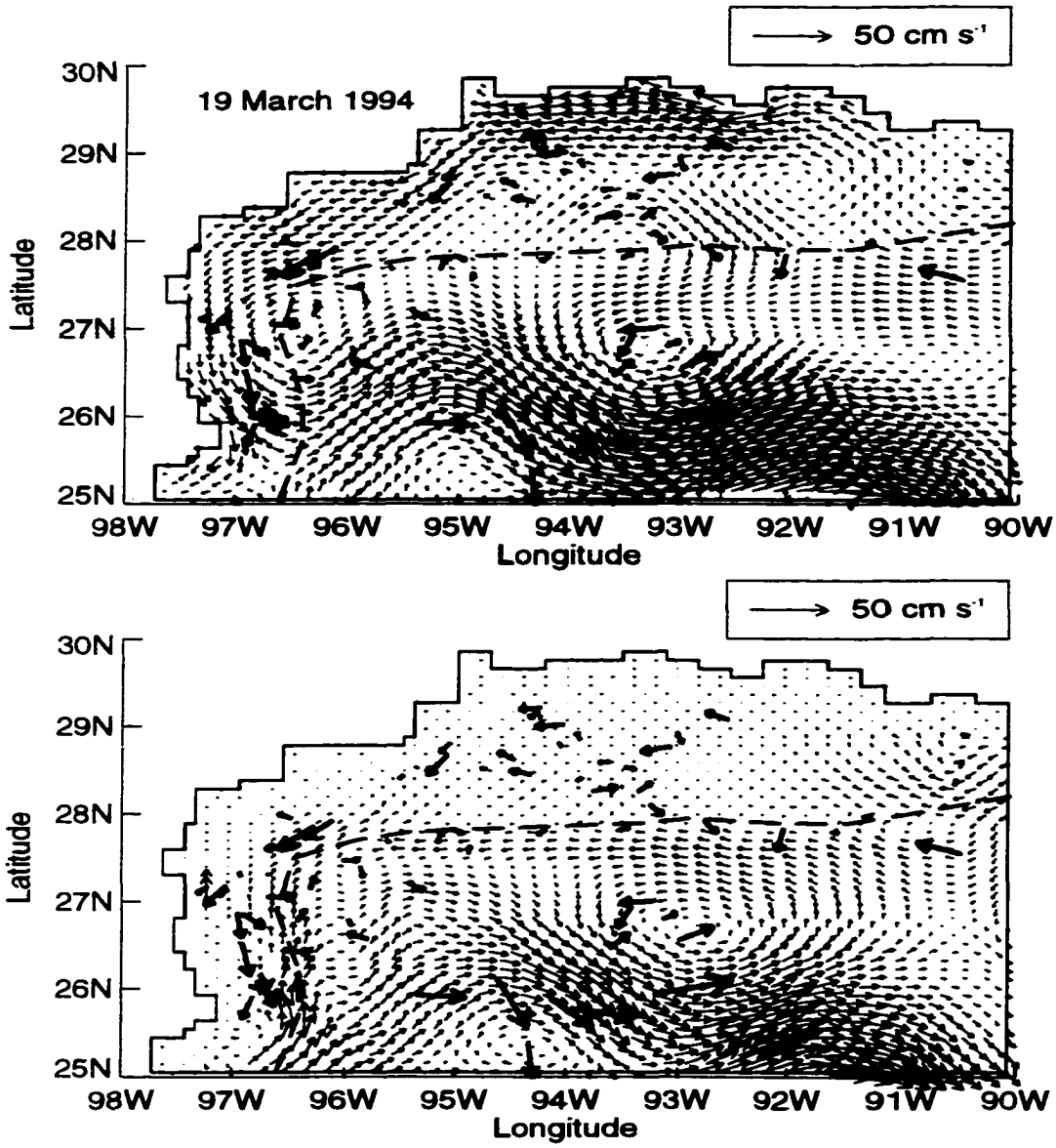

Figure 27: NMA Reduced Frequency nowcast with sampling factor 3 (top) and MODAS analysis (bottom) for 19 March 1994. Observations are overlaid as thick red arrows.

Table 3: Objective analyses for 19 March 1993.

Trial	Total Modes	u-corr	v-corr	Error Index
Comparitive sources				
29D-29N-3 baseline	58	.8080	.7044	.0563
MODAS		.5400	-.0030	.0837
Experiments				
Reduced Frequency	30	.7300	.6430	.0626
Best Frequency	45	.7929	.6105	.0584
Lower Dirichlet	30	.7191	.5715	.0633
High Amplitude	20	.7859	.6564	.0599
Lower Neumann	30	.7016	.5182	.0682
Random	20	.7559	.3163	.0680
Minimum Frequency	20	.6723	.3919	.0716

both the January and March trials, further suggesting that *a priori* oceanographic knowledge of a target area remains essential.

5.4 Comparative Analyses over the Entire Sampling Periods

In Section 5.3, the Best Frequency, High Amplitude, Lower Neumann, Reduced Frequency and Lower Dirichlet trials all, at least once, ranked in the top half of the comparison trials. All consistently outperformed the MODAS analysis in terms of correlation with observations and low error indices. Several came very close to matching the statistics of the baseline run as well. Here, through an F-test, the variance of the amplitude vectors generated in the reduced mode trials is compared to the baseline trial.

The amplitude vector under study is the right hand column vector in (12). The squared components of this vector are proportional to the energy distribution among the modes. Successful reduced mode trials should distribute the energy as the baseline trial does, and thus capture a significant portion of the baseline run's amplitude vector variance. For the 113 day Winter period, the amplitudes and frequencies

are chosen from the 22 January trial. It is assumed the abundance of observations centered around that day provided the most accurate look at the character of the area. The date also conveniently falls near the middle (day 46 of 113) of the studied period.

Figure 28 displays the F-test time series for the five most successful reduced mode trials. In each panel, the test reports, to a selected confidence level, whether the amplitudes from the reduced mode trial were distributed similarly to the amplitudes of the baseline trial. The thin horizontal lines represent the 50% (solid), 80% (dashed) and 90% (dotted) confidence levels. None of the trials consistently duplicate the variance found in the baseline trial, but certain trials outperformed others at various times, revealing sensitivities of the NMA process.

All the trials except Lower Neumann appear sensitive to high flow across the open boundary. The thick dotted and solid black lines in the five panels correlate to the net inflow charted in Figure 3. The solid line indicates a period of high (greater than 5 x $10^7 s^{-1}$) outflow, and the thick dotted lines mark periods of high inflow. At other times, the flow is below the threshold. Four of the five trials were consistently weak during the high outflow period. Most notably, this period includes 22 January. In such a domain, with fixed coastlines on two sides, such high surface outflow may imply increased surface divergence. Even optimally configuring the mode selection process for that day fails to overcome this strong forcing in the frequency selection and two of the amplitude selection modes. Recalling from Section 3 that the Neumann modes may also be termed divergence modes, the Lower Neumann trial's immunity to this effect is expected. In fact, the high outflow period is the only time the Lower Neumann mode consistently breaks the 50% level.

Overall, the frequency selection methods duplicate more of the variance than the amplitude selection methods. The mean variability of the F-statistic and variance about that mean are listed in Table 4, which shows that the Best Frequency and

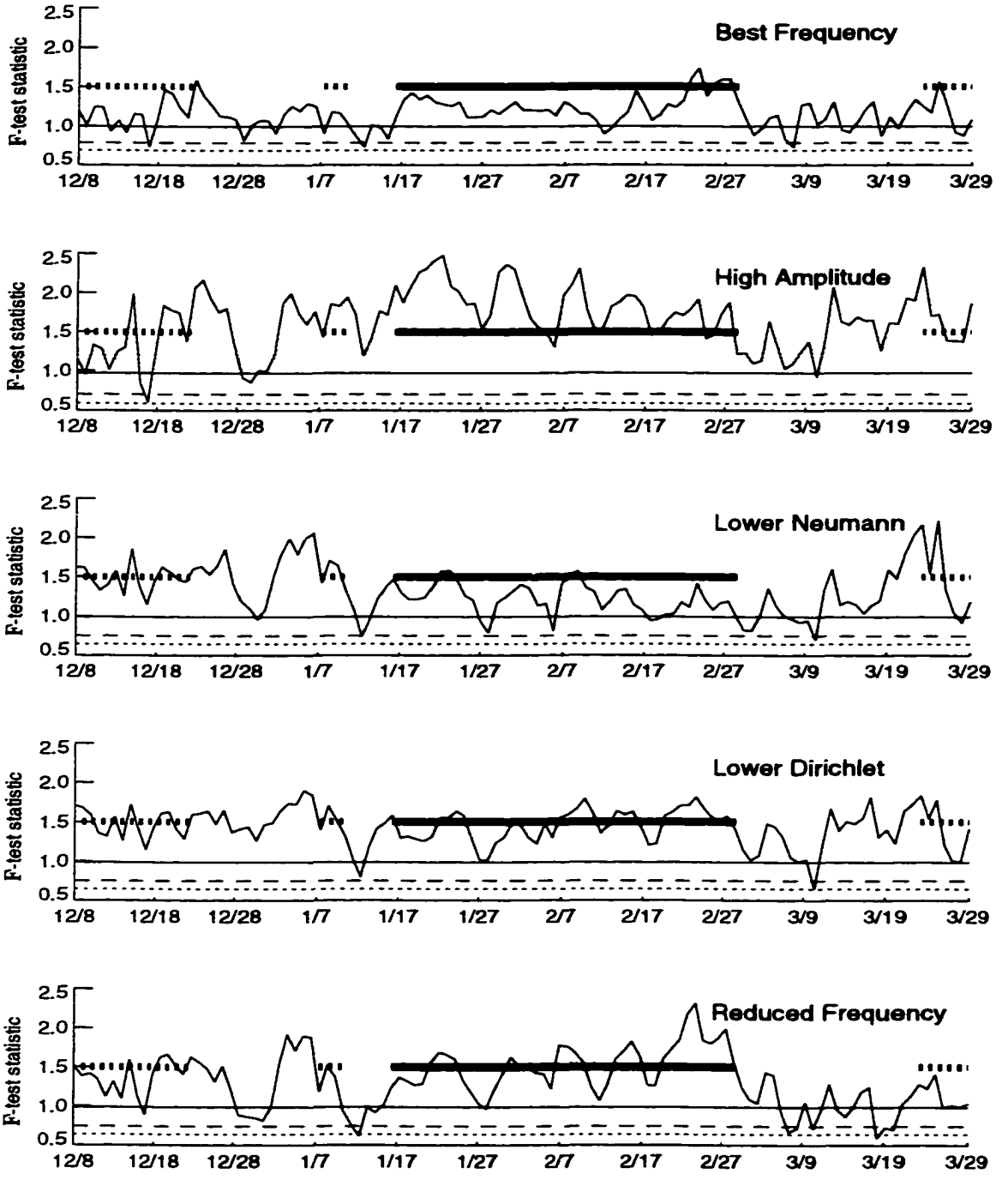

Figure 28: Variance analyses for five reduced mode trials (Winter). In each panel, the 50, 80 and 90 percent significance levels are indicated by thin horizontal solid, dashed and dotted lines respectively. Heavy dashed and dotted lines indicate periods of high cross-boundary flow.

Table 4: F-test statistics for the reduced mode trial..

Trial	Mean (Winter)	Variance (Winter)	Mean (Summer)	Variance (Summer)
Best Frequency	1.1612	0.0387	0.9271	0.1311
High Amplitude	1.6344	0.1505	1.0088	0.2003
Lower Neumann	1.3210	0.0977	1.0063	0.1280
Lower Dirichlet	1.4367	0.0569	1.0328	0.1163
Reduced Frequency	1.3164	0.1249	.9071	.1023

Reduced Frequency trials had the two lowest means. Best Frequency also maintained the lowest variance. Despite its realtively large variance, the Reduced Frequency mode was the best performer of the group toward the end of the run. In early March, when both net inflow and available observations were low, the Reduced Frequency trial achieved 90% confidence several times. This provides additional evidence that in a weakly forced scenario, including too many higher-numbered modes without sufficient observations degrades NMA's performance.

Among the amplitude selection modes, the Lower Dirichlet and Lower Neumann runs displayed low variances but high means. As with the frequency modes, performance improved during low net boundary flow periods. Still, the High Amplitude trial rarely achieved 50% confidence. The other amplitude selection methods fared better, but each only reached the 80% level once.

Figure 29 presents the F-test results for the Summer period. From the start of the run until late September, the region experiences extremely weak forcing. The MODAS analysis notes a Loop Current meander intruding from the southeast during the last week of September, forming a complete eddy by the end of October. For the majority of the run, MODAS and observed velocities were lower than during the Winter period, with few well defined rotating structures. The thick lines in Figure 29 indicate the same cross boundary flow threshold as in the Winter trials.

In contrast to the Winter trials, the Summer trials had greater success in mod-

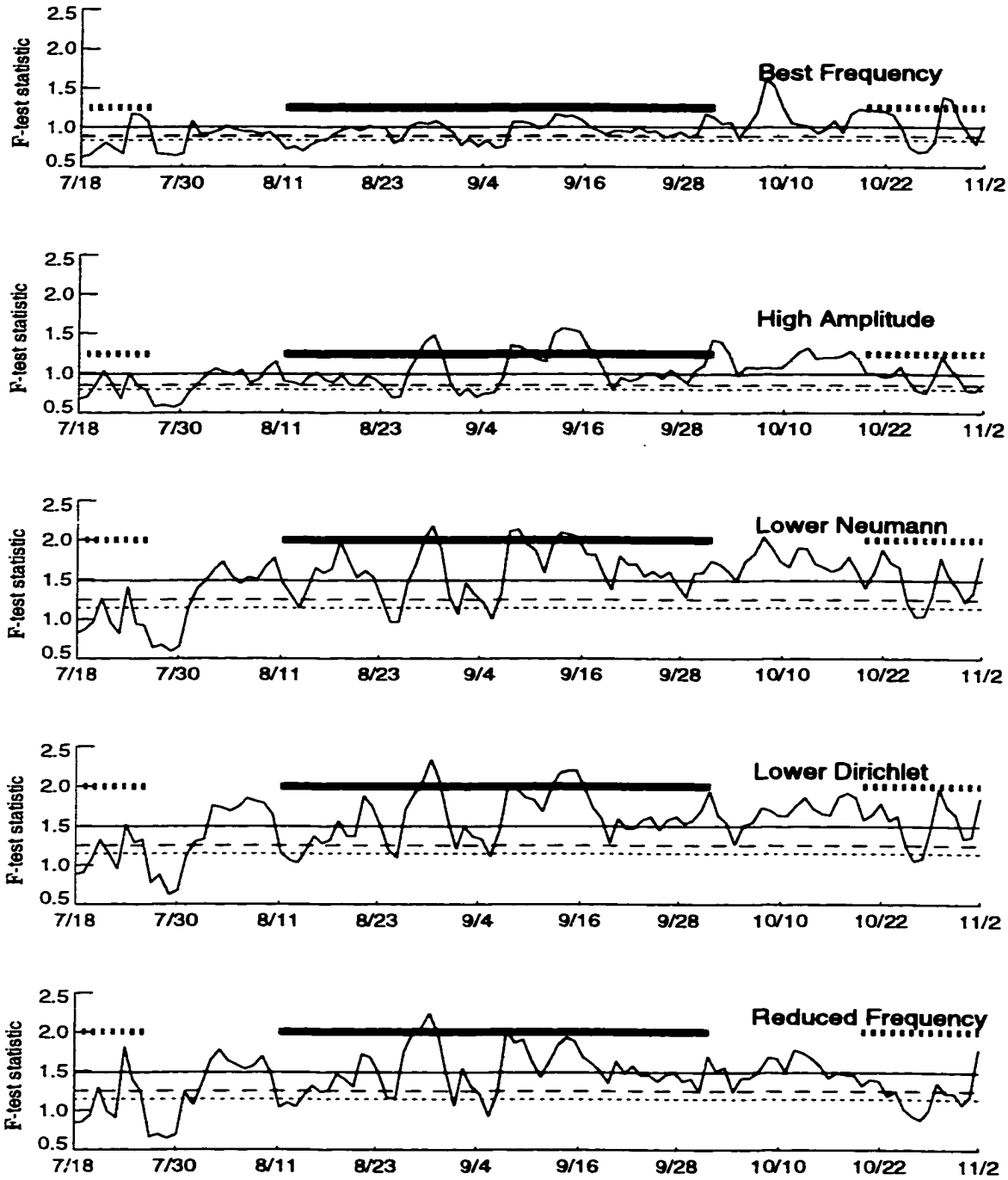

Figure 29: Variance analyses for five reduced mode trials (Summer). In each panel, the 50, 80 and 90 percent significance levels are indicated by thin horizontal solid, dashed and dotted lines respectively. Heavy dashed and dotted lines indicate periods of high cross-boundary flow.

eling the variance of the baseline run. This period had fewer observations, which probably reduced the amount of variability in the baseline amplitudes. All repeatedly achieved 90% significance. Variance, however, was up to four times greater than in the Winter trials. High boundary flow periods had a different effect during Summer. The Best Frequency trial appears unaffected by the cross boundary flow, displaying weaker performance during the low flow period near 10 October. The Lower Dirichlet run, which was the single good performer during high flow periods in Winter, was among the worst during Summer (although still achieving 90% significance four times during the period). As in the Winter trials, frequency selection methods performed slightly better, displaying lower means and less variability. Only small differences arose among the amplitude selection methods.

Summarizing the lessons of Figures 28 and 29, high cross boundary flow degrades reduced mode nowcasting in well sampled, highly dynamic situations. The effects of such an environment are best mitigated by a reliance on Neumann modes. In more settled flow regimes, reversion to increasing the numbers of modes used provides best results.

5.5 Convergence Maps

The correlation results, Error Index comparisons, and subjective depiction critiques of Section 5.2 allows the conclusion that the baseline NMA (58 modes with sampling invoked) yields reasonable depictions of the surface circulation. To illustrate the convenience of NMA in extracting traditionally computationally expensive fields, a brief study of the convergence pattern is presented. The divergence (negative convergence) fields are calculated according to (20). All the components required by (20) to construct the divergence field (Neumann mode amplitude vector and the Neumann eigenfunctions) were generated early in the velocity NMA process, and are now readily available.

Mapping the convergence patterns for this region is challenging. Consideration of currents, river outflows, wind-driven 'piling' of the water along the coast, bathymetry, eddies and the concave shape of the coastline complicates the analysis. Even upon inclusion of these factors, a surface convergence analysis is an incomplete study, since assumptions must still be made about the sub-surface flow.

From Section 1, five convergence features are expected. A 'wind driven' convergence region forms near Brownsville in the fall and migrates to the Louisiana border by mid-summer. Bathymetric features cause 'northern coastal convergence' on the east side of the Texas-Louisiana border and 'northern coastal divergence' on the west. Mississippi River outflow, meeting the shelf break current, causes 'confluence' convergence at the northeastern corner of the region, while anti-cyclonic eddies create mobile convergence centers ('eddy convergence') in deep water.

5.5.1 Winter Convergence

Figures 30 through 32 show the convergence pattern at 15 day intervals from 1 January to 15 March 1994. Positive values of convergence are contoured in solid lines at every 4.6 x 10^{-7} s^{-1}, with maxima indicated by 'plus' signs. Negative contours (divergence) are dotted, with convergence minima marked by open squares. Examination of the convergence maps reveals that in addition to the regular convergence features listed above, a regular divergence area ('deep water divergence') is centered near 94°W 27°N.

The upper panel of Figure 30 displays all five of the expected features. A 2.23 x 10^{-6} s^{-1} convergence maxima centered near 96.1°W 27°N marks the wind driven convergence, already well north of Brownsville as expected in January. At the opposite corner of the region, on the shelf east of 92°W, is the northern coastal convergence, with the complementing northern coastal divergence near the Texas-Louisiana border. The maximum convergence on the map, 2.64 x 10^{-6} s^{-1} at the eastern edge of

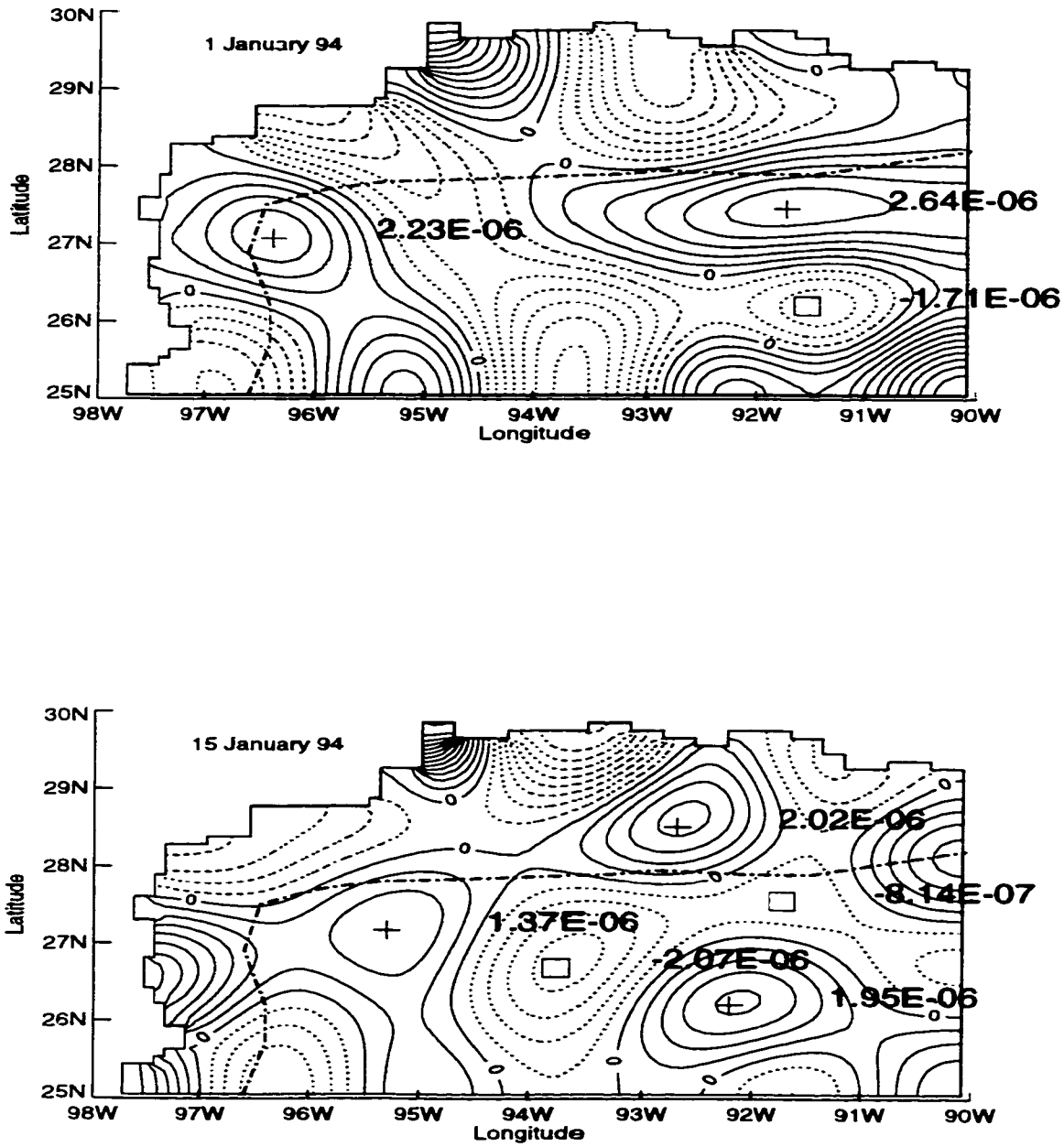

Figure 30: Convergence maps for January, 1994.

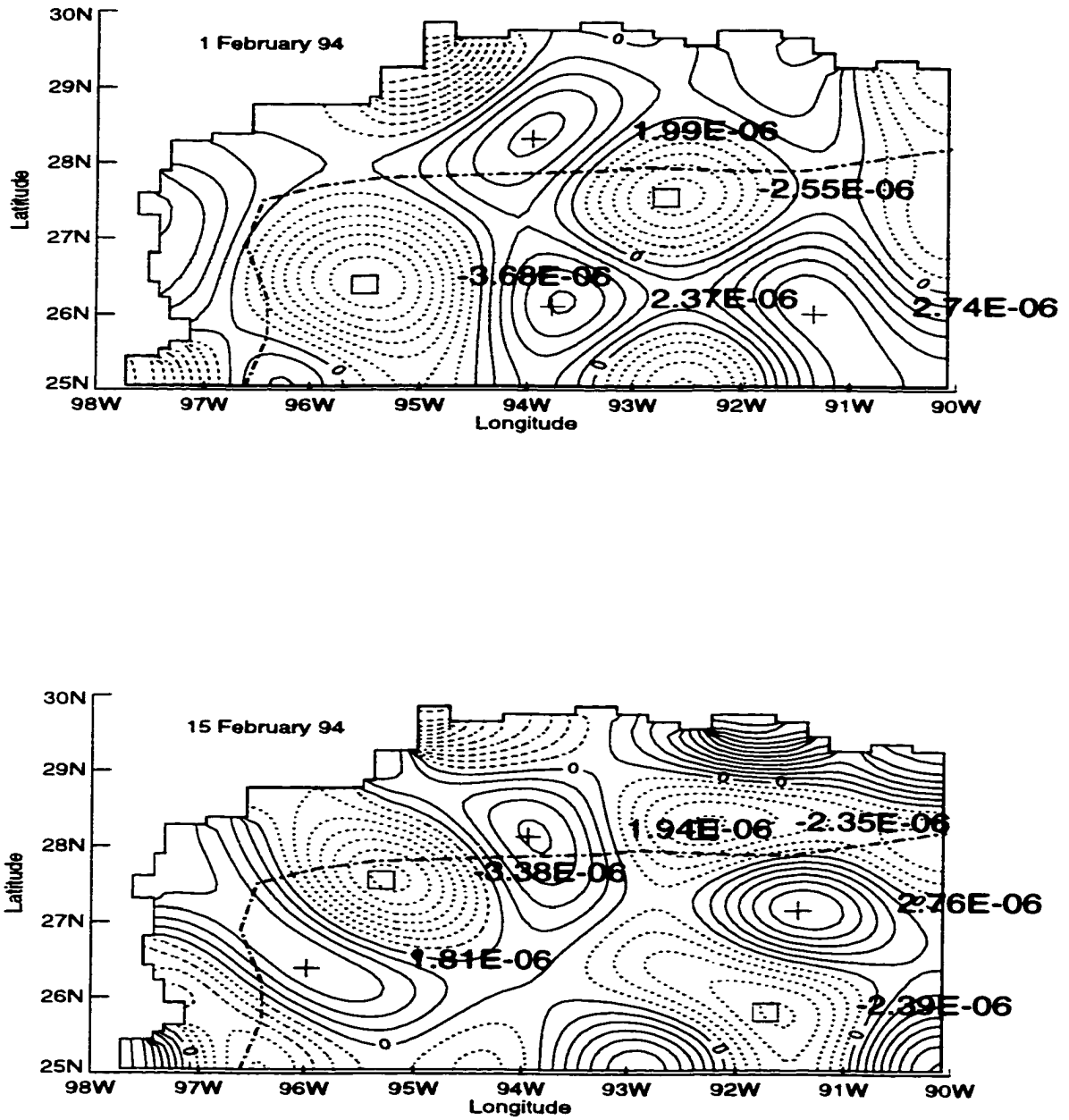

Figure 31: Convergence maps for February, 1994.

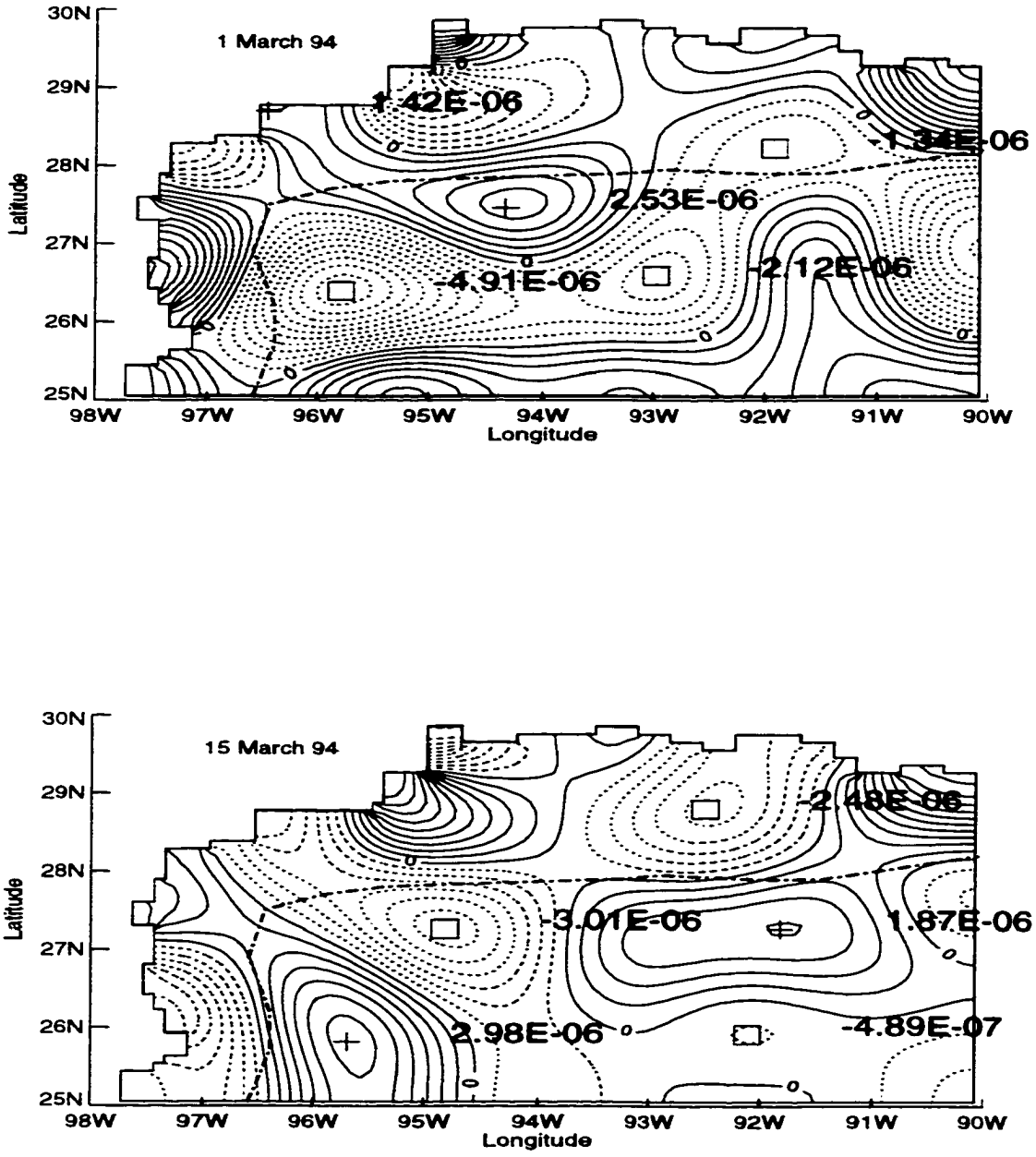

Figure 32: Convergence maps for March, 1994.

the shelf break, corresponds with the confluence convergence. Although no major eddies appeared, the process captures eddy convergence in the southeastern corner due to an anticyclonic meander of the Loop Current, just before eddy shedding.

In addition to the expected features, a pronounced convergence occurs at Galveston Bay (along the coast at 94°W). Although probably artificially enhanced by the crude digital representation of the coastline, this may be the result of the divergent flow from the east encountering the first significant obstacle; the coastline's curve to the southwest. Numerous estuarine plumes from Galveston to Sabine, as noted by *Vastano et al.* [1995], also contribute to convergence here. A second distinct but unexpected feature is the northeast to southwest orientation of a divergence band extending seaward from 96°W 29°N. The southern reach of this band covers what appears to be a regularly occurring divergence region.

Two weeks later (lower panel), the expected five features remain, though slightly modified. The wind driven convergence in the west is stretched to the northeast. The portion closest to the coast is south of the 1 January position, indicating a movement opposite what was expected. (For now, this is regarded as a minor oscillation in the convegence regions' path since in the next map, the convergence region resumes a northward drift.) The northern coastal convergence has intensified and migrated slightly west, consistent with the development and drift of the climatological shelf cyclone. The corresponding northern coastal divergence has decreased in spatial coverage as the shelf cyclone developed, but has increased in intensity. The confluence convergence has advected east, perhaps in response to a reduction in outflow. In the southeast, the anticyclonic meander in the Loop Current has become a detached eddy, with convergence value less than the shallow water northern coastal convergence.

The Galveston Bay convergence and deep water divergence also maintain their signatures. As the northern coastal divergence decreased in area converage but

increased intensity due to the strengthening of the shelf cyclone, the Galveston convergence also became smaller but stronger. Some of the convergence here may be due to outflow of the onshore wind driven convergence moving northeast along the coast. The elongated divergence area noted on 1 January has been interrupted by the onshore wind convergence, leaving a distinct circular deep water divergence region. The divergence maxima here is one of the strongest features on the map at 2.07×10^{-6} s^{-1}.

In early February, the top panel of Figure 31, westward drift of the shelf cyclone and the Loop Current Eddy modify most of the features under consideration. The wind driven convergence continues to track northward, but with decreased intensity. The newly detached eddy interrupts the fetch, decreasing the onshore flow. The northern coastal convergence drifts west, tracking with the eastern limb of the shelf cyclone. The northern coastal divergence region has overtaken Galveston Bay, which now feels the offshore flow of the northern and western limbs of the shelf cyclone (itself a divergence feature), effectively evacuating the bay. The eastern limb of the LCE also deflects the shelf break current, eliminating the confluence convergence. The LCE itself strengthened 25% over the two week period. While moving west, it displaced the deep water divergence point, which nearly doubled in strength. Although not conclusive here, it is tempting to speculate the two are related.

As the LCE continues northwestward and then stalls, the expected features begin recovering their climatological characteristics. In the lower panel of Figure 31, the pattern resembles the 1 January depiction with the exception of the shelf from Galveston eastward. The 15 February MODAS analysis placed the LCE center near 94.5°W 25.5°N. The wind drivern convergence has restrengthened, likely due to the wind approaching from the south-southeast, allowing a longer fetch with onshore flow enhanced by the southwestern side of the LCE. Still, this convergence is not as strong as it was in January, and continues on a slowly weakening trend. The northern

coastal convergence restrengthened dramatically, as did the confluence convergence, suggesting increased outflow due to late winter river run-off. With such a strong northern coastal convergence, the northern coastal divergence remains extended to Galveston. The deep water divergence point shifted northward. Caught between a convergent eddy to the south and the shelf to the north, this divergence center is probably being enhanced by subsurface up-slope flow.

The wind driven convergence shows little movement but significant strengthening in early March (upper panel, Figure 32). This intensification matches the springtime convergence in *Vastano and Barron* [1994], which also migrates north with the shifting wind. Increased river outflow contributes both to the increase in northern coastal convergence and the divergence center on the shelf coincident with the strengthened shelf cyclone. The increased along shore flow in the north re-establishes the convergence at Galveston.

Most striking in this map is the deep water gradient established by the 4.91 x 10^{-6} s^{-1} divergence maximum immediately south of a 2.53 x 10^{-6} s^{-1} convergence maximum. The convergence maximum coinicides with the position of the Texas Plume (see Figure 1), a springtime offshore-directed convergence generating feature theorized by *Vastano and Barron* [1994] to be a return mechanism, moving Gulf water back towards the Florida Strait. The strong divergence maximum may also be a return mechanism, representing the western vertical transfer point for subsurface inflow from the Strait.

In the final panel for this series, the 15 March map displays the convergence pattern without influence of the Loop Current. The remanants of the old LCE appear as the 2.98 x 10^{-6} s^{-1} convergence maximum. Other features appear as expected. Springtime runoff accounts for the large convergent regions in the northeast.

5.5.2 Summer Convergence

Figures 33 through 35 examine the Summer convergence patterns. The beginning of the period includes the annual reversal and weakening of flow over the shelf. Interestingly, some of the largest convergence values occur in this more benign season.

MODAS analysis on 1 August 94 indicated a LCE centered at 26°N 91°W and another halfway into the region centered at 25°N 94°W. As in the Winter map, the eddies influence the convergence structure of the entire region. The wind driven convergence has neared its northern apex, centered on the coast at 94.8°W. The western portion of this convergence region may be enhanced by the shoreward, cross-shelf flow around the east side of the western LCE. At this time of year, the shelf cyclone is gone, replaced by an anti-cyclone with a shoreward western limb also directing flow towards the Galveston area, supporting convergence. Along the eastern portion of the shelf, the northern coastal convergence/divergence structure exists as expected, though less intense than in the Winter. The weak summertime river outflow converging with the weak northeasterly coastal current provides just enough convergence to overcome the diffluent effects of the shelf anti-cyclone's eastern (offshore) limb.

The strength of the convergence centers associated with the two LCE's is remarkable. (They are top two highest convergence centers in either series.) With little wind mixing in August to disturb the eddies, they persist at greater intensities than their Winter counterparts. The combined convergence of the LCEs (10.63 x 10^{-6} s^{-1}) is nearly balanced by the 3.1 x 10^{-6} s^{-1} divergence center at the eastern edge of the shelf break and the implied over 5.6 x 10^{-6} s^{-1} center along the middle of the southern boundary.

Two weeks later, in the lower panel, the amplitude of the overall convergence pattern has markedly decreased. The western most eddy encounters the shelf break and

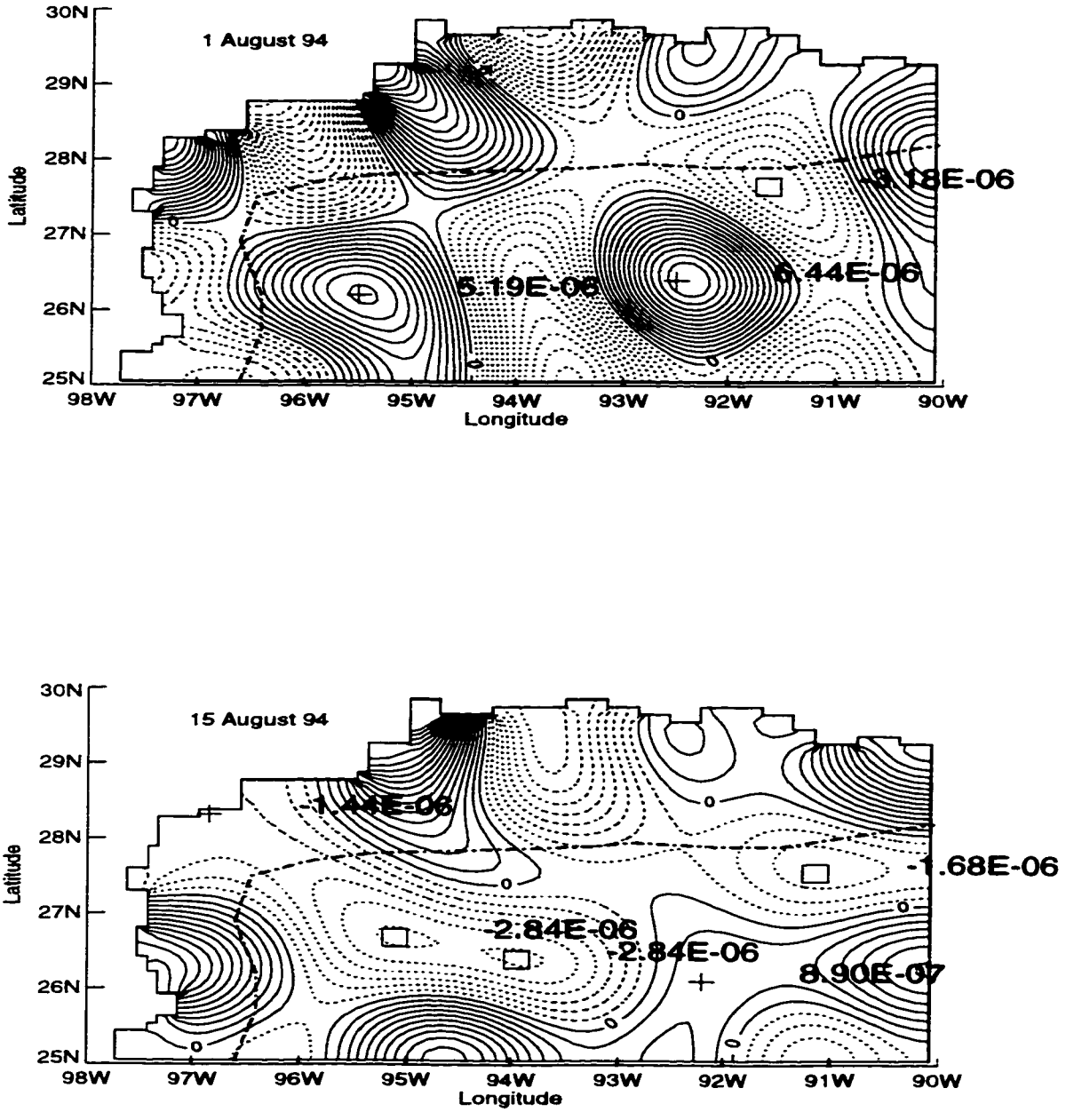

Figure 33: Convergence maps for August, 1994.

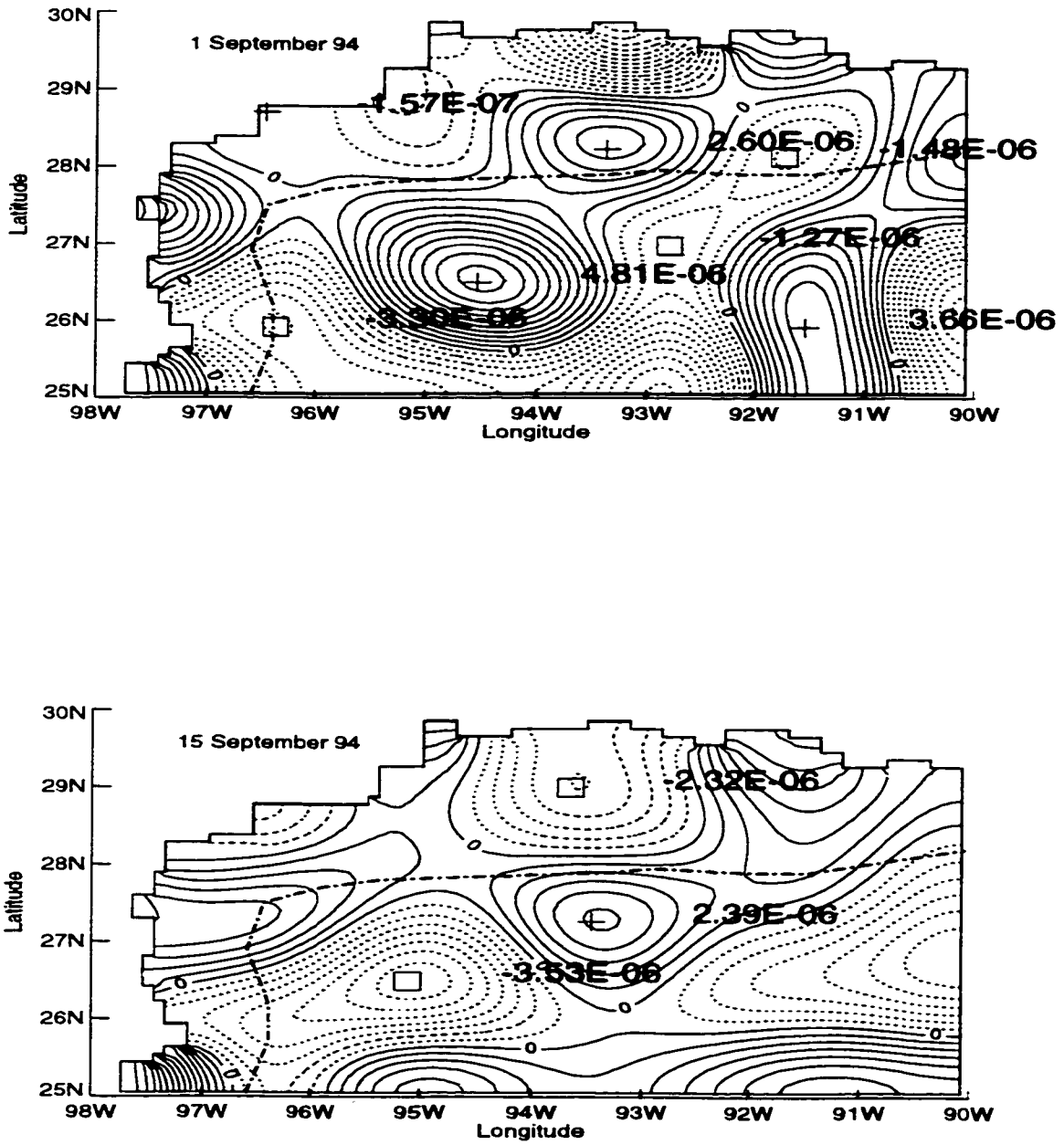

Figure 34: Convergence maps for September, 1994.

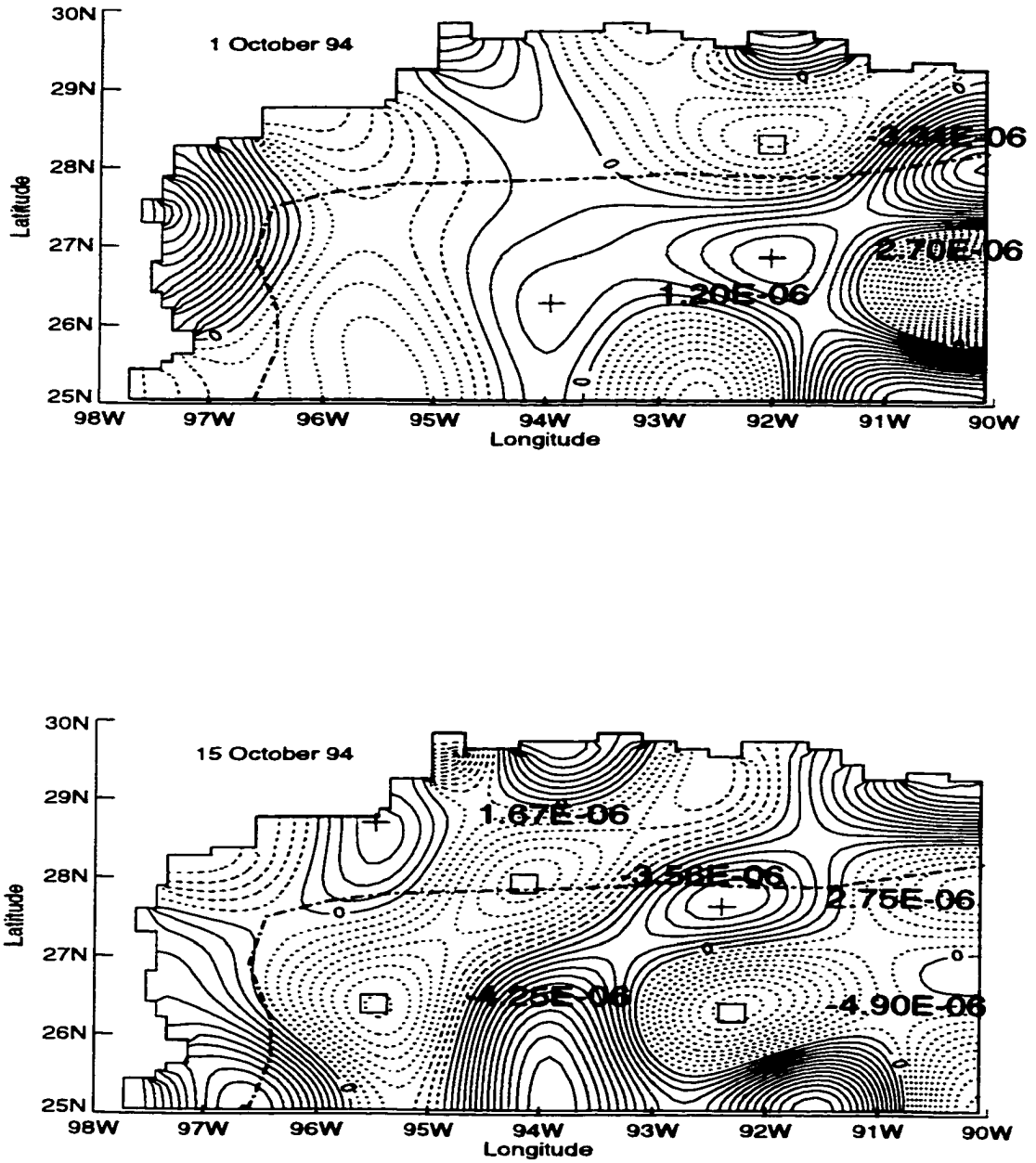

Figure 35: Convergence maps for October, 1994.

dissipates, but remnants of its strong convergent region advect towards the coast. The eastern eddy drifted southeast while weakening, but the combined convergence of both eddies is still above 9.2 x 10^{-6} s^{-1}. As the eddies cleared the center of the region, a wide area of divergence re-established, while a new eddy (also evident on the MODAS analysis) begins to detach in the southeastern corner. On the shelf, the coastal anti-cyclone persists, keeping a convergent flow near Galveston while drawing moving water seaward along 93°W. This offshore flow requires an easterly flow along the coast for continuity. Tropical Storm Beryl moved north along 88°W from 14 to 19 August, presumably enhancing the westerly coastal flow at the time of this map. This increased the replacement flow required due to the shelf anticyclone. As this replacement flow traversed the shallow shelf area, the coastal convergence zone strength was maintained.

By September 1, flow along the shelf returns to the usual configuration, restablishing the shelf cyclone and Texas Current. The wind driven convergence has returned nearly to its southerly position along the coast. The northern coastal convergence and northern coastal divergence are in the climatologically expected positions. A large convergence maxima, indicative of a strong LCE, appears centered at 26.5°N 94.5°W, with no corroborating eddy on the MODAS analysis. The convergence region is again nearly balanced by two divergence maxima to the northeast and southwest. This convergence may result from an eddy undetected by MODAS for various reasons including an unusually weak thermal structure in the eddy or an insufficient number of observations. Additionally, the convergence may be supplemented by the multiple, episodic current reversals near the northwestern corner of the shelf break described by *Vastano et al.* [1995].

With the exception of a moderately strong convergence region south of the shelf break near 93.5°W, convergence in the lower panel of Figure 34 is confined to the outer boundaries. This single convergence region may be a combination of the

confluence convergence and the intrusion of a cyclonic meander in the Loop Current. This map stands out as the most predominantly divergent period observed, although Figure 3 indicates strong boundary inflow indicative of overall convergence. This contradiction implies significant vertical motions at work which are unresolved here.

In October, the wind driven convergence strengthens (top panel of Figure 35) then relaxes (lower panel), again indicative of that feature's oscillatory character. Most interesting in the October depiction is the coastal divergence/convergence structure. In the top panel, a stong divergent center exists directly south, but still on the shelf, of the expected coastal convergence. MODAS analysis for the day shows a reversal of the shelfbreak current, flowing very weakly to the west. If winds over the northeastern region were unusually weak, the Missisippi outflow would move directly south or even southeast as *Oey* [1995] suggests. A reasonable scenario then has a split Mississippi/Atchafalaya outflow under weak winds, with the western portion converging over the shallow shelf but the eastern portion continuing southward. The southward branch encounters the Loop Current creating the northeastern convergence maximum. Strong winds in the southern portion of the region would support the strong wind driven convergence as well as a temporary reversal of the shelf break current's surface signature. The situation is likely short-lived, since a more normal pattern has emerged by 15 October.

6 Discussion and Conclusion

6.1 Assumptions and Limitations in NMA

Normal mode analysis succeeds following careful initial decisions. Early study of the REA target area must satisfy numeric and oceanographic concerns. Numerically, most of the computational resources in NMA go towards generation of the eigenfunctions. The complexity of this process stems from irregularities in the bounding region's shape and the degree of resolution required. In some cases, careful selection of the target area may eliminate extraneous irregular coastline areas. Had this study been mostly concerned with operations on the eastern Texas coast, for example, the coastal irregularities from Matagorda southward could have been eliminated. Otherwise, measures similar to those taken here are appropriate; i.e. masking large boundary solution values generated by sub-scale coastal outcroppings.

Confidence in NMA results rests on three assumptions; the quality of the boundary data, the reliability of the observations, and the accuracy of the model providing simulated observations in data sparse areas. The frequency and resolution of the boundary data places the initial constraint on the type of features one can expect from an NMA map. Here, the once per day forcing at the boundaries was insufficient for initiating tidal signatures. Fortunately tides in the Gulf of Mexico are minimal, but this once-daily approach is not recommended for use globally. Since NMA is forced to accept the boundary data as accurate, computing its effect as an isolated component in the analysis equation (10), using a model sensitive to appropriate physical forcing is best but not essential. (Alternatively, a weighting scheme may be

applied to the boundary data.) One of NMA's advantages is the ability to overcome limitations of the boundary model via ingestion of observations. In this case, wind drives much of the circulation of the Gulf of Mexico, yet the version of MODAS used here produces velocities through geostrophic calculations based primarily on sea surface height and temperature. Despite the lack of direct wind input on the open boundaries, results were useful. The model need only provide the 'general sense' of the open boundary flow for adequate NMA initialization.

The observation data provided the critical resolution and wind forcing needed to accurately map the region. Undoubtedly, more observations are better as long as they are reliable, as was this data set. The primary shortfall in the data remained the lack of coverage in the deep, southeastern portion of the region. This sub-region was governed more by features handled well by geostrophic calculations (eddies and the Loop Current), so MODAS was an adequate source of simulated observations there.

Oceanographically, successful evaluation and interpretation of NMA maps requires thorough knowledge of the features expected in the region. In several cases during this study, NMA placed vigorous eddies across the shelf break where dissipation should have occurred. Usually this resulted in construction of an eddy due to NMA's inability to separate southbound shelf flow from northbound shelf break current flow. Armed with knowledge of the area, these results can be discounted, higher mode numbers included, or a tighter observation network employed.

6.2 Sensitivities of NMA

The sensitivities of NMA emphasize the value of an *a priori* oceanographic understanding of the REA region. The process is most sensitive to the size of features expected to be modeled, the rotational nature of these features, and the spectral behavior of the forcing mechanisms. To avoid effects similar to 'noodling', care

must be taken not to include too many superfluous modes. The reduced mode trials disproved the implied assumption that more modes necessarily produce a better analysis. Conversely, considering too few modes leads to large errors in the least squares computation process, contributing to unrealistic near-boundary velocities. Prior knowledge of the minimum size of a significant feature is essential. Additionally, grid resolution must be small enough to resolve these features.

The reduced mode trials were separated into two categories; frequency-selected methods and amplitude selected methods. Frequency selected methods ingested modes based on the physical forcing signals detected in the observation records. The frequency selected methods worked well in scenarios with strong dynamics, or with small scale rotational features. Strong dynamic forcing included both deep water features distinct enough to show up on the geostrophic MODAS analysis, and features like the Texas Current detected by numerous buoys in close agreement on the direction and magnitude of the flow. When forcing relaxed, modes numbers 23 and above degraded the analysis.

The success of frequency selected methods depends upon accurate determination of the forces at work in the area. To determine this, a variety of sources are preferred. The Lagrangian drifters were advantageous due to their spatial coverage, reaching areas otherwise unavailable, but were often trapped too close to eddy centers or blinded by the motion of an eddy in which they are trapped. Fixed current meters provided expanded spectral coverage, but lacked the area coverage of the mobile sensors. More and varied types of data collection are preferred.

High amplitude methods worked well when large scale features, including 150 km diameter eddies and prominent Loop Current meanders but excluding items like the Texas Plume or the Padre Island convergence, dominated the region. Here, modes were selected based on magnitudes with no concern for the physical forcing mechanism. In such a method, one assumes that how a signal is generated is not

as important as the effect it has on the area. These methods were particularly well suited for scenarios rich in observations. Even better performance can be gained through advanced knowledge of the rotational character of the region, slanting the analysis towards Dirichlet or Neumann modes as appropriate.

The cross boundary flow can confuse or contradict the interior pattern in highly dynamic scenarios. Reduced mode nowcasts for such situations suffered during high outflow periods, which may have biased the analysis toward a divergent (or Neumann) initialization. Reliance on Neumann modes reduced the effect of the high cross boundary flow.

6.3 Gulf of Mexico Circulation Lessons

The data analysis of Section 4 revealed important forcing mechanisms undetected by drifting buoys. The most common forcing mechanisms (wind and some eddy characteristics) in the 0.01 to 0.2 cycles per day region and the tidal/near inertial region were readily captured by most sensors. More elusive are the fluctuating signals in the 0.2 to 0.8 cpd range, sometimes captured by the fixed sensors. In this middle range, which includes the effects of winter frontal passage and rotational signals of the outer radius of large eddies, only the 0.2 to 0.5 cpd range was captured by modes 29 or lower. Although the resultant surface maps seem reasonably accurate, the significance of the 0.5 to 0.8 cpd band remains in question.

The convergence maps revealed two recurring processes which, although requiring verification by additional study, imply a capability to map the outflow of vertical structures in the Gulf of Mexico. These convergence maps were constructed with minimal additional computer time (less than one minute) following the construction of the velocity nowcasts.

The convergence study suggests that a large divergent center tends to persist in the center of the region. Typically positioned near 94°W 27°N, the center moves

in response to transiting Loop Current Eddies, and may experience some slope enhancement when diverted northward. This may represent a portion of the feedback loop transporting subsurface water from the Florida Strait to the northwestern Gulf, then returning near the surface via the Texas Plume/shelf break current system.

Convergence maps also support the assertion that LCE's influence circulation on the shelf [*Oey*, 1995]. Divergent regions outside the eddy can disrupt established convergence zones like the wind driven convergence along the western coast. Strong eddies also deflect the shelf break current and establish divergent areas along the eastern part of the shelf where confluence convergence typically forms. Finally, these eddies may enhance the shoreward or seaward flow of the shelf circulation, dramatically altering the strength of convergence or divergence areas established near Galveston at at points eastward along the coast.

6.4 NMA Utility and Items for Further Study

In summary, the blending of disparate data is a viable, accurate tool with features showing significant potential for future use:

- Rapid analysis of an area may be accomplished independent of the synoptic run time schedule of a large scale model in areas where boundary forcing may be safely neglected or modeled climatologically.

- In this semi-enclosed basin, NMA conducted with mode numbers 20 and below, capturing frequencies 0.5 cpd and lower, produced reasonable maps. Computation of the necessary eigenfunctions for modes 20 and lower is within the capability of current operational workstations.

- A disjointed, irregularly spaced field of observations can be converted to a well spaced grid of analyzed values with minimal degradation in the dynamic depiction. These gridded values are suitable for use as boundary forcing for

smaller scale, more physically detailed models.

- Incorporation of subsurface data should allow extension of NMA analysis to three dimensions. Further study of the divergence center with this method is recommended.

- NMA allowed resolution of small scale current features in shallow water. The maps presented here suggest reliable depictions within two to three grid points, or 6 miles. The resolution is a function of operator choices, not mathematical obstacles. With more intricate observation networks and a recomputed basis function matrix, higher resolutions are attainable.

REFERENCES

Blumberg, A. F., and G. L. Mellor, Diagnostic and prognostic numerical circulation studies of the South Atlantic Bight, *J. Geophys. Res., 88*, 4579–4592, 1983.

Chen, C., R.O. Reid, and W. D. Nowlin, Jr., Near-inertial oscillations over the Texas–Louisiana shelf, *J. Geophys. Res., 101*, 3509–3524, 1996.

Cho, K., R. O. Reid, and W. D. Nowlin, Jr., Objectively mapped stream function fields on the Texas–Louisiana shelf based on 32 months of moored current meter data, *J. Geophys. Res., 103*, 10,377–10,390, 1998.

Cochrane, J. D., and F. Kelly, Low-frequency circulation on the Texas-Louisiana continental shelf, *J. Geophys. Res., 91*, 10645–10659, 1986.

Dinnel, S. P., and W. J. Wiseman, Jr., Fresh water on the Louisiana and Texas shelf, *Cont. Shelf Res., 6*, 765–784, 1986.

Durham, D. L., and J. B. Boatman, United States Naval Meteorology and Oceanography Command plans for rapid environmental assessment, In *Proceedings of the SACLANT/ONR/ODU Conference on Rapid Environmental Assessment*, Lerici, Italy, 1997.

Eremeev, V. N., L. M. Ivanov, and A. D. Kirwan, Jr., The reconstruction of characteristics of oceanic flows from quasi-lagrangian data, Part 1: approach and mathematical methods, *J. Geophys. Res., 97*, 9733–9742, 1992.

Everson, R. A., P. Cornillion, L. Sirovich, and A. Weber, An empirical eigenfunction analysis of sea surface temperatures in the western North Atlantic, *J. Phys. Oceanogr., 27*, 468–479, 1997.

Gavart, M., and P. DeMay, Isopycnal EOF's in the Azores Current region. A statistical tool for dynamic analysis and data assimilation, *J. Phys. Oceanogr., 27*, 2146–2157, 1997.

Hamilton, P., Deep currents in the Gulf of Mexico, *J. Phys. Oceanogr., 20*, 1087–1104, 1990.

Hamilton, P., G. S. Fargion, and D.C. Biggs, Loop current eddy paths in the western Gulf of Mexico, *J. Phys. Oceanogr., 29*, 1180–1207, 1999.

Harding, J. M., S. W. Chang, R. M. Clancy, and A. Johnson, Naval coastal ocean prediction, In *Preprints of the AMS Conference on Coastal Oceanic and Atmospheric Prediction*, Atlanta, Georgia, 1996. American Meteorological Society.

Hendershott, M. C., Inertial oscillations of tidal period, *Prog. Oceanogr., 6*, 1–27, 1973.

Johnson, D. R., J. D. Thompson, and J. D. Hawkins, Circulation in the Gulf of Mexico from geosat altimetry during 1985-1986, *J. Geophys. Res., 97*, 2201–2214, 1992.

Kirwan, A. D., Jr., W. J. Merrell, Jr., J. K. Lewis, and R. E. Whitaker, Lagrangian observations of an anticyclonic ring in the western Gulf of Mexico, *J. Geophys. Res.*, *89*, 3417–3424, 1984.

Kundu, P. K., and J. S. Allan, Some three dimensional characteristics of low-frequency current fluctuations near the Oregon coast, *J. Phys. Oceanogr.*, *6*, 181–199, 1976.

Kundu, P. K., and R. E. Thompson, Inertial oscillations due to a moving front, *J. Phys. Oceanogr.*, *15*, 1076–1084, 1985.

Lavin, M. F., R. Durazo, E. Palacios, M. L. Argotte, and L. Carillo, Lagrangian observations of the circulation in the northern Gulf of California, *J. Phys. Oceanogr.*, *27*, 2298–2305, 1997.

Legler, D. M., Empirical orthogonal function analysis of wind vectors over the tropical pacific region, *Bull. Am. Meteorol. Soc.*, *64*, 234–241, 1983.

Lipphardt, B. L., Jr., and A. D. Kirwan, Jr., Numerical modeling study of the Gulf of Mexico basin:Skill assessment, Technical Report Department of Oceanography report 96-02, Old Dominion University Research Foundation, Norfolk, Va, 1996. 104 pp.

Lipphardt, B. L., Jr., A. D. Kirwan, Jr., C. E. Grosch, J. K. Lewis, and J. D. Paduan, Blending HF radar and model velocities in Monterey Bay through normal mode analysis, *J. Geophys. Res.*, under review, 1999.

Lipphardt, B. L., Jr., A. D. Kirwan, Jr., C. E. Grosch, L. M. Ivanov, and J. K. Lewis, Merging disparate oceanographic data, In *Proceedings of the SACLANT/ONR/ODU Conference on Rapid Environmental Assessment*, Lerici, Italy, 1997.

Lozier, M. S., L. J. Pratt, A. M. Rogerson, and P. D. Miller, Exchange geometry revealed by float trajectories in the Gulf Stream, *J. Phys. Oceanogr.*, *27*, 2327–2341, 1997.

Oey, L. Y., Eddy- and wind-forced shelf circulation, *J. Geophys. Res.*, *100*, 8621–8637, 1995.

Oey, L. Y., and P. Chen, A model simulation of circulation in the northeast Atlantic shelves and seas, *J. Geophys. Res.*, *97*, 20,087–20115, 1992.

O'Reilly, W. C., and R. Guza, Assimilating coastal wave observations in regional swell predictions. Part i: Inverse Methods, *J. Phys. Oceanogr.*, *28*, 679–691, 1998.

Pond, S., and G. Pickard, Introductory Dynamical Oceanography, Pergammon, New York, 2nd edition, 1983.

Press, W. H., S. A. Teukolsky, W. T. Vetterling, and B. P Flannery, Numerical Recipes in Fortran, Cambridge University Press, Cambridge, U.K., 2nd edition, 1992.

Rachev, N. H., and E. V. Stanev, Eddy processes in semi-enclosed seas: a case study for the Black Sea, *J. Phys. Oceanogr.*, *27*, 1581–1601, 1997.

Sellschopp, J., and A. R. Robinson, Describing and forecasting ocean conditions during operation Rapid Response 96, In *Proceedings of the SACLANT/ONR/ODU Conference on Rapid Environmental Assessment*, Lerici, Italy, 1997.

Stammer, D., Geosat data assimilation with application to the eastern North Atlantic, *J. Phys. Oceanogr.*, *27*, 40–61, 1997.

Tomczak, M., and J. S. Godfrey, Regional Oceanography: An Introduction, Pergammon, 1994.

Valle-Levinson, A., and K. M. Lwiza, Rapid assessment of current velocities in the coastal ocean, In *Proceedings of the SACLANT/ONR/ODU Conference on Rapid Environmental Assessment*, Lerici, Italy, 1997.

Vastano, A. C., and C. N. Barron, Jr., Comparison of satellite and drifter surface flow estimates in the northwestern Gulf of Mexico, *Cont. Shelf Res.*, *14*, 589–605, 1994.

Vastano, A. C., C. N. Barron, Jr., and E. W. Shaar, Jr., Satellite observations of the Texas Current, *Cont. Shelf Res.*, *15*, 729–754, 1995.

Vukovich, F. W., and B. W. Crissman, Aspects of warm rings in the Gulf of Mexico, *J. Geophys. Res.*, *91*, 2645–2660, 1986.

Whitman, E. C., Evolving U. S. Navy requirements for rapid environmental assessment, In *Proceedings of the SACLANT/ONR/ODU Conference on Rapid Environmental Assessment*, Lerici, Italy, 1997.

VITA

William John Schulz, Jr.
Department of Ocean, Earth and Atmospheric Sciences
Old Dominion University
Norfolk, VA 23529

EDUCATION

Ph.D. Old Dominion University, 1999
Major: Oceanography
M.S. United States Naval Postgraduate School, 1992
Major: Meteorology and Physical Oceanography
B.S. United States Naval Academy (with merit), 1985
Major: Oceanography

MILITARY EXPERIENCE

Anti-Submarine Warfare & Operations Officer, USS BARBEY (FF-1088)
Meteorology Officer, USS GEORGE WASHINGTON (CVN-73)
Forecaster, Naval Atlantic Meteorology and Oceanography Center
Oceanography and Meteorology instructor, Fleet Training Center Norfolk

SIGNIFICANT QUALIFICATIONS AND AWARDS

Surface Warfare Officer
Tactical Action Officer
Ship Routing Officer
Navy Commendation Medal
PACFLT Shiphandler of the Year
Engineering Officer of the Watch
Meritorious Service Medal
Navy Achievement Medal

SOCIETIES

American Geophysical Union
United States Naval Institute
American Meteorological Society

PUBLICATIONS

Schulz, W. J., and Patrick Dixon, "Tale of Two Sorties: Hurricane Emily Threatens the Atlantic Fleet" Mariners Weather Log, 1994.

Schulz, W. J., "Wind Speed and Moisture Sensitivity Tests of the NRL Limited Area Dynamical Weather Prediction Model: An OSSE Study of ERICA IOP-4." *U.S. Naval Postgraduate School Master's Thesis*, 1992.

This document was prepared using LaTeX.